1995

Excited state proton transfer in 9-aminoacridine carboxamides in water and in DNA

Charles Andrew Smith
Iowa State University

Excited state proton transfer in 9-aminoacridine carboxamides in water and in DNA

by

Charles Andrew Smith

A Dissertation Submitted to the

Graduate Faculty in Partial Fulfillment of the

Requirements for the Degree of

DOCTOR OF PHILOSOPHY

Department: Chemistry
Major: Physical Chemistry

Approved:

Signature was redacted for privacy.

In Charge of Major Work

Signature was redacted for privacy.

For the Major Department

Signature was redacted for privacy.

For the Graduate College

Iowa State University
Ames, Iowa

1995

Excited state proton transfer in 9-aminoacridine carboxamides in water and in DNA

Charles Andrew Smith

Major Professor: Dr. Walter S. Struve
Iowa State University

The 9-aminoacridine molecule is important in several different fields of chemistry. The absorption and fluorescence spectra of this compound are pH sensitive and it is this property that allowed it to be used as a pH probe in different chemical environments. The compound exhibits proton transfer reactions which are among the most fundamental of chemical reactions. The planarity of 9-aminoacridine allows it to intercalate into DNA. Intercalation is a process in which the aromatic flat surface of the intercalator inserts between adjacent base pairs of DNA. The large surface area of 9-aminoacridine's fused tricyclic ring system allows strong intercalative binding through van der Waals attractions. 9-aminoacridine and many of its derivatives have been tried as possible antitumor drugs.

The cytotoxicity of an antitumor agent can be dramatically increased through the addition of one or two cationic side chains. This increase in cytotoxicity using the 9-aminoacridine compound as a parent molecule has been investigated through various derivatives with cationic side chains consisting of different number of carbon atoms between the proximal and distal N atoms. Similar derivatives varied the position of the carboxamide side chain on the aromatic ring system.

The objective of this work is to first create a baseline study of the excited state kinetics of the 9-aminoacridine carboxamides in the absence of DNA. The baseline study will allow

the excited state kinetics of these antitumor drugs when placed in DNA to be more fully understood.

TABLE OF CONTENTS

GENERAL INTRODUCTION 1

Dissertation Organization 1
Introductory Remarks 1
Transition State Theory 3
Borgis and Hynes 10
Laser Studies 18
Time Correlated Single Photon Counting 27
References 57

SECTION I. EXCITED STATE KINETICS OF PROTON TRANSFER EQUILIBRIA 61

INTRODUCTION 62

Two State Equilibria 62
Four State Sequential Proton Transfer Equilibria 83
Four State Tautomer Equilibria 109
References 114

EXCITED STATE PROTON TRANSFERS IN 9-AMINOACRIDINE CARBOXAMIDES 116

Abstract 116
Introduction 117
Materials and Methods 119
Results 121
Discussion 132
Acknowledgments 150
Appendix 150
References 152

SECTION II. EXCITED STATE PROTON TRANSFER IN 9-AMINOACRIDINE CARBOXAMIDES IN DNA 155

INTRODUCTION 156

DNA Structure 156
Intercalation 165
References 171

FLUORESCENCE KINETICS OF 9-AMINOACRIDINE CARBOXAMIDE INTERCALATORS IN DNA 174

Abstract 174
Introduction 175
Materials and Methods 177
Results 178
Discussion 187
Acknowledgment 196
References 196

GENERAL CONCLUSIONS 199

ACKNOWLEDGMENTS 202

APPENDIX 203

GENERAL INTRODUCTION

Dissertation Organization

This dissertation opens with a general introduction into the theory of proton transfer reactions. The introduction is a short overview of proton transfer theory beginning with transition state theory. The general introduction concludes with an overview of the theory of proton transfer reactions according to Borgis and Hynes. Following the general introduction is a brief explanation of the experimental technique, apparatus, and data analysis used to obtain the data for sections I and II.

Section I includes an introduction into the characterization of the excited state equilibria kinetics by first investigating the simplest case of the two state equilibrium of 2-naphthol. The more complicated kinetic model of a sequential four state equilibrium is then presented and used in the manuscript contained in Section I. Section II contains the kinetic results for the antitumor drugs when intercalated into DNA. Section II opens with an introduction of the known conformations of DNA and the process of intercalation. This section also includes the second paper. The dissertation closes with general conclusions, acknowledgments, and an appendix containing the computer programs used in obtaining the results of the first paper.

Introductory Remarks

The 9-aminoacridine molecule described in this dissertation is important in several different fields of chemistry. The absorption and fluorescence spectra of this compound are pH sensitive and it is this property that allowed it to be used as a pH probe in different

chemical environments [1,2,19,20]. The compound exhibits proton transfer reactions which are among the most fundamental of chemical reactions. It has been debated as to whether the structure of 9-aminoacridine exists as an aminoacridine **1** or as an iminoacridan **2** [3,4, 21-25].

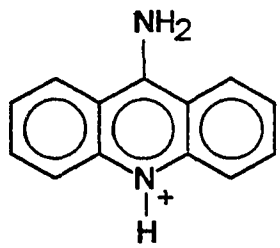

1

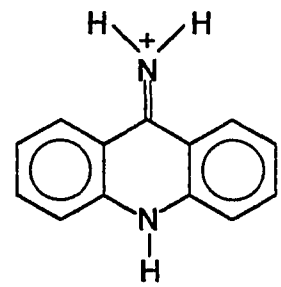

2

The planarity of 9-aminoacridine allows it to intercalate into DNA. Intercalation is a process in which the aromatic flat surface of the intercalator inserts between adjacent base pairs of DNA. The large surface area of 9-aminoacridine's fused tricyclic ring system allows strong intercalative binding through van der Waals attractions. 9-aminoacridine and many of its derivatives have been tried as possible antitumor drugs.

The cytotoxicity of an antitumor agent can be dramatically increased through the addition of one or two cationic side chains [5]. Denny and coworkers investigated this increase in cytotoxicity using the 9-aminoacridine compound as a parent molecule [5, 6, 26].

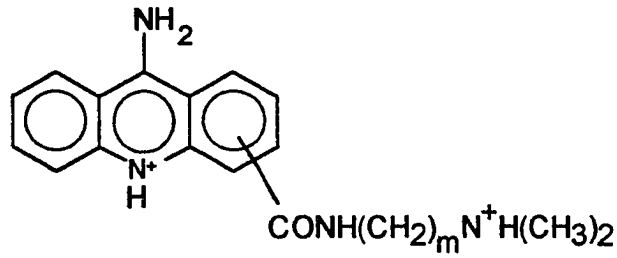

3

Denny synthesized various derivatives **3** with cationic side chains consisting of m number of carbon atoms between the proximal and distal N atoms. Similar derivatives were also synthesized which varied the position of the carboxamide side chain on the aromatic ring system. The DNA binding affinity of an antitumor drug does not always produce antitumor activity and only one of the drugs tested by Denny [6] appeared to have promise as an antitumor drug even though the other derivatives all had high DNA binding affinities.

The objective of this work is to first create a baseline study of the excited state kinetics of 9-aminoacridine and the derivatives of Denny [5] in the absence of DNA. The baseline study will allow the excited state kinetics of these antitumor drugs when placed in DNA to be more fully understood.

Transition State Theory

Transition state theory, TST, summarizes the concepts which affect the rate of reactions that have an activation barrier along the reaction coordinate in their potential energy surface. An energy surface is created by calculating the energy of the system for different fixed nuclear coordinates and plotting the calculated energy verses the nuclear configuration.

Potential energy surfaces are a consequence of the Born Oppenheimer approximation. Figure 1 is a conventional potential energy diagram used to describe reactions according to TST. The reaction coordinate is the path of minimum energy in going from reactants to products. The small basin in the activated state in Figure 1 is characteristic of many potential energy surfaces [7]. The reacting system must pass over an energy barrier before products may be formed. The energy barrier is called the activated or transition state. The ends of potential energy curves in conventional potential energy diagrams are turned up to illustrate nuclear vibrations. The potential energy of the system changes during a vibration due to the change in interatomic spacing. The effect of nuclear vibrations may better be realized in a more detailed general potential energy plot as shown in Figure 2 for the reaction of equation (1).

$$X + YZ \rightarrow XY + Z \qquad (1)$$

The numbers in Figure 2 are contours of constant potential energy. When Figure 2 is viewed three dimensionally it consists of two valleys or grooves separated by a narrow pass [7]. The lower right hand groove of Figure 2 is the region of the reactants because the distance between X and Y is large and the distance between Y and Z is short. The upper left hand groove of Figure 2 represents the nuclear configuration and potential energy of the products. The dashed line of Figure 2 is the reaction coordinate of Figure 1.

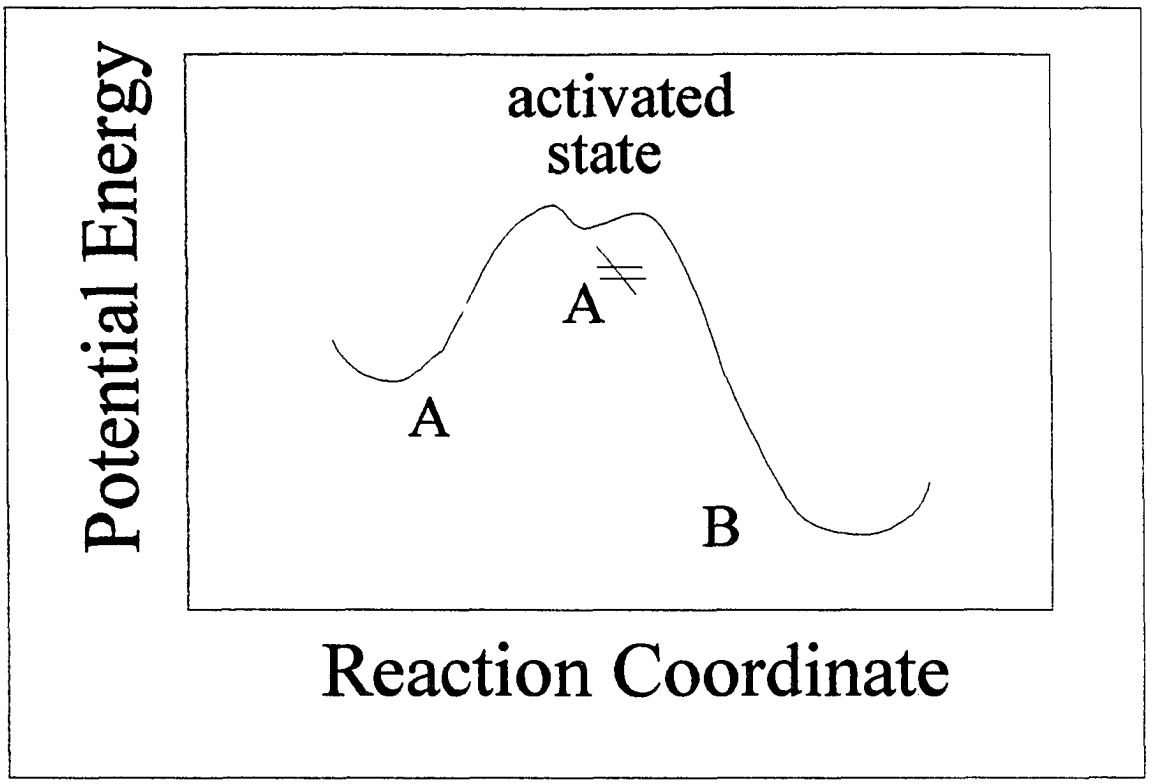

FIGURE 1 A conventional potential energy diagram consisting of the potential energy of the system plotted as a function of the nuclear configuration. The activated state is also called the transition state, which is a high potential energy nuclear configuration which the reactants must pass through before they can become products.

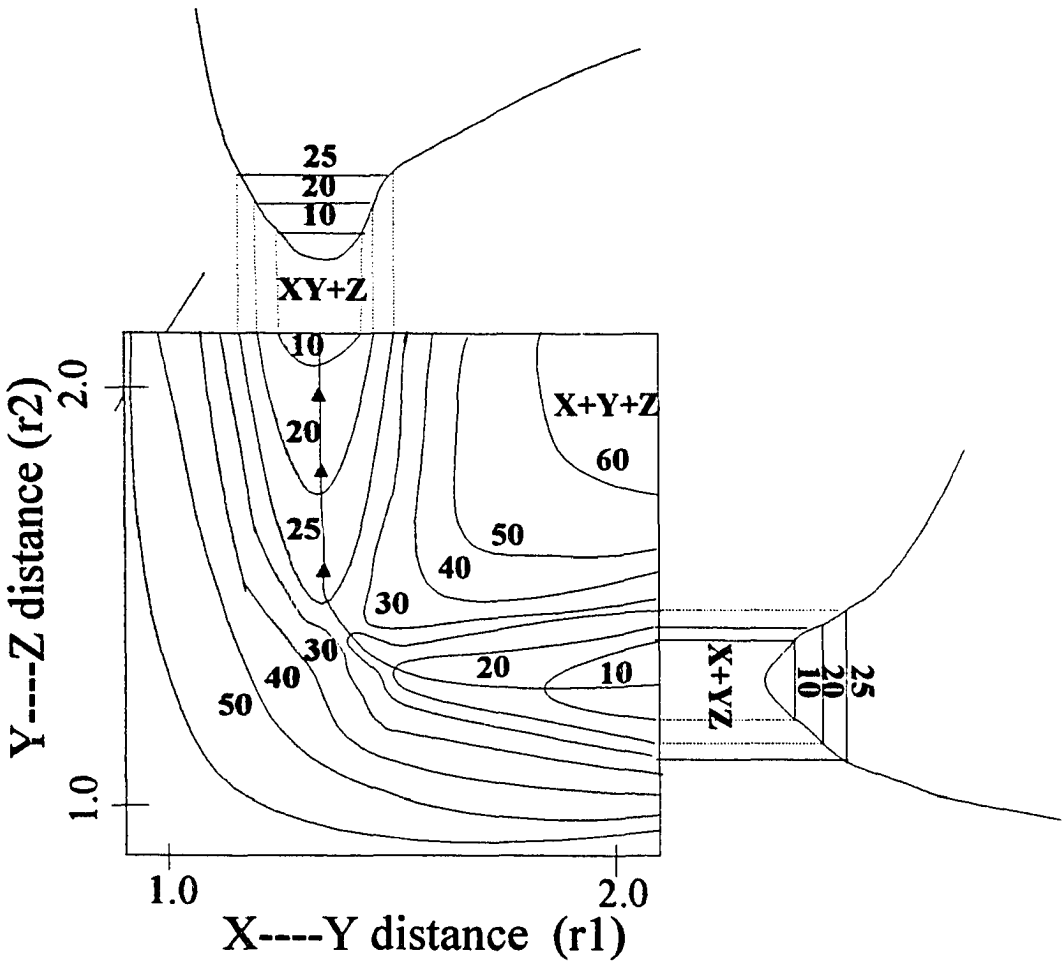

FIGURE 2 A more detailed potential energy diagram. The magnitude of the numbers in the diagram reveals the degree of potential energy for that nuclear configuration. The differing vibrational levels for different nuclear configurations are illustrated with numbers on the vibrational levels which correspond to the indicated potential energy.

$$A \rightarrow B \qquad (2)$$

In the above reaction (2) TST assumes that there is an equilibrium between the reactants A and the species in the activated stated, $(A)^{\neq}$. TST also assumes that once the configuration of the system attains $(A)^{\neq}$ and travels over the barrier it will not reverse its direction on the potential energy surface but will always form products. A successful reaction path in the TST sense is one that reaches then leaves the shallow basin of the transition region in the direction of the product groove and remains in the product groove for a long time [8]. The expression for the rate of the forward reaction in TST is:

$$\frac{dN}{dt} = \frac{\omega_A}{2\pi} \exp\left[-\Delta G^{\neq^\circ} \Big/ k_B T \right] \qquad (3)$$

where k_B is the Boltzman's constant and ω_A is the characteristic frequency of the harmonic energy groove of the reactant. $\Delta G^{\neq^\circ}$ is the difference in free energy between the reactant and the activated species. Equation (3) can be arrived at by assuming the system moves over the barrier without being hindered and the fraction of molecules in the transition state is governed by the Boltzman distribution [8]. TST describes the rate of a reaction such as that in (3) as:

$$\frac{dN}{dt} = \frac{\omega_{coll}}{2\pi} \exp\left[-\Delta G^{\neq^\circ} \Big/ k_B T \right] \tag{4}$$

where ω_{coll} is the collision frequency of the approach of X and YZ [9].

TST incorporates the two main features which contribute to any reaction rate: energy and probability [10]. A reaction with a small cost in energy is more likely to occur than a reaction which costs the system much more energy. This cost is measured as zero point energies and is measured from the bottom of the reactant energy groove to the bottom of the activated energy basin in Figure 1. A low energy barrier allows more molecules to attain the required amount of energy to reach the transition state. Entropy can be thought of as the natural log of probability [10]. For example a system with many closely spaced states has a very high entropy and is much more likely to be formed than a final system which has widely spaced states and a low entropy. TST does not fully account for the change in entropy in a reaction but the model does realize that entropy is an important factor. A function which takes both energy and entropy into account is the free energy function of equation (5)

$$\Delta G^{\neq^\circ} = \Delta H^{\neq^\circ} - T\Delta S^{\neq^\circ} \tag{5}$$

where $\Delta H^{\neq^\circ}$ is the difference in the heat content between the reactant and activated species and $\Delta S^{\neq^\circ}$ is the difference in entropy between the reactant and activated states. We have

stated no difference between enthalpy and energy so $\Delta H^{\neq^\circ}$ is replaced with $\Delta E^{\neq^\circ}$ to get equation (6):

$$\Delta G^{\neq^\circ} = \Delta E^{\neq^\circ} - T\Delta S^{\neq^\circ} \qquad (6)$$

where $\Delta E^{\neq^\circ}$ is the difference between zero point energies of the reactant and activated states.

TST gives erroneous rates for reactions where solvation plays a major role. The difficulty lies in the theory's determination of the entropy especially when the activated configuration carries a charge and the reactants do not. TST overestimates the rate of reactions because it does not take into account collisions with surrounding molecules which may cause the reacting system to recross the barrier even though the energy barrier was surmounted and products were being formed. TST assumes the solvent is in a thermal equilibrium with the reacting system. The solvent however is dynamic and the instantaneous level of energy along any one coordinate is changing constantly due to attractions and collisions between molecules. TST does not account for non equilibrium solvation dynamics [9]. TST also ignores the changing potential (slope) in the transition region and treats the reacting system like a non interacting flight over the barrier making recrossings impossible. In general this model does not describe well the effective frequency for crossing the barrier

including recrossings. Overall TST overestimates the rate and sets an upper limit for the rate of a reaction.

Borgis and Hynes

Recently Borgis and Hynes developed a promising approach for the microscopic understanding of the dynamics involved in determining the rate of proton transfer reactions in polar and nonpolar solvents where tunneling is the main mechanism [11,12,13]. Their approach takes into account three factors involved in proton transfer reactions [13]. The first factor is that the motion of the proton being transferred may be coupled to the vibrational modes of the proton transfer system. A second factor which occurs especially in polar solvents is the electrical coupling between the proton and the surrounding polar solvent molecules making up the local environment. Different local environments create subtle differences in the electronic potential energy surface of the proton transfer system affecting the rate of the reaction. The third factor Borgis and Hynes took into account is the quantum mechanical character of the proton. The proton is a quantum particle and may tunnel through a potential barrier rather than acquire an energy of activation and travel over an energy barrier [14]. Tunneling occurs for light particles when there is a double well in the potential energy surface and since a proton is a light particle a significant portion of its wave function extends out of the potential well the proton currently is in. The probability of tunneling in a double well system increases as the barrier between the wells is narrowed [15].

A description of the Borgis/Hynes model is simplified by considering a symmetric intramolecular proton transfer reaction in the hydrogen bonded complex: described by equation (7)

$$AH^+ - - - A' \rightarrow A - - - H^+A' \qquad (7)$$

where A = A' and A is a heavy atom like oxygen. The Borgis and Hynes model assumes that the proton transfer occurs along a linear $A-H^+$---A' bond and that the proton transfer is electronically adiabatic [12]. The overall proton transfer is in the "nonadiabatic limit" meaning that even though the entire proton transfer process can be described on a single potential energy surface the reaction is dominated by proton tunneling [13].

There are three coordinates in the Borgis/Hynes model. The first coordinate, q, is the proton position and is defined as the displacement of the proton from the center of the A-A' bond. Potential energy surfaces in the proton transfer coordinate q may be calculated for different values of intramolecular separation between A and A' if the Born Oppenheimer approximation holds. The proton is much lighter than its flanking heavy atoms so its motion will be much faster. Figure 3 describe the proton's potential energy for different intramolecular separations of A and A'. In each diagram a double well exists in the potential energy surface in q where the left potential well is for the "reactant" AH^+---A' and the right potential well is for the "product" A---H^+A'. The distance between A and A' contracts and

expands with each vibration of the molecule. This changing distance between A and A' is taken into account by the second coordinate, Q. Equation (8) describes Q

$$Q = R - R_{eq} \tag{8}$$

where R is the intramolecular separation between A and A' and R_{eq} is the equilibrium separation between A and A'. The double potential wells in q depend parametrically on the value of Q as illustrated by Figure 3. Figure 3a is the potential energy diagram in q for the equilibrium separation, Q = 0. Upon a contraction (Q < 0) the barrier in q is lower and narrower as indicated in Figure 3b. Upon expansion (Q > 0) Q increases and the barrier in q concomitantly gets larger and wider as indicated in Figure 3c. The barrier height in q can drop very rapidly with decreasing Q, as much as 50kcal/mol/Å and the tunneling rate increases exponentially with this drop in barrier width and height [12]. The vibrations in the Q coordinate then lead to a modulation of the tunneling rate from the reactant well to the product well. These modulations of the tunneling rate with the vibrations of the heavy atoms is called "coupling fluctuations" and is given the symbol C(Q). The third coordinate of the Borgis/Hynes approach is the collective solvent coordinate, S. S describes the solvent local environment about the charged proton and includes the orientations and alignment of the polar solvent molecules with the proton transfer system. Figures 4a, 4b, and 4c illustrate the affect of the solvent coordinate on the symmetry of the double potential well in the proton

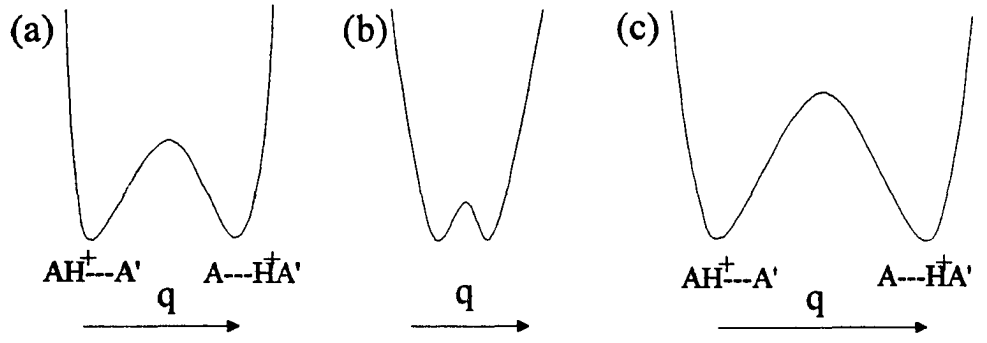

FIGURE 3 Proton double wells for differing values of the Q coordinate where $Q = R - R_{eq}$. (a) occurs when Q = 0, (b) occurs when Q is negative and (c) occurs for positive Q. These three Figures illustrate the parametric dependence of the potential double wells in q on the value of the intramolecular separation Q.

coordinate q. Figure 4a describes the situation when the solvent dipoles are aligned appropriately about the reactant, AH^+---A'. The overall effect is a lowering of the reactant potential well and a raising of the product potential well. The reverse situation is described by Figure 4b where the solvent stabilizes the product, A---H^+A', thereby lowering the product potential well and raising the reactant potential well. The collective solvent coordinate S thus introduces asymmetry into the double well system of q. In Figures 4a and 4b $\Delta\varepsilon$ is the splitting between the ground vibrational energies of the reactant and the product. In Figure 4c $\Delta\varepsilon = 0$ and the double well in q is symmetric. Tunneling occurs only when the double well system in q is approximately symmetric. The tunneling rate decreases dramatically with increasing asymmetry and concomitant splitting $\Delta\varepsilon$ [11]. The solvent molecules are constantly changing their orientation often trapping the proton in the reactant

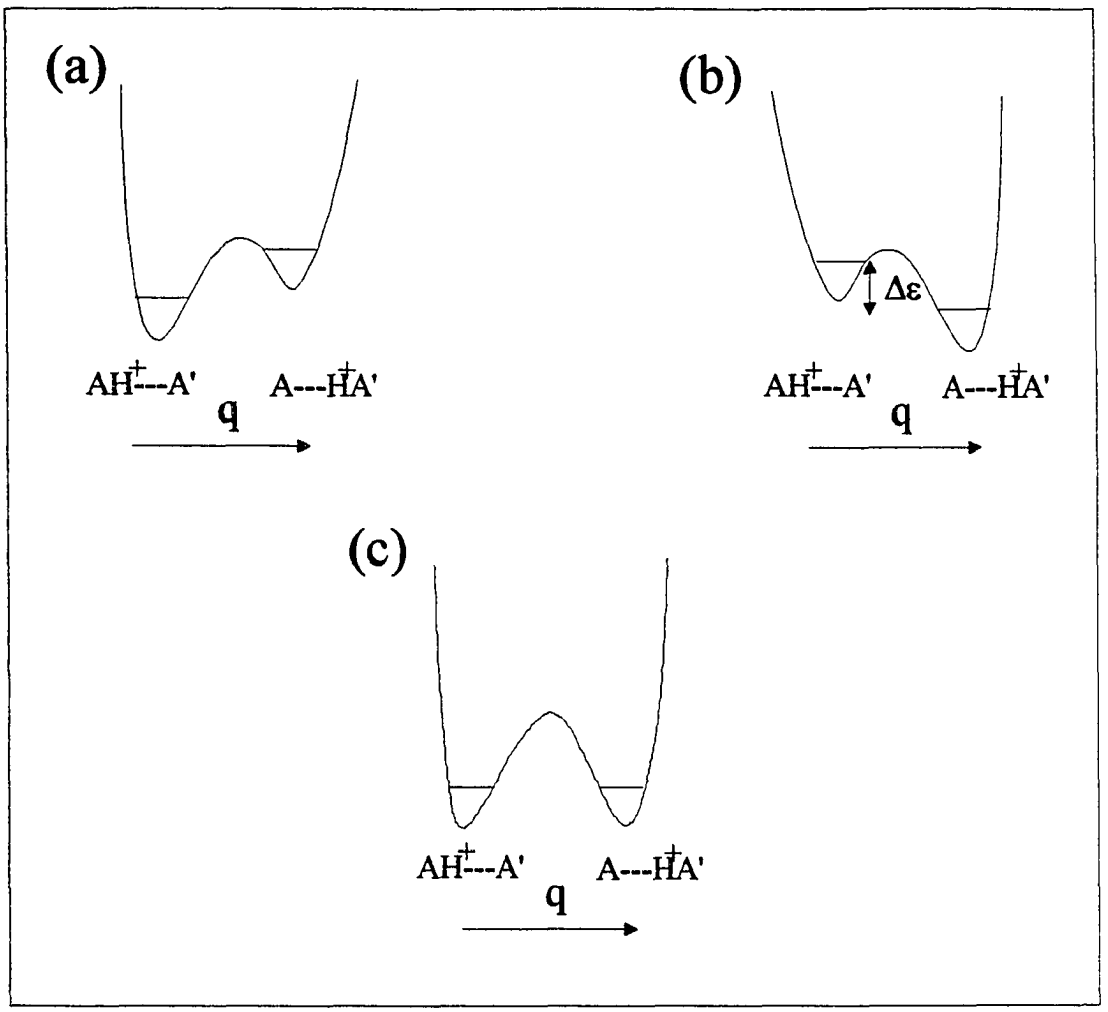

FIGURE 4 The influence of the solvent on the symmetry of the double potential well system: (a) reactant potential well is lowered in energy by the solvent, (b) product potential well is lowered in energy by the solvent, (c) the solvent is organized about the system in such a way that the potential wells are symmetrical allowing proton tunneling between the wells to occur.

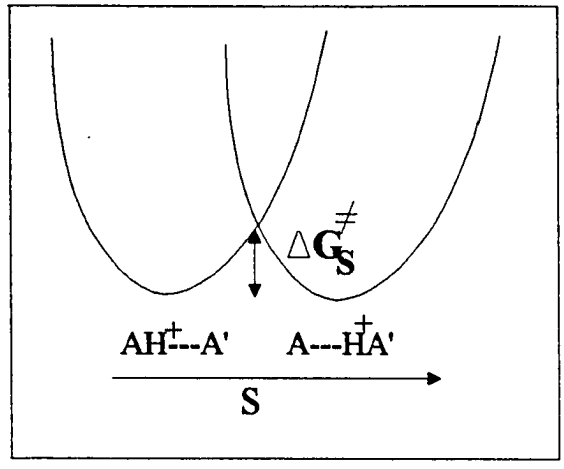

FIGURE 5 The creation of symmetric proton double wells costs the solvent free energy.

or product well then again changing alignment. Tunneling will occur only when the solvent has an appropriate alignment about the proton transfer system. Figure 5 illustrates the proton energies for the reactant and product as a function of the solvent coordinate, S. The difference between the two curves of Figure 5 is the splitting $\Delta\varepsilon$ of Figure 4. In order for the solvent to orient itself to allow tunneling to occur the double well in q must be symmetric resulting in zero splitting $\Delta\varepsilon = 0$. This occurs in Figure 5 where the lines cross and will cost the solvent free energy $\Delta G_S^{\neq}$. The overall effect of the solvent is a slowing down of the proton transfer rate. Figure 3 through 5 assume the Born Oppenheimer approximation for the proton motion described by q in that the motion of the proton is much faster than the heavy atom vibrations in Q and any solvent reorientation described by S. Overall, the double wells in q depend parametrically on two coordinates: the intramolecular vibrations (Q) and the solvent stabilization about the proton transfer system (S).

Borgis and Hynes use a time correlation function formula to evaluate the rate constant k

$$k = \int_0^\infty dt \ \mathrm{Re}\langle j(o)j(t)\rangle \tag{9}$$

of a proton transfer reaction where the function j is the proton probability flux out of the reactant well and into the product well in the proton coordinate q [12]. $j(0)$ is the initial value of the proton probability flux and $j(t)$ is its value at time t. The brackets denote the equilibrium average and Re denotes the real part. Equation (9) provides a way of calculating the rate at a microscopic level and the larger the flux correlation then the larger the rate constant k. The Borgis/Hynes theory determines tunneling to be the dominant process for proton transfer reactions and their rate constant for the proton transfer process is described by equation (10)

$$k = \int_0^\infty dt \ \mathrm{Re}\left\langle C(0)\exp\left[i/\hbar \int_0^t d\tau \ \Delta\varepsilon(\tau)\right] C(t)\right\rangle \tag{10}$$

where C(0) is the coupling fluctuation described earlier at the equilibrium separation of the atoms A and A' [11]. The Borgis/Hynes rate constant thus depends on the coupling C(Q) of the proton tunneling process with the vibrations of the heavy atoms in coordinate Q. The

rate constant also depends on the splitting $\Delta\varepsilon$ of the vibrational energies of the proton by the solvent.

If the dynamics of Q and S are removed from the flux correlation function then the intramolecular spacing between A and A' would be fixed and the solvent would remain in a single collective orientation. The coupling and splitting would then remain at a fixed value C_0 and $\Delta\varepsilon_0$, respectively. The resulting flux time correlation function would then take on the form $\cos\left(\Delta\varepsilon_0 t/\hbar\right)$ and the rate constant would be infinite [11]. A plot of the time correlation function verses time is plotted in Figure 6. Figure 6a depicts that the proton tunneling probability oscillates back and forth between the reactant and product wells when no vibrations or solvent dynamics are taken into account. This type of effect where the tunneling probability oscillates back and forth between wells with a well defined frequency is called coherent tunneling and can be observed in the gas phase [12]. Figure 6b illustrates the result of the time correlation function when the coupling C(Q) and the solvent dynamics $\Delta\varepsilon$ are included. By calculating the area under the curve in Figure 6b the finite valued rate constant can be found. An estimate for the time scale for proton transfer to occur in this system is ~0.04ps [12]. The proton motion thus occurs on a very short time scale and the Born Oppenheimer approximation assumed in Figure 3 through 5 will be valid. The tunneling process illustrated in Figure 6b is incoherent because each tunneling event occurs independently from the other tunneling events. The tunneling process in Figure 6b occurs in

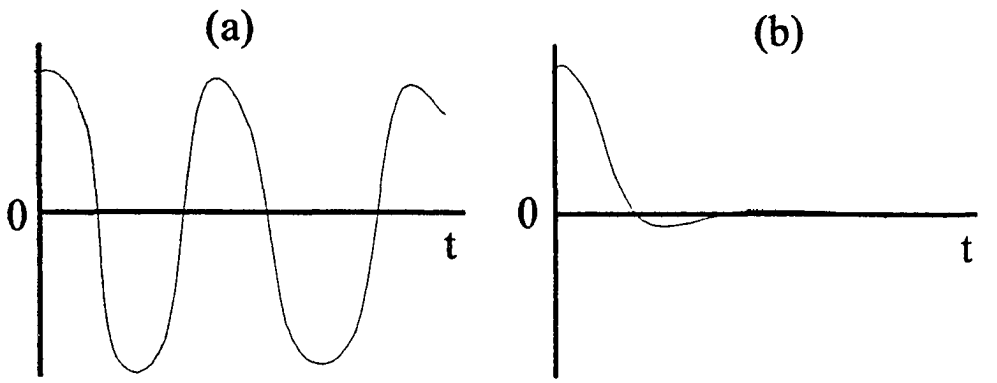

FIGURE 6 The flux time correlation function for (a) the nonrealistic case for when the coupling and splitting are fixed and (b) for the proton transfer reaction in solution where the coupling and energy splitting now fluctuate. The rate constant is the area under curve (b).

a distribution of different solvent environments and the overall rate is just a superposition of all these incoherent tunneling events. This is a very different situation than that described in Figure 6a where the rate constant is meaningless through the loss of dynamics in Q and S. The first and second paper are the original works of this dissertation and they do not involve applications of the Borgis and Hynes theory or the transition state theory. Rather the original works of this dissertation are laser studies of the proton transfers that occur in 9-aminoacridine carboxamides in water and in DNA.

Laser Studies

Laser studies on excited state proton transfer systems can lead to new models and structural information for proton transfer reactions. A review article written by Barbara et al.

[31] contains laser studies of compounds that exhibit intramolecular proton transfer reactions and classifies the compounds into two groups. Both the potential energy surface and the time resolved proton transfer reaction of the compounds were investigated. One type of compound exhibits irreversible proton transfer and the other contains compounds with symmetric or slightly asymmetric double minima in their ground and excited state potential energy surfaces. The compounds that exhibit irreversible proton transfer have excited state potential energy surfaces that contain "double" minima that are strongly asymmetric so much so that it is a basic question for many of these compounds as to whether their excited state potential energy surface has two minima or only one minimum [31]. The compounds that have symmetric double minima potential energy curves in their ground and excited states exhibit splittings in their lowest ground and excited electronic states due to the existence of two identical structures [39]. Compounds with slightly asymmetric minima have two possible representations for their ground and excited state potential energy curves. When the deepest minimum in the excited state coincides with the deepest minimum in the ground state potential energy curve, (the deepest minimum occurs on the same donor/acceptor atom in the excited and ground state potential energy surface) the system has 'common asymmetry.' When the deepest minima in the ground and excited state potential energy curves do not coincide the system has 'reversed asymmetry.' Compounds whose potential energy curves are symmetric, have common asymmetry or reversed asymmetry are distinguished through their distinctive patterns of relative vibronic absorption intensities [31]. Both asymmetric and

symmetric potential energy surfaces that describe intramolecular proton transfer reactions can exhibit ultrafast proton transfer dynamics.

Intramolecular proton transfer reactions between aromatic alcohol donor groups and carbonyl or C=N acceptor groups are generally found to occur with a rate constant $k_{pt} > 10^{11}$ s^{-1} in different environments and even at cryogenic temperatures [32]. Included in this group of fast proton transfer reactions is the isomerization of 9-hydroxyphenalenone. Both isomerized forms of 9-hydroxyphenalenone are shown in Figure 7 by compounds IA and IB. The isomerization in this system is characterized by a symmetrical double minimum potential energy surface because the isomerized forms are identical. The excited state isomerization of the 2-(2'-hydroxyphenyl)benzothiazole system (IIA→IIB in Figure 7) yields a physically different molecule. Excited state proton transfer occurs in this system on the time scale of 160 ± 20fs in nonpolar solvents [29]. The potential energy surface of the reaction IIA→IIB is essentially barrierless in the excited state [29]. 2-(2'-hydroxy-5'-methyl phenyl)benzotriazole (III in Figure 7) exhibits intramolecular proton transfer rates of a few picoseconds in alkane solvents and up to hundreds of picoseconds in long chain alkanols [30]. In noninteracting solvents the intamolecular proton transfer in 3-hydroxyflavone (IVA →IVB in Figure 7) is irreversible and rapid ($k_{pt} > 10^{12}$ s^{-1}) even at cryogenic temperatures [40]. Hydrogen bonding solvents compete with the intramolecular hydrogen bonding of 3-hydroxyflavone causing a decrease in the intramolecular proton transfer rate with increasing hydrogen bonding capability of the solvent [31].

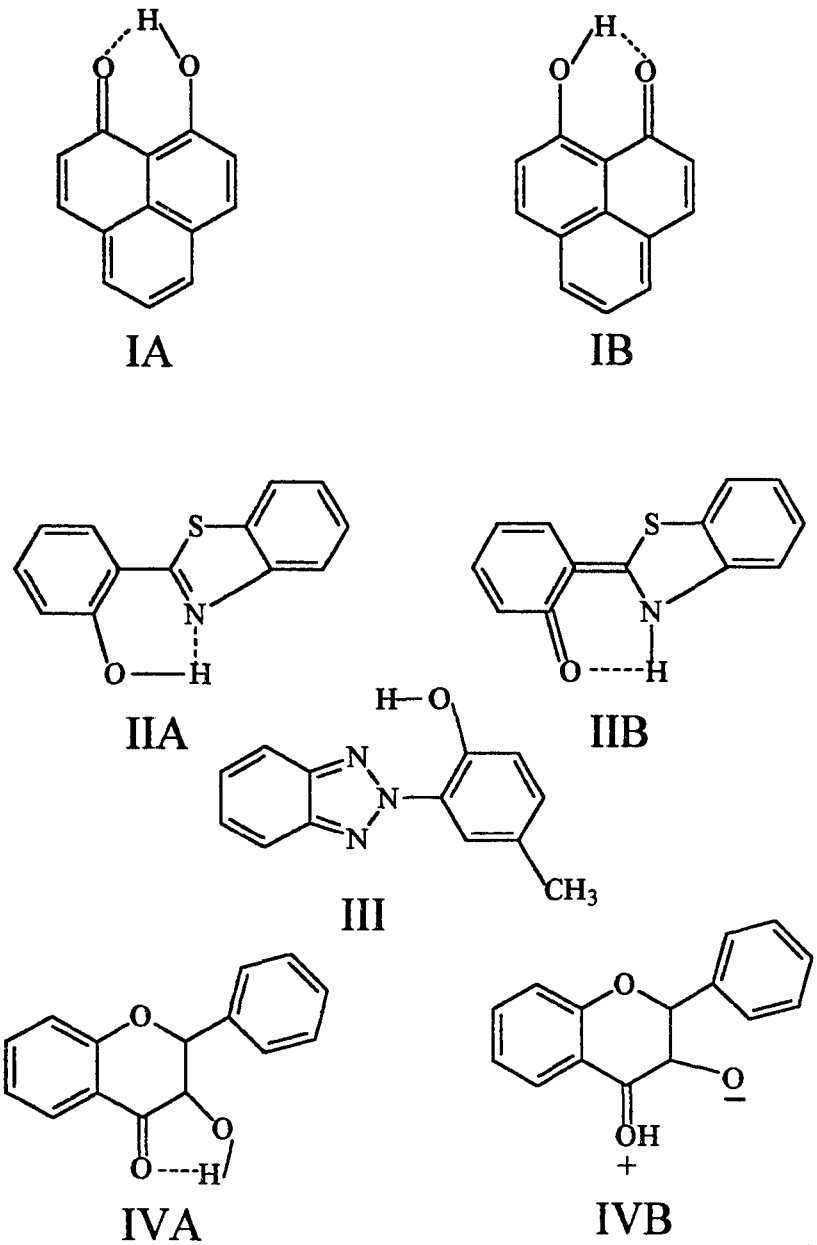

FIGURE 7 Various molecular compounds that exhibit intramolecular proton transfer. Hydrogen bonds are indicated by dashed lines.

Table 1 Compounds That Exhibit Intermolecular Excited State Proton Transfer

compound	pK_a^*	k_d (s^{-1})	reference(s)
2-naphthol	2.8	$(7\pm2)\times10^7$	[41],[45]
2-naphthol-6-sulfonate	1.66	$(1\pm0.2)\times10^9$	[44]
2-naphthol-3,6-disulfonate	0.5±0.1	$(3.1\pm1.1)\times10^{10}$	[42],[44]
8-hydroxy pyrene-1,3,6-trisulfonate	0.4±0.1	$(3.2\pm2.1)\times10^{10}$	[42]

The compounds listed in table 1 each exhibit excited state intermolecular proton transfer. Table 1 lists their respective excited state ionization constants pK_a^*, deprotonation rate constants k_d, and references. The 2-naphthol system has been studied by Laws and Brand [41] by nanosecond fluorimetry. When an electron withdrawing group is placed on 2-naphthol as in 2-napthol-6-sulfonate the pK_a^* decreases by about one pK unit mainly because of a large increase in k_d [42]. When two electron withdrawing sulfonate groups are placed on 2-naphthol as in 2-naphthol-3,6-disulfonate pK_a^* decreases by another pK unit with a further large increase in k_d [43]. The reprotonation rate is diminished because there are now more sites where the proton may be accepted. This supports the idea that reprotonation rate constants are essentially controlled by two factors: the number of sites that may combine with a proton and the diffusion rate [44]. If the excited state deprotonation rates of the four compounds in table 1 are plotted as a function of their respective pK_a^* the plot will reveal a linear relationship between k_d and pK_a^* over more than two pK units [41]. The last compound listed in table 1 contains 3 electron withdrawing groups, 8-hydroxypyrene-1,3,6-trisulfonate, and its deprotonation rate constants are found to

increase linearly with pressure rising from 8 $x10^9$ s^{-1} at 1 bar to 25 $x10^9$ s^{-1} at 9 kbar (temperature kept at 294 K) [44].

Aromatic amines and phenols generally become more acidic in the excited state while aromatic acids, ketones, and certain nitrogen-heterocycles become more basic in the excited state [43]. For example the ground state ionization constant (i.e. pK_a) of 2-naphthol is 9.5 while its excited state ionization constant is 2.8 [41]. The nitrogen-heterocycle acridine tends to acquire a proton in the excited state because acridine's pK_a = 5.45 while its pK_a^* = 10.7 [45]. The forward reaction in acridine is thus a protonation reaction depending on both the acridine and proton donor (usually water) concentrations as described in equation (10b).

$$B^* + H_2O \underset{k_d}{\overset{k_p}{\rightleftharpoons}} BH^{+*} + OH^- \qquad (10b)$$

Equation (10b) shows only the excited state reaction where k_p and k_d are the respective excited state protonation and deprotonation rate constants. Excited state proton transfer studies of the acridine system by Gafni and Brand [46] used ammonium nitrate to allow proton transfer to occur during the short lifetime of the excited state of acridine in certain pH regions. Ammonium ions serve as proton donors and facilitate the excited state proton transfer reaction. 6-methoxyquinoline like acridine is a nitrogen heterocycle but is more basic

than acridine in the excited state. pK_a^* for 6-methoxyquinoline is 11.8 [44]. The rate constant for the deprotonation of water by 6-methoxyquinoline is 5.1 $x10^6$ $M^{-1}s^{-1}$ [44].

Park et al. [47] studied intermolecular excited state proton transfer of 2-naphthol when complexed with β- and α-cyclodextrins (abbreviated β- and α-CDs respectively) by picosecond time resolved studies and molecular modeling techniques. CDs are composed of linked glucose units pictured in Figure 8g. β-CDs contain seven linked glucose units and α-CDs contain six linked glucose units. The 3-dimensional structure of CDs is illustrated in Figure 8h where CDs appear like a two ended open cone. β- and α-CDs have a hydrophobic cavity where the 2-napthol molecule is well embedded as revealed by molecular modeling techniques [47]. 2-naphthol was found to complex with α-CD in the stoichiometric ratios of 1:1 and 1:2 and with β-CD in a single ratio of 1:1 (all ratios are naphthol:CD) [47]. Molecular modeling performed by Park et al. also revealed that neither the β-CD complex nor the 1:1 α-CD complex efficiently shield the naphtholic hydroxyl group from the surrounding solvent allowing 2-naphthol to form hydrogen bonds with the surrounding water molecules. A characteristic of the complexation of 2-naphthol with CDs is the absorption and emission spectral shifts of 2-naphthol when using water as the solvent. The shifts in the absorption and emission spectrum occur through the change in chemical environment of 2-naphthol upon complexation with the CDs. The spectral shifts allowed Park to use the Forster cycle to predict the excited state ionization constants of the 2-naphthol-CD complexes. The pK_a^* of the complexes increased from that of 2-naphthol in

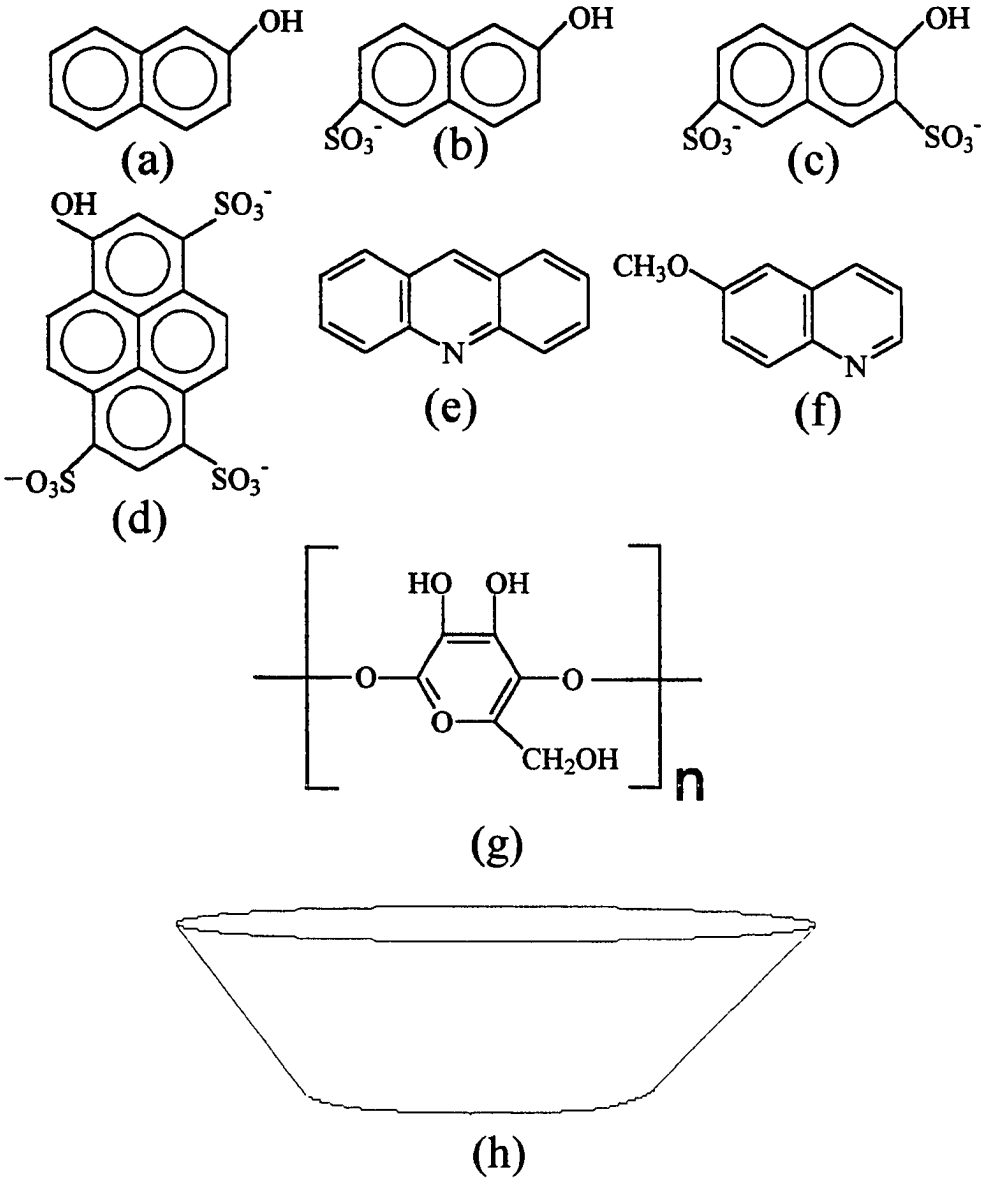

FIGURE 8 See text for description. (a) 2-naphthol, (b) 2-naphthol-6-sulfonate, (c) 2-naphthol-3,6-disulfonate, (d) 8-hydroxy pyrene-1,3,6-trisulfonate, (e) acridine, (f) 6-methoxyquinoline, (g) glucose unit of a cyclodextrin, (h) 3-dimensional shape of cyclodextrins

Table 2 Kinetic Parameters for the 2-Naphthol Complexes with β- and α-Cyclodextrins

compound or complex	k_d ($\times 10^7\ s^{-1}$)	k_p ($\times 10^{10}\ M^{-1}s^{-1}$)	reference
2-naphthol:β-CD	2.2±0.2	2.3±0.5	[47]
2-naphthol:α-CD (1:1)	3.5±1.0	4.2±1.0	[47]
aqueous 2-naphthol	7	4.7	[41]

water. pK_a^* for the β-CD complex increased to 3.6 while the α-CD 1:2 complex increased to a lower limit of four. The increase in 2-naphthol's pK_a^* value upon complexation is believed to be a result from an overall decrease of the excited state deprotonation rate k_d. A much smaller decrease is found in 2-naphthol's reprotonation rate constant k_p when complexed with CDs. The values Park et al. found for the kinetic parameters k_d and k_p are tabulated in table 2.

Supported by their time-resolved spectroscopy and molecular modeling results Park et al. find that reprotonation is essentially determined by the local molecular environment of the proton acceptor (in this case naphtholate). Evidence for this is the effect of cyclodextrin complexation on k_p. Molecular modeling techniques find that the naphtholic hydroxyl group is well embedded in the β-CD complex and this allows k_p for the β-CD complex to be smaller than the k_p for 2-naphthol alone in water (see table 2). For the 1:1 α-CD complex k_p is nearly equal to the k_p for aqueous solutions and the minimum energy structure for this complex indicates that the naphtholic hydroxyl group projects freely into the surrounding bulk water producing very little chemical change of the chemical environment upon

complexation. Park also finds that the deprotonation rates k_d for both 1:1 β- and α-CD complexes are determined mainly by the energetics of the guest-host complex. The same free energy differences between the complexed conjugate acid and base that were used to predict excited state ionization constants with the Förster cycle also account for the differences in excited state deprotonation rates of the complexed species.

The laser studies of the two papers utilize picosecond time resolved single photon counting to investigate the proton transfer kinetics of the 9-aminoacridine carboxamide compounds. The instrumentation, methodology, and data analysis of time correlated single photon counting in our laboratory are described next.

Time Correlated Single Photon Counting

Time correlated single photon counting, abbreviated TCSPC, is a technique used to determine the time resolved fluorescence emission profiles of molecules. The technique is time correlated because each detection has a corresponding delay time consisting of the time difference between the excitation event of the sample and the detection of a photon at the detector. During the data collection period the number of detections for each delay time are counted by creating a histogram of number of detections verses delay time. Each detection placed in the histogram is called a count. A typical histogram of counts verses time is depicted in Figure 9. The x-axis of Figure 9 is divided into 512 time divisions called channels. The height of each channel is determined by the number of counts that fall within

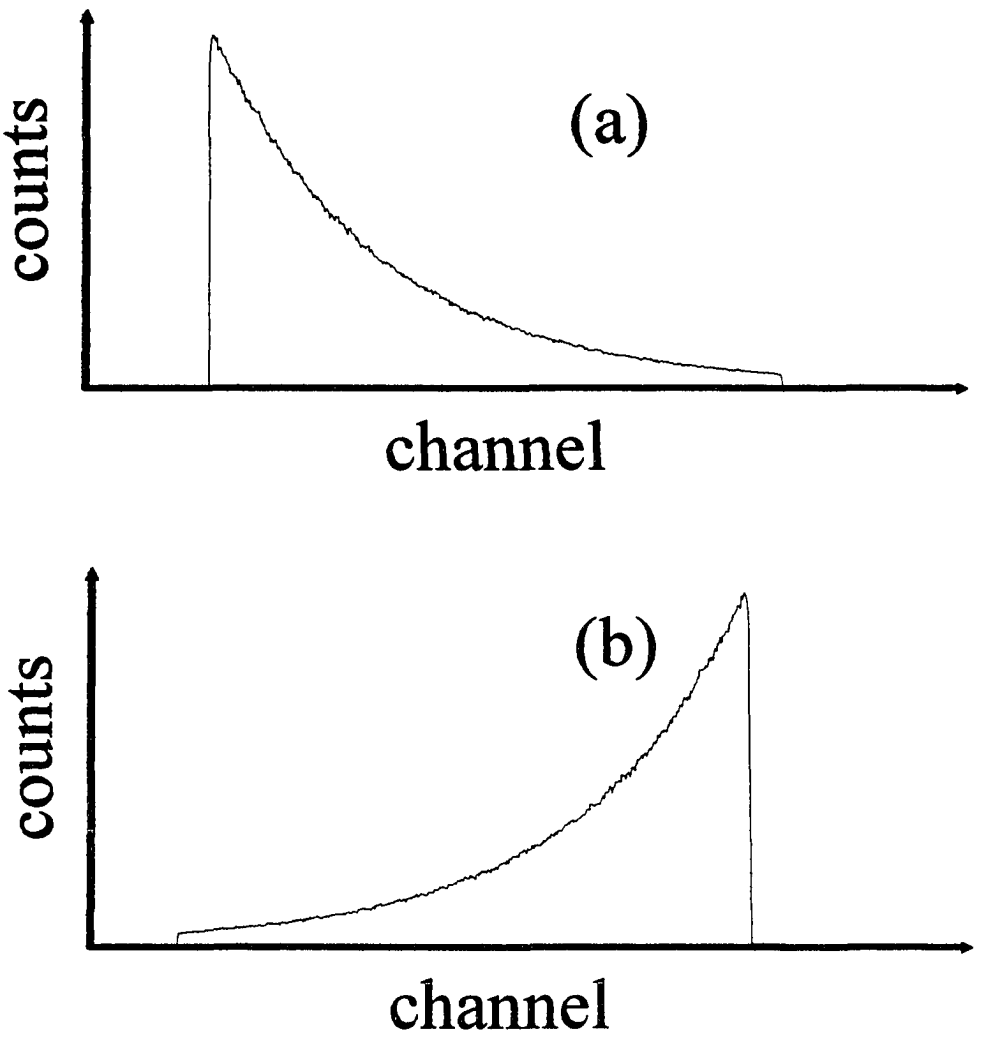

FIGURE 9 (a) describes a photon counting emission curve obtained in the normal configuration (b) describes the identical photon counting emission curve but obtained in the inverted configuration.

the time range of the channel. A typical TCSPC histogram contains a total of approximately a million counts. Because TCSPC detects single fluorescent photons and individually determines their time correlation, extended collection periods are prevented by utilizing a very high excitation rate. The excitation source must not only occur at a very high repetition rate but must be very stable and nonchanging in shape. The excitation event must also be as short as possible to aid in the time resolution of the experiment Our excitation source initially began with a mode locked Ar ion laser which was later replaced with a solid state Nd:Yag laser. Both excitation sources produce very stable and reproducible laser pulses spaced by about 10ns. Figure 10 describes a photon counting set up where the output from a mode locked Nd:YAG laser pumps a dye laser. There are two main reasons for the use of a dye laser. The dye laser creates a choice of operating wavelengths due to the typically wide gain curve of the laser dye. In our system the operating wavelength is chosen with a birefringent filter. Another benefit of a dye laser is that its outgoing laser pulses are inherently much shorter than the incoming laser pulses from the Nd:YAG laser. A qualitative description of the pulse shortening mechanism is given by Fleming [27]. The shortened duration of the outgoing dye pulses is a result from the increasing gain on the rising edge of the dye pulse followed by a rapid depletion of the gain at the peak of the dye pulse. These two factors combine to produce an amplification of the center of the pulse as compared to the wings of the pulse. Pulse shortening continues with each successive round trip in the dye laser cavity until a steady state is created between the dispersive (broadening) mechanism(s) and the pulse

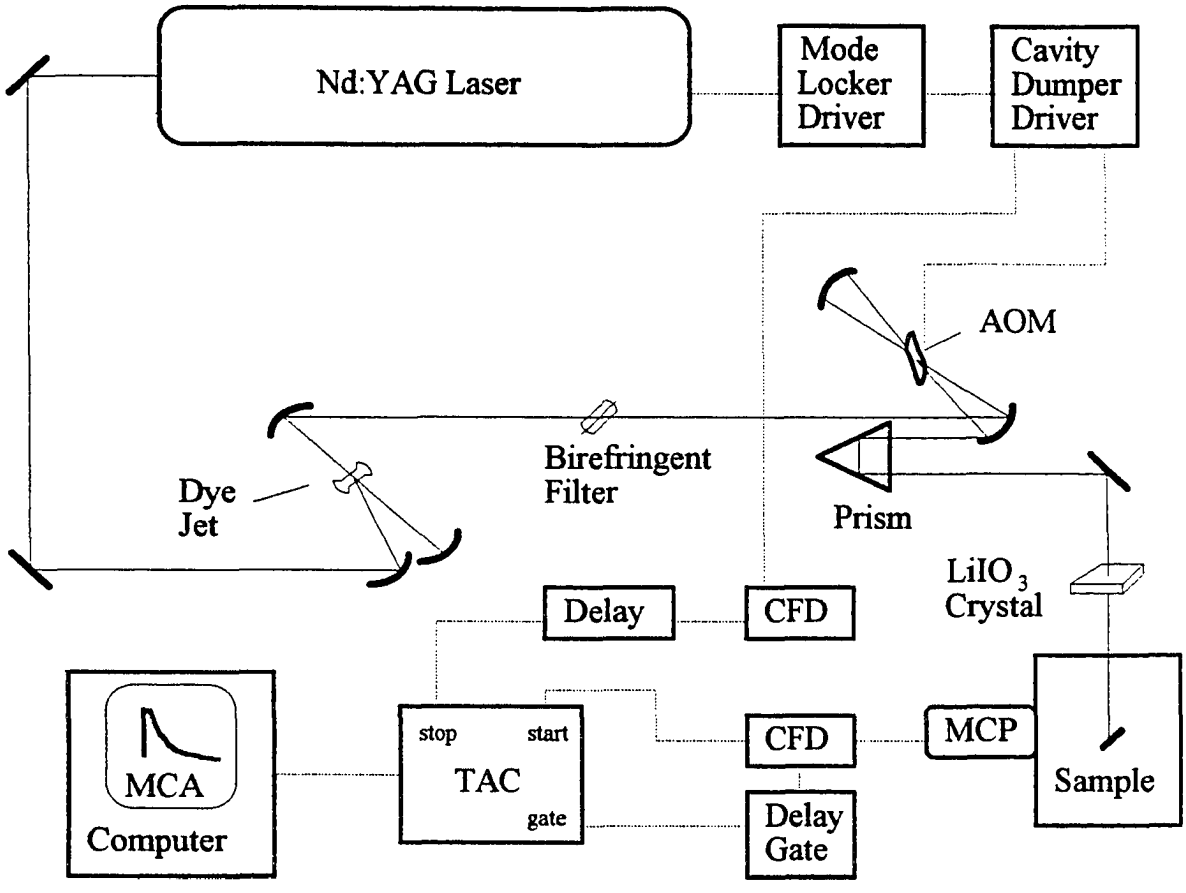

FIGURE 10 Experimental setup: AOM, acousto-optic modulator, CFD, constant fraction discriminator, MCP, multichannel plate, TAC, time to amplitude converter, MCA, multichannel analyzer. Solid lines indicate the path of the laser and dashed lines indicate electronic signal or data transfer.

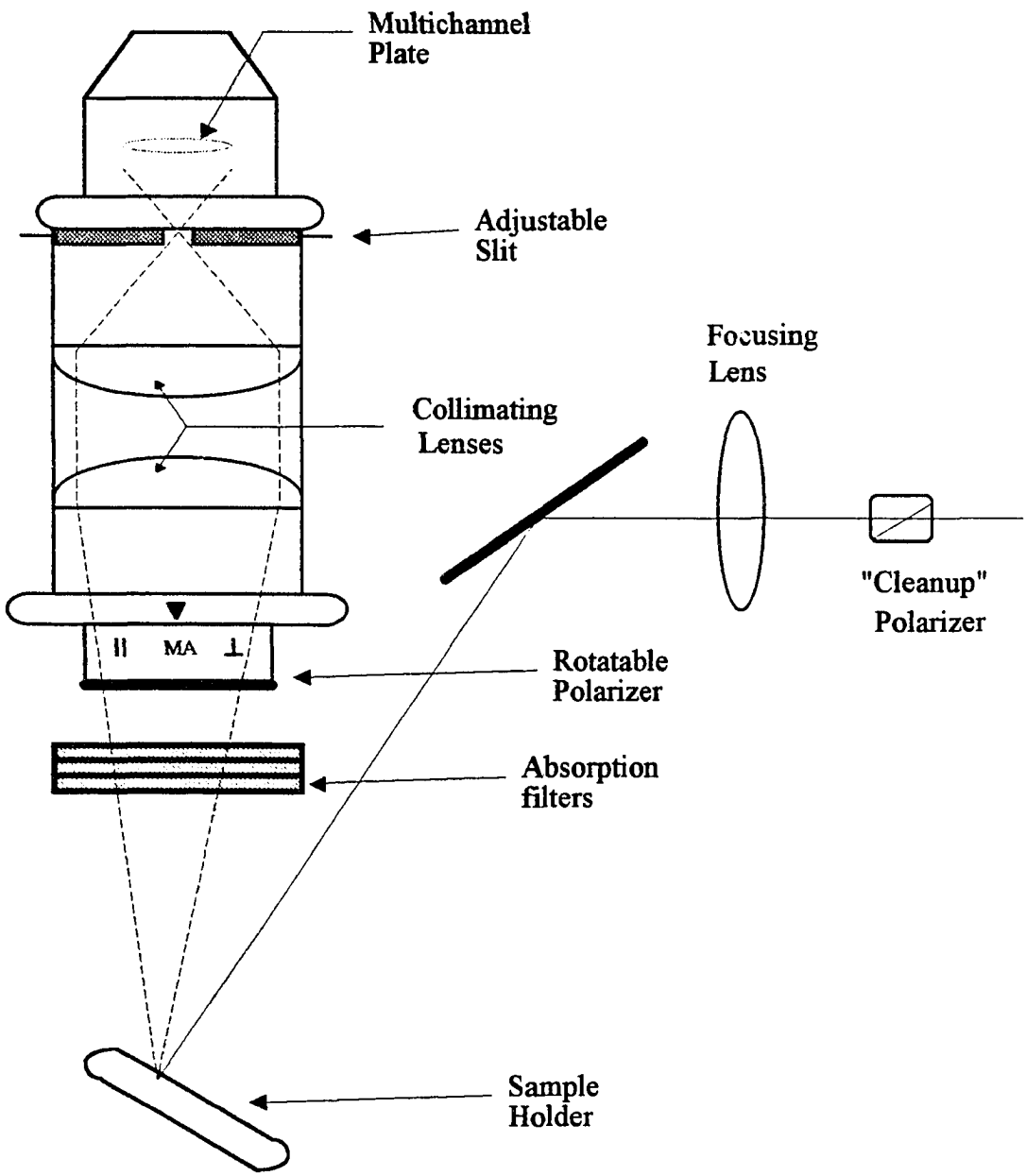

FIGURE 11 Description of the sample chamber where solid lines indicate the path of the excitation light and dashed lines indicate the path of the detected emission focused by the collimating lenses placed before the detector.

shortening mechanism. The duration of a resulting dye pulse is about 10ps. The time interval between dye pulses is still 10ns and this time duration makes it difficult to study samples whose fluorescent lifetimes are on the order of 10ns. Such samples require a rest period between excitation events to allow the sample to fully recover before the next excitation pulse arrives. In order to decrease the repetition rate of the excitation reaching the sample, a cavity dumper is placed in the dye laser cavity. The cavity dumper diffracts one of every N number of laser pulses out from the laser cavity. The time interval between excitation pulses arriving at the sample is extended by increasing N. The cavity dumper thus allows the selection of the repetition rate of the outgoing pulses. The dumper also increases the energy of the individual pulses by allowing the pulses that are not diffracted to remain in the cavity and build up in energy. This is a useful effect of the cavity dumper especially when second harmonic generation is required for excitation of a particular sample. The instantaneous intensity of the second harmonic is proportional to the incident intensity squared. The diffracted laser pulses from the cavity dumper are then sent to the sample chamber.

The sample is housed in an aluminum box whose contents are described by Figure 11. In the sample box the incoming dye pulses pass initially through a cleanup polarizer that ensures the polarization of the excitation source. A focusing lens then focuses the excitation pulses on the sample. The sample holder may be rotated for light sensitive samples. Located directly above the sample are absorption filters that prevent any scattered excitation from reaching the detector. The absorption filters chosen are approximately transparent at the

emission wavelengths of the sample and have very high absorption coefficients at the excitation wavelength. Placed above the absorption filters is a rotatable polarizer for anisotropy studies. It is preferable to have the absorption filters placed after the polarizer because the filters may alter the polarization of the emission from the sample. Located above the polarizer are two collimating lenses which are focused on the same position on the sample as the incoming excitation. The collimating lenses collect a sampling of the emitted photons from the excited sample and focus the emitted light through an adjustable slit. The absorption filters attenuate the excitation through absorption and consequent emission occurs from the absorption filters. The detector detects both emission from the sample and emission from the absorption filters. The emission from the sample may be separated from the emission from the filters by incorporating a background spectrum during data analysis. The background spectrum is found by replacing the sample with a scatterer resulting in emission due solely to the absorption filters. The background spectrum is taken for the same amount of time that was required for the fluorescent sample being studied. Even though the emission from the absorption filters may be taken into account it is best to block the emission from the filters and observe solely the emission from the sample. This is done by using an adjustable slit located above the collimating lenses to act as a spatial filter that will physically block a majority of the emission from the absorption filters before it reaches the detector. The collimating lenses focus a fraction of the emission from the sample through the opening in the spatial filter and ideally it is only the fluorescence from the sample that will reach the

detector. To aid in the prevention of the detection of stray emission from the filters, the slit in the spatial filter can be made very small with the proper adjustment of the collimating lenses.

The detector is composed of a multichannel plate, or MCP. A MCP contains many 1mm long by 10 micrometer wide glass capillaries. The inside of each glass capillary is coated with an electron emissive material. Each capillary acts as an independent electron multiplier because when a photon strikes a capillary wall electrons are emitted and a cascade of electrons then ensues. The MCP converts photons of light to electronic signals. The delay time between the excitation event and the outgoing electronic signal from the detector is the time interval or count referred to earlier.

Precise measurement of this delay time is hindered by two major factors. The first factor includes jitter in the transit time of the detector. The transit time is the time between the photon arrival at the photodetector and the resulting electrical pulse created by the detector. There is a spread in transit times for a detected photon and this spread is called jitter. The second major source of loss in time resolution is related to the electronics in the timing of the arrival of electronic signals. This timing error occurs especially with electronic signals arising from the detector. The signals arising from the detector consist of varying amplitudes and time ranges making it difficult to reproducibly time their arrival. The constant fraction discriminator (CFD) is an electronic instrument designed to overcome the difficulty in timing the arrival of signals with varying amplitudes but of similar shapes. The CFD finds a timing

point on the leading edge of each incoming signal that is amplitude invariant. The CFD first discriminates against the noise from the detector by not accepting any pulse that is not greater than a specific threshold voltage. Next the CFD divides each accepted pulse into two pulses and delays and inverts the larger division. The term constant fraction in this instruments name is due to the constant ratio used by the CFD to divide each accepted pulse into two pulses. The two pulses are then added together to produce a bipolar signal. The zero crossing of this bipolar signal is a constant fraction of the amplitude of the initially divided pulse and can be used as an amplitude invariant timing point. Overall the CFD creates a pulse whose zero crossing is amplitude invariant as long as the pulses under discrimination have a constant shape. It is preferred to have the slope as large as possible at the zero crossing otherwise there will be a small spread of possible zero crossing points resulting in further loss in time resolution. In Figure 10 CFDs are applied to the signals received from the detector and the excitation reference signals from the cavity dumper driver.

The electronic apparatus that is used to measure time intervals is the time to amplitude converter, or TAC. Figure 12 illustrates the operation of the TAC. The TAC contains a capacitor which initiates charging when it receives a start pulse and stops charging when it receives a stop pulse. After the reception of a stop pulse the TAC sends out an electronic signal whose voltage is in direct proportion to the time of charging the capacitor. After each successful start/stop sequence the TAC must remain disabled for a period of time to allow the capacitor to fully discharge. If for some reason the TAC receives a start pulse

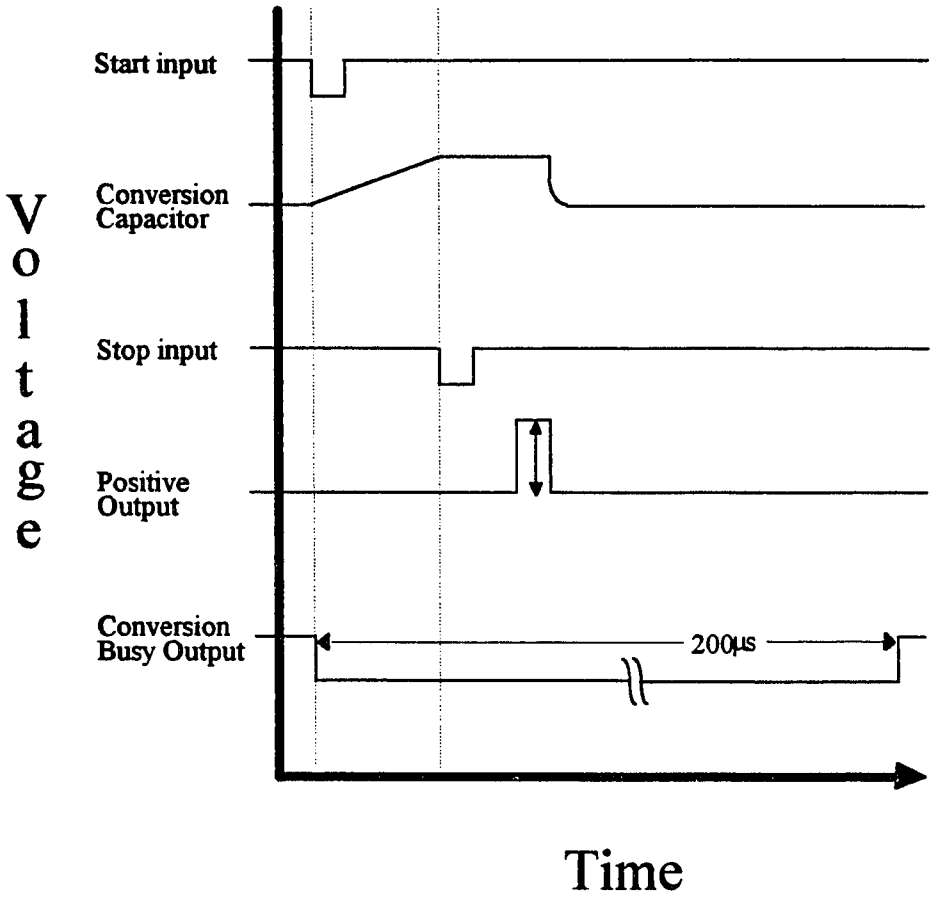

FIGURE 12 Diagram illustrating the operation of the time to amplitude converter.

but no stop pulse the TAC recycles itself and awaits the next start signal. In the normal configuration the start pulse originates from the driver controlling the cavity dumper to indicate the time of the excitation event. The stop pulse originates from the detector indicating the arrival of a detected fluorescent photon. The time interval between excitation and photon detection is a measure of the time duration of the excited state of the sample and is the count referred to in Figure 9. An emission curve obtained in the normal configuration is pictured in Figure 9a.

The normal configuration is not an efficient configuration for the collection of photon counting data. In the normal configuration every start pulse from the cavity dumper driver initiates the capacitor to start charging even though for each excitation event fluorescence does not always occur or may not reach the detector. The TAC does not receive a stop pulse for every start pulse in the normal configuration creating an inefficient data collection process. A more efficient manner of collecting photon counting data is the inverted configuration. The inverted configuration is described by having the start pulse originate from the detection of a fluorescent photon and the stop pulse originate from the cavity dumper driver. An emission curve obtained in the inverted configuration is pictured in Figure 9b. With the inverted configuration the capacitor in the TAC will start to charge only when emission is detected and stop charging upon the arrival of a signal from the cavity dumper driver. The inverted configuration allows the TAC to operate at a lower repetition rate than the normal configuration. The lower repetition rate of the TAC in the inverted configuration

is still very high and it was found that pulse pile-up was occurring in the TAC. Pulse pile-up occurs in the TAC at very high data collection rates. High data collection rates do not allow the capacitor time to fully discharge. Pulse pile-up results in longer lifetime measurements than the true decay because the capacitor is not completely discharged before the next charging event initiates. A solution to this problem was found by making the effective busy time longer as illustrated in Figure 12. The busy time is the amount of time that the TAC does not accept any incoming start pulses and allows the capacitor time to completely discharge. The busy time was extended by externally gating the TAC. An external gate keeps the TAC inoperational after each charging period for an extended amount of time. The length of time that the TAC is forced to rest is determined by the settings on the external gate module.

The outgoing voltage signals (counts) from the TAC are sent to a multichannel analyzer, or MCA. The memory of the MCA is divided into 512 voltage (time) divisions called channels. The MCA sorts and keeps track of each count by placing each count in its appropriate channel. After many counts have been received the MCA will have created a histogram as in Figure 9. The settings on the TAC determine the time resolution of the 512 channels in the MCA. The actual time per channel is determined experimentally by using the delay gate pictured in Figure 10 to delay the stop pulses from the cavity dump driver by exactly one nanosecond. The resulting one nanosecond delay change is observed on the MCA window and the time resolution per channel over the observed one nanosecond may be

calculated. The settings on the TAC also determine the charging region of the capacitor. The linearity of the charging region of the capacitor is checked by delaying the stop pulse signals from the cavity dump driver in one nanosecond intervals across the entire time window of the MCA. The time resolution per channel is then calculated and compared across the entire window to ensure linearity in time measurement.

The emission curve or histogram obtained by the MCA during a photon counting experiment is a convolution of the actual emission curve of the sample and the instrument response function. The instrument response function consists of a conglomeration of processes that each result in loss of time resolution during the experiment. The response function is composed of the time duration of the laser pulse excitation (~10ps), the spread in the transit times at the detector, and the jitter in the timing of the arrival of electronic signals in the electronics. The spread in transit times at the detector is the lower limit for time resolution in TCSPC [28]. The instrument response function is experimentally determined by scattering light off a nonfluorescing sample. A dilute aqueous solution of Coffee Mate has been found to be an excellent nonfluorescent scatterer. The full width at half maximum, or FWHM, of the instrument response function in our lab is normally in the range of 80ps when the wavelength of excitation is 600nm. A typical instrument response function is shown in Figure 13a along with a photon counting emission curve for a particular sample. Both the instrument response function and the emission curve are a histogram of count intensity verses the time interval or channel. The division of the instrument response function into channels is

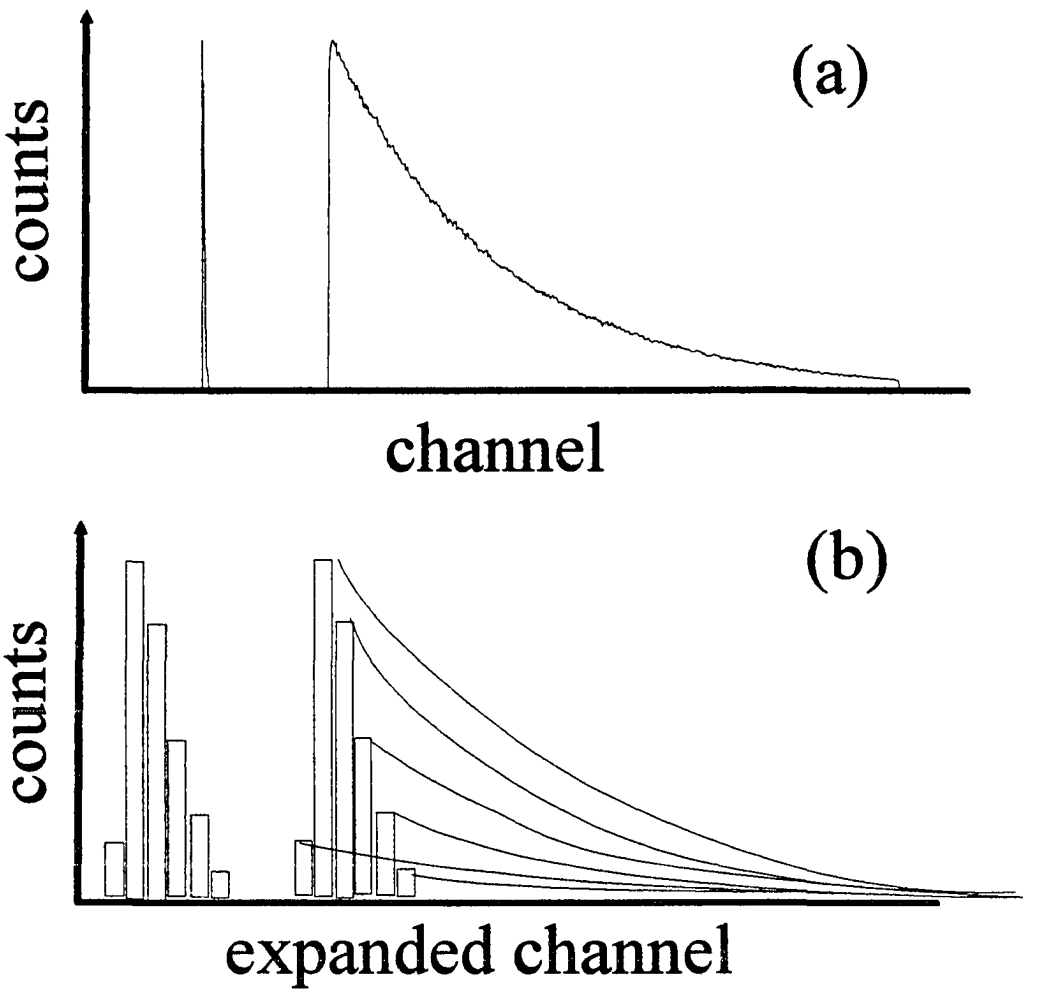

FIGURE 13 (a) illustrates the observed photon counting instrument response function for our apparatus and also an emission curve, respectively from left to right. Both were obtained at a resolution of 40ps/ch. (b) expands each 40 ps channel to emphasize that the instrument response function consists of channels and that each channel of the instrument response function produces an emission curve. The curves observed in (a) are a sum of the convoluted curves in (b).

emphasized in Figure 13b where each channel has an exaggerated width. The actual width of each channel in Figure 13a is 40ps. The intensity (height) of each channel is dependent on the number of counts that were placed in the channel by the MCA. The histogram created by the MCA, I(t), is actually a convolution of the instrument response function, X(t'), and the true decay, p(t-t'). This convolution is described by equation (11)

$$I(t) = \sum_{n} X_n(t')p(t-t') \tag{11}$$

where $X_n(t')$ describes the instrument function in channel n at time t'. For each non zero $X_n(t')$ there is a subsequent emission described by $p(t-t')$ as illustrated in Figure 13b. The observed emission curve $I(t)$ is the sum of the convolution of each $X_n(t')$ with its corresponding emission $p(t-t')$. As the width of the channel approaches zero the sum is replaced with the convolution integral described in equation (12).

$$I(t) = \int_0^t X(t')p(t-t')dt' \tag{12}$$

The experimental optimization method used to determine the true decay p(t) is the sequential simplex method [16].

Consider a system that is a function of two parameters x1 and x2. The response surface of the system is a graph of the system's response, y, as a function of the experimental conditions x_1 and x_2. For example assume x_1 and x_2 describe two parameters in a

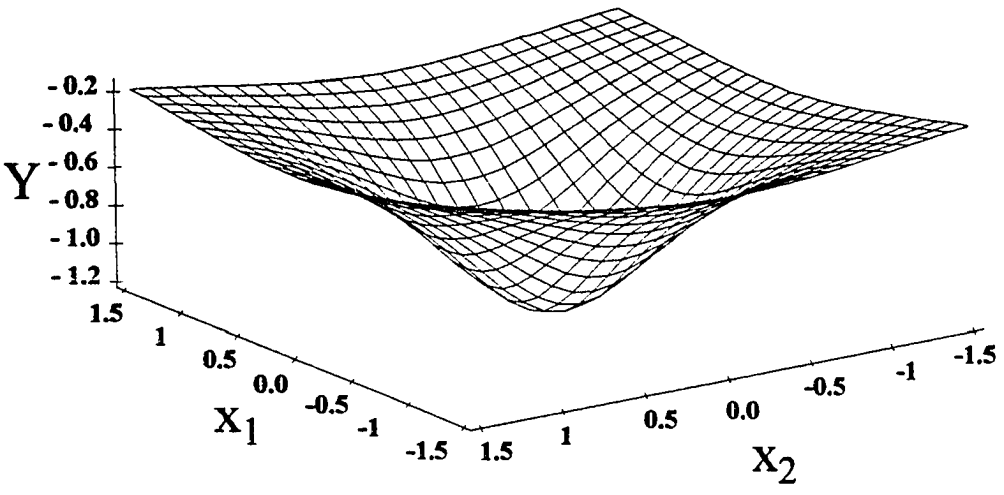

FIGURE 14 Graph of the system response (y) as a function of two system factors x_1 and x_2. The graph was made using Maple V.2 software with the equation $y = \frac{-1}{x_1^2 + x_2^2 + 0.8}$

manufacturing process and the response of the system is the amount of energy required to perform the process. If we assume Figure 14 is the response surface for the manufacturing process then there exists a particular set of experimental conditions such that the minimum energy is required to perform the manufacturing process. There are many methods that can be used to find the minimum or a maximum in a surface including the single factor optimization method [34] and the "shotgun" approach to optimization [35]. Both of these optimization methods have been used in the past however in 1962 Spendley et al. [36] introduced a more efficient method of optimization called the sequential simplex method. A simplex is a geometric Figure that has a number of vertexes equal to one more than the

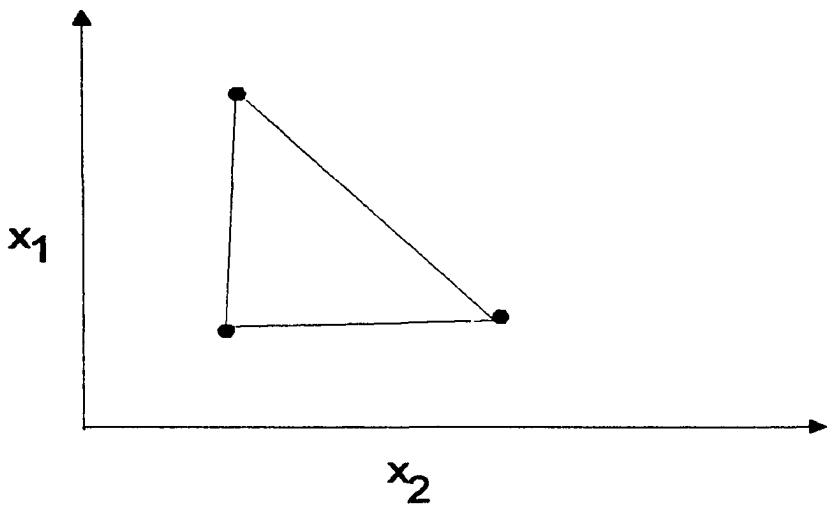

FIGURE 15 Simplex for optimizing function with two parameters is a triangle.

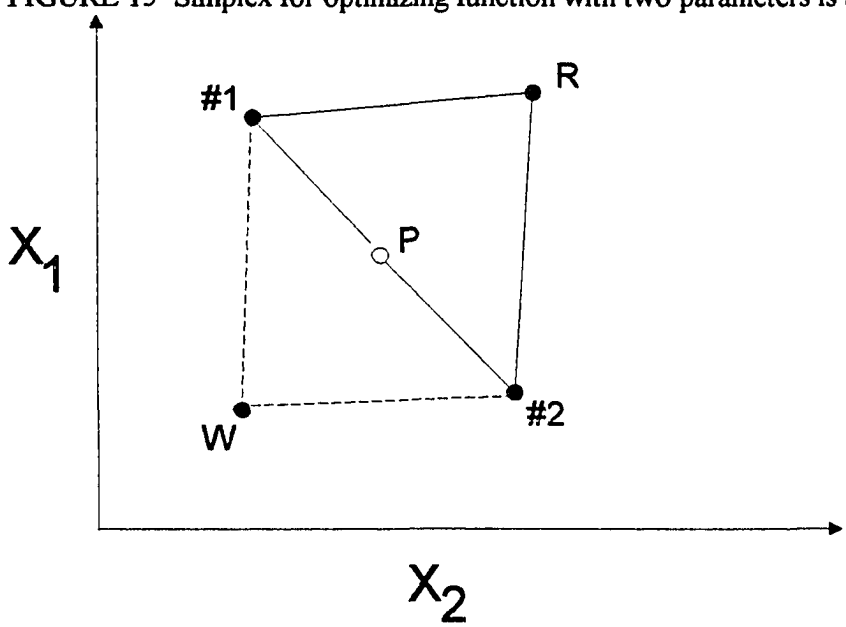

FIGURE 16 The simplex reflection move for system with two parameters showing the vertex with the worst response, **W**, and the vertex found by the reflection operation, **R**. Dashed lines represent the simplex before the reflection operation and solid lines represent the simplex after the reflection operation. The open circle represents the centroid of the simplex before reflection and is found by evaluating the vector average of vertexes #1 and #2.

number of variables in the system. The name 'simplex' is given because a simplex contains the minimum number of points needed to describe a point on the response surface of a system. For example for a one dimensional response surface (a line) the simplex would consist of two points. Two points are the minimum number of points needed to describe a line. To describe a point on a two dimensional response surface the simplex would consist of three points-a triangle. The simplex always contains one more point than the number of variable factors in the system to be optimized. The simplex for the manufacturing process with two variables is pictured in Figure 15. Each vertex of the simplex corresponds to a different set of experimental conditions. The solid lines connecting the vertexes in the simplex have no meaning other than allowing the visualization of the simplex.

Each vertex of a simplex can be designated by a row vector of the coordinates of the vertex. For example the i^{th} vertex in Figure 15 is given the symbol V_i and represented by equation (13)

$$V_i = \left[x_1^i, x_2^i\right] \tag{13}$$

where x_1^i and x_2^i are the coordinates describing the vector V_i. A simplex can be moved into an adjacent area on the factor response surface of a system through the simplex reflection operation with the purpose to approach the optimum response on the response surface. A simplex reflection move is illustrated in Figure 16 where the vertex with the worst response

W is rejected and replaced with a reflected vertex **R**. The dashed lines in Figure 16 represent the old simplex and the solid lines represent the new simplex. The new vertex **R** is found by projecting the position of the rejected vertex through a centroid an equal distance beyond. The centroid of the reflection move in Figure 16 is given the symbol **P.** The position of the centroid is found by rejecting the vertex with the worst response **W** and averaging the remaining vectors of the dashed simplex. Thus the centroid in Figure 16 was found by finding the vector average of vertexes #1 and #2. The reflected vertex, **R**, is found by the vector formula described in equation (14)

$$R = P + (P - W) \tag{14}$$

where **R**, **P**, and **W** are all row vectors. **R** corresponds to a new set of experimental conditions where the system response will be evaluated. The goal of the simplex reflection operations is to move rapidly to the region of the optimum response.

A simplex that can approach the region of optimum response with only the reflection operation is called a "fixed-size" simplex. A fixed-size simplex is inefficient at finding the exact location of the optimum response when in the region of the optimum. A fixed-size simplex may also get "hung-up" because as can be seen from Figure 16 the reflected vertex may be as equally bad of a response as the worst response. Another drawback of the fixed-size simplex is that if the location of the optimum response on the response surface of the

system is far from the original position of the simplex then many calculations (reflection operations) will be required because the simplex cannot change its shape.

Nelder and Mead [37] modified the fixed-size simplex to allow it to expand in directions that are favorable and contract in directions that are unfavorable. The modified simplex no longer has a fixed size but a variable size. A simplex whose size is allowed to vary can accelerate to the optimum response and adapt to different response surfaces [16]. In addition to "reflection" a variable-size simplex has two other operations: "contraction" and "expansion." In the fixed-size simplex **W** was always replaced by **R** to create a new simplex and move closer toward the region of the optimum response. In the variable-size simplex the vertex that replaces **W** may be **R**, an expansion vertex **E**, or one of the contraction vertexes $\mathbf{C_R}$ or $\mathbf{C_W}$ depending on which direction of contraction is more desirable. Figure 17 illustrates the possible moves in the variable size simplex algorithm. The vertexes **P**, **W**, and **R** have identical meanings and definitions in a variable-size simplex as they do in a fixed-size simplex. **B** is the vertex with the best system response and **N** is the vertex with the next-to-worst system response.

The expansion vertex allows the simplex to accelerate to the optimum once the simplex is progressing in the correct direction. **E** is described by the row vector equation (15)

$$E = P + 2(P - W) = R + (P - W) \tag{15}$$

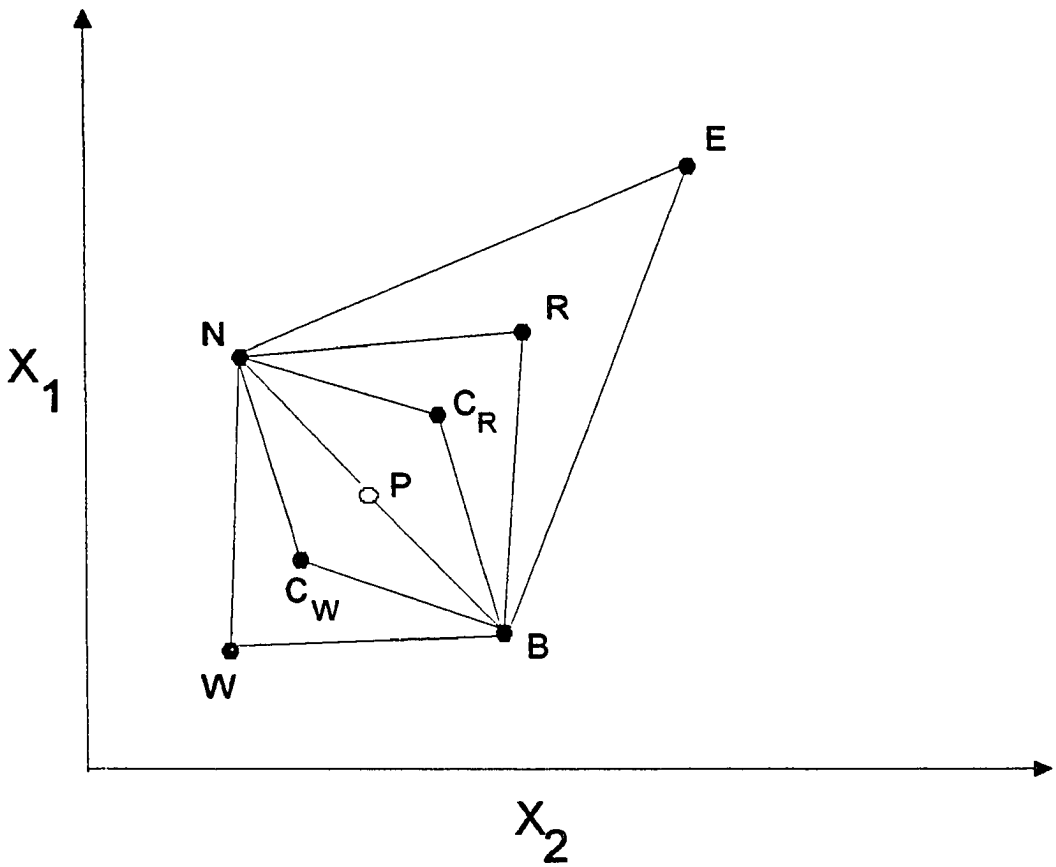

FIGURE 17 Possible moves in the variable-size simplex algorithm. Each vertex is described by a row vector of its coordinates: **P** is the centroid of the remaining hyperface, **B** = best vertex, **N** = next-to-worst vertex, **W** = worst vertex, **R** = reflection vertex, **E** = expansion vertex, $\mathbf{C_R}$ = contraction vertex on the **R** side, $\mathbf{C_W}$ = contraction vertex on the **W** side.

and goes out twice as far from the centroid **P** as the reflection vertex **R**. In Figure 17 if the response at the reflection vertex **R** is better than or equal to the response at the rejected vertex **W** then the **R** side of **P** is more desirable than the **W** side of **P** and the contraction vertex $\mathbf{C_R}$ is a likely choice for the new vertex. If the situation is reversed the vertex $\mathbf{C_W}$ may be a likely choice to replace **W**. The formulas for finding the vertexes $\mathbf{C_R}$ and $\mathbf{C_W}$ are given in the row vector equations (16) and (17).

$$C_R = P + \tfrac{1}{2}(P - W) \tag{16}$$

$$C_W = P - \tfrac{1}{2}(P - W) \tag{17}$$

The algorithm of the variable-size simplex is qualitatively described in table 3. The vertex symbols in table 3 each refer to the system response evaluated at the coordinates of the vertex. Thus table 3 is comparing various system responses and the symbol "<" should be read as "is worse than" and the symbol ">" should be read as "is better than." The symbols "$\leq$" and "$\geq$" should be read respectively as "is worse than or equal to" and "is better than or equal to."

A realistic view of an experimental response surface for a system can be very different from the response surface pictured in Figure 14. A realistic surface may contain plateaus, ridges, and possibly more than one minima or maxima. The response surface may also be

Table 3 Rules for the Variable-Size Simplex [a4]

1. Rank the vertexes of the first simplex on a worksheet in decreasing order of response from best to worst. Label the worst vertex (vertex with the worst response) **W**.

2. Calculate **R**:
   A. If $N \leq R \leq B$, use simplex **B..NR**, and go to step 3.
   B. If $R > B$, calculate and evaluate **E**:
      i. If $E \geq B$, use simplex **B..NE**, and go to step 3.
      ii. If $E < B$, use simplex **B..NR**, and go to step 3.
   C. If $R < N$:
      i. If $R \geq W$, calculate $\mathbf{C_R}$, and use simplex **B..NC**$_\mathbf{R}$ and go to step 3.
      ii. If $R < W$, calculate $\mathbf{C_W}$, and use simplex **B..NC**$_\mathbf{W}$ and to to step 3.

3. Replace **N** with **W** and rank the remaining retained vertexes in order of decreasing response. Go to step 2.

very rough due to experimental noise. For response systems that have a high degree of noise and/or multiple local minima or maxima around the optimal system response, the variable-size simplex optimization method through personal use has proven to be an excellent optimization method. For example when trying to find the optimal minimum on a response surface that has a high degree of noise and many local minima a very large simplex is initially chosen. In this situation a large simplex can be thought of as a big ball and it will "roll" over (disregard) the noise and local minima in search of the optimal minimum on the response surface. Once the simplex finds the true minimum it "falls" into it and contracts in size allowing it to more precisely find the exact location of the optimal minimum. The size of the simplex is dynamic while traveling on the response surface of a system and this dynamic size allows it to efficiently adapt to different response surfaces.

When the experimental data is numerical and not continuous a problem may occur with the simplex method because the simplex calculates the response of the system at each of its vertexes. This problem may be overcome by incorporating an interpolation procedure into the sequential simplex algorithm. Overall through personal use the simplex method has proven to be an efficient optimization method for finding the true decay in our obtained photon counting data.

A computer program called SPECTRA written by Dr. Sergei Savikhin was used to fit our experimental photon counting decay curves. The program uses the sequential variable-size simplex method mentioned above. The program creates a decay curve $S(t)$ described by equation (18)

$$S(t) = \sum_{i=1}^{n}\left[a_i \times \exp\left(-\frac{t}{\tau_i} \right) \right] \qquad (18)$$

where n is the number of exponentials in the decay law and a_i is the excited state amplitude for the excited state lifetime τ_i. The program then convolutes $S(t)$ with the apparatus function (i.e. instrument function) $X(t)$ and adds a background correction. The result is $R(t)$ described in equation (19)

$$R(t) = X(t) \otimes S(t) + Back \times BackSpec(t) \qquad (19)$$

where the second term accounts for the time independent or time dependent background. BackSpec(t) is a time dependent emission spectrum that is input into the SPECTRA program. For example if it is known that emission from the absorption filters is being detected along with emission from the sample then BackSpec(t) would contain the emission spectrum of the absorption filters. SPECTRA varies the amplitude of BackSpec(t) by multiplying it by a number Back to optimize the theoretical background emission. Usually the emission from the absorption filters is blocked so that BackSpec(t) is not needed and is set equal to one (i.e. BackSpec(t) = 1.0) and Back is set to a constant around 2 to 20 counts. SPECTRA finds the best fit R(t) to the experimentally obtained decay curve I(t) using the variable size sequential simplex method. Starting with an initial set of amplitudes and lifetimes for S(t) the variable size simplex uses equation (19) to calculate different convoluted emission curves R(t) by varying the amplitudes and lifetimes of S(t). Once the best fit R(t) to the experimental decay curve I(t) is found then the true decay (deconvoluted) of the sample will be represented by the final decay function S(t) that was used to calculate the final and optimized R(t). The system response that the simplex uses to optimize the lifetimes and amplitudes of the system is the reduced chi-square test. Before discussing the reduced chi-square test it is important to understand the statistical distribution that describes photon counting data.

The probability for observing any specific number of counts in a given channel in the MCA is given by the Poisson probability function [18]. The Poisson distribution assumes

that the average number of successful events is much smaller than the total number of possible events. The probability of observing x events in the time interval t is described by equation (20)

$$P(x,t,\tau) = \frac{1}{x!}\left(\frac{t}{\tau}\right)^{x} \exp\left[-t/\tau\right] \qquad (20)$$

where τ is the mean time interval between events (in our case the lifetime of the excited state of a molecule.) It can be shown that the variance, σ^2, of a Poisson distribution is equal to the mean, μ, of the Poisson distribution ($\sigma^2 = \mu$). Every count in a channel represents an estimate of the mean of the Poisson distribution of counts for that channel. Thus the variance in the number of counts for each channel σ_i^2 equals the number of counts in that channel, N_i. The uncertainty in the number of counts in each channel is then given by equation (21)

$$\sigma_i = \sqrt{N_i} \qquad (21)$$

where σ_i is the standard deviation of channel i. According to equation (21) the relative counting error is larger for channels with fewer counts and smaller for channels with a larger number of counts.

Let us assume (as the method of least squares does) that the optimum fit for a set of data points may be found by minimizing a weighted sum of squares of deviations of the data $I(t_i)$ from the fitting function $R(t_i)$. The weighted sum may be characterized by the variance of the fit s^2 which is an estimate of the parent variance of the data σ^2. σ^2 is a characteristic of the dispersion of the data about the parent distribution and is not descriptive of the goodness of fit. The estimated variance of the fit s^2 however is characteristic of both the spread of the data and the accuracy of the fit. Equation (22) describes s^2

$$s^2 = \frac{1}{\upsilon}\left[\frac{\sum_{i=n_1}^{n_2} \frac{1}{\sigma_i^2}\left[I(t_i) - R(t_i)\right]^2}{\frac{1}{N}\sum_{i=n_1}^{n_2} \frac{1}{\sigma_i^2}}\right] \qquad (22)$$

where υ is the number of degrees of freedom left after fitting N data points (from channel n_1 to channel n_2) to $(p+1)$ parameters $(\text{i.e. } \upsilon = N-(p+1))$ and σ_i^2 is the uncertainty of each data point. The weighting factor w_i for each data point in equation (22) is described by equation (23)

$$w_i = \frac{1/\sigma_i^2}{(1/N)\sum_{i=n_1}^{n_2}\left(1/\sigma_i^2\right)} \qquad (23)$$

where w_i for each data point is the inverse of the uncertainty σ_i^2 for each data point normalized to the average of all the weighting factors. The weighting factors are incorporated in the sum of equation (22) to aid in yielding a fitting function that best represents the parent distribution. The estimated variance of the fit s^2 can be characterized by the statistic chi-square, χ^2 defined in equation (24).

$$\chi^2 \equiv \sum_{i=n_1}^{n_2} \left\{ \frac{1}{\sigma_i^2} \left[I(t_i) - R(t_i) \right]^2 \right\} \tag{24}$$

The relationship between s^2 and χ^2 can be seen by comparing s^2 with the reduced chi-square χ_υ^2 in equation (25)

$$\chi_\upsilon^2 = \chi^2 / \upsilon = s^2 / \overline{\sigma_i^2} \tag{25}$$

where $\overline{\sigma_i^2}$ is the weighted average of the individual variances. When the uncertainties for each data point are equal then $\chi_\upsilon^2 = s^2/\sigma^2$.

$$\overline{\sigma_i^2} \equiv \frac{1}{\frac{1}{N}\sum \frac{1}{\sigma_i^2}} \tag{26}$$

As the mean of the Poisson distribution increases, the Poisson distribution becomes indistinguishable from the Gaussian distribution [38]. The parent variance of a Gaussian distribution is one (i.e. one standard deviation from the mean.) For a best fit s^2 (the estimate of the parent variance) will also be one resulting in a χ_υ^2 value of one. The χ_υ^2 values for photon counting curves thus have a meaning beyond that of a number that when minimized gives the best fitting curve. For example assume the calculated standard deviation for a particular photon counting data set is 0.064 and with 500 degrees of freedom the predicted value of χ_υ^2 is 0.999. If the observed value of χ_υ^2 is 1.138 then the fit will be 2.185 standard deviations from the predicted mean. Of course if no experimental noise were present a perfect fit (i.e. $I(t_i) = R(t_i)$ for every t_i) would result in $\chi^2 = \chi_\upsilon^2 = 0$.

Another criterion that can be used for the comparison of the experimental and theoretical curves is the autocorrelation function described in equation (24).

$$A_n = \frac{2N'}{(N-M)} \frac{\sum_{i=1}^{b} \sqrt{w_i}\left[I(t_i) - R(t_i)\right]\sqrt{w_{i+n}}\left[I(t_{i+n}) - R(t_{i+n})\right]}{\sum_{i=1}^{N'} w_i\left[I(t_i) - R(t_i)\right]^2} \qquad (24)$$

In this function the data is in the range from M to N and N' is the total number of channels. A quality fit should have an autocorrelation function that is randomly distributed about zero.

The autocorrelation function can reveal systematic deviations between the theoretical and experimental curves.

There are two types of noise in time correlated single photon counting experiments. The first is the noise resulting from the dark current of the detector. The dark current originates from the spontaneous emission of electrons in the detector. The effect of this noise is greatly reduced by the mode of operation of the TAC. The dark current signals that are accepted as start signals by the TAC result in a constant background in the MCA window and can be treated in the data analysis if necessary. The second type of noise is the counting error resulting from the Poisson distribution of photon counting data and is more significant than the noise from the detector. It is recommended that single exponential photon counting curves be obtained to a maximum height of 1 or 2 x 10^4 counts to make the counting error negligible [17].

TCSPC has advantages over conventional measurements where the average photomultiplier current is plotted versus time. Photon counting is sensitive because photon counting data can be deconvoluted to separate the effect of the response of the instrumentation from the true decay of the sample. The signal to noise ratio is enhanced for photon counting because the dark current is discriminated against due to the operation of the TAC. A problem with photon counting data is that the detected fluorescence occurs at many wavelengths while the instrument response function is collected only at the excitation wavelength. Any wavelength dependence in the detector will result in error in the final

deconvolution. TCSPC also has difficulty in measuring very long lifetimes because this would require a long time duration between each excitation pulse and although possible the acquisition time for a complete curve would be very long. TCSPC time resolution is also limited and can be seen by the width of the instrument response function as mentioned earlier.

References

1. Casadio, R.; Baccarini-Melandri, A.; Melandri, B. A. *Eur. J. Biochem.* **1974**, 47, 121-128.

2. Deamer, D. W.; Prince, R. C.; Crofts, A. R. *Biochim. Biophys. Acta.* **1972**, 274, 323-335.

3. Capomacchia, A.C.; Casper, J.; Schulman, S. G. *Journal of Pharmaceutical Sciences* **1974**, 63(8), 1273.

4. Capomacchia, A.C.; Schulman, S.G. *Journal of Pharmaceutical Sciences* **1974**, 64(7), 1256.

5. Atwell, G. J.; Cain, B. F.; Baguley, B. C.; Finlay, G. J.; Denny, W. A. *J. Med. Chem.* **1984**, 27, 1481.

6. Denny, W. A.; Graham, J. A.; Rewcastle, G. W.; Baguley, B. C. *J. Med. Chem.* **1987**, 30, 658.

7. Gladstone, H.; Laidler, K. J.; Eyring, H. In *The Theory of Rate Processes* Mc-Graw Hill: New York, NY, **1941**.

8. Frauenfelder, H.; Wolynes, P. G. *Science* July 26, **1985**, 229(4711), 337-345.

9. Hynes, J. T. In *The Enzyme Catalysis Process* Cooper, A.; Houben, J.; Chien, L. Eds., Plenum Press: New York, NY, **1989**, 283-292.

10. Barrow, G. M. In *Physical Chemistry* Mc Graw Hill: New York, NY, **1961**.

11. Borgis, D.; Hynes, J. T. In *The Enzyme Catalysis Process* Cooper, A.; Houben, J.; Chien, L. Eds., Plenum Press: New York, NY, **1989**, 293-302.

12. Borgis, D.; Hynes, J. T. *Chem. Phys.* **1993**, 170, 315-346.

13. Borgis, D.; Hynes, J. T. *J. Chem. Phys.* March, **1991**, 94(5), 3619-3628.

14. Levine, I. N. In *Quantum Chemistry* Prentice Hall: Englewood Cliffs, New Jersey, **1991**.

15. Houben, J. L. In *The Enzyme Catalysis Process* Cooper, A.; Houben, J.; Chien, L. Eds., Plenum Press: New York, NY, **1989**, 275-282.

16. Deming, S. N.; Morgan, S. L. *Analytical Chemistry* March, **1973**, 45(3).

17. O'Connor, D. V.; Phillips, D. In *Time -correlated Single Photon Counting* Academic Press, Inc.:Orlando, Florida, **1984**.

18. Bevington, P. R. *Data Reduction and Error Analysis for the Physical Sciences* McGraw-Hill: New York, NY, **1969**.

19. Schuldiner, S.; Avron, M. *FEBS Letts.* May, **1971**, 14(4), 233.

20. Schuldiner, S.; Rottenberg, H.; Avron, M. *Eur. J. Biochem.* **1972**, 25, 64-70.

21. Faure, R.; Galy, J.P.; Elguero, V. J.; Galy, A. M.; Barbe, *J. Chemica Scripta* **1979**, 15, 62.

22. Bacon, N.; Boulton, A. J.; Brownlee, R.T.C.; Katritzky, A. R.; Topsom, R. D. *J. Chem. Soc.* **1965**, 5230.

23. Mason, S.F.; *J. Chem. Soc.* **1959**, 1281.

24. Acheson, R. M.; Burstall, M. L.; Jefford, C. W.; Sansom, B. F. *J. Chem. Soc.* **1954**, 3742.

25. Short, L. N. *J. Chem. Soc.* **1952**, 4584.

26. Wakelin, L. P. G.; Atwell, G. J.; Rewcastle, G. W.; Denny, W. A. *J. Med. Chem.* **1987**, 30, 855-861.

27. Fleming, G. R. In *Chemical Applications of Ultrafast Spectroscopy* Oxford University Press: New York, NY, **1986**.

28. Anfinrud, P. Doctoral Dissertation, **1987**, Iowa State University.

29. Frey, W.; Laermer, F.; Elsaesser, T. *J. Phys. Chem.* **1991**, 95, 10391-10395.

30. Choi, K. -J.; Boczer, B.; Topp, M. R. In *Ultrafast Phenomena Vol. 4* Austin, D. H.; Eisenthal, K. B. Eds. Springer: Berlin, **1984**, p. 368.

31. Barbara, P. F.; Walsh, P. K. *J. Phys. Chem.* **1989**, 93, 29-34.

32. Barbara, P. F.; Walker, G. C.; Smith, T. P. *Science* May 15, **1992**, 256, 975-981.

33. Strandjord, A. J. G.; Smith, D. E.; Barbara P. F. *J. Phys. Chem.* **1985**, 89, 2362.

34. Friedman, M.; Savage, L. J. In *Techniques of Statistical Analysis* Eisenhart, C.; Hastay, M. W.; Wallis, W. A. Eds., McGraw-Hill: New York, N.Y., **1947**.

35. Walters, F. H.; Parker, L. R. Jr.; Morgan, S. L.; Deming, S. N. In *Sequential Simplex Optimization* Brown, S. D. Ed., CRC Press: Boca Raton, Florida, **1991**.

36. Spendley, W.; Hext, G. R.; Himsworth, F. R. *Technometrics* **1962**, 4(4), 441-461.

37. Nelder, J. A.; Mead, R. *Computer Journal* **1965**, 7, 308.

38. Bevington, P. R.; Robinson, D. K. In *Data Reduction and Error Analysis for the Physical Sciences-2nd Edition* McGraw Hill: New York, NY, **1992**.

39. Rossetti, R.; Haddon, R. C.; Brus, L. E. *J. Am. Chem. Soc.* **1980**, 102, 6913.

40. Itoh, M.; Fujiwara, Y. *J. Phys. Chem.* **1983**, 87, 4558-4561.

41. Laws, W. R.; Brand, L. *J. Phys. Chem.* **1979**, 83, 7, 795-801.

42. Smith, K. K.; Huppert, D.; Gutman, M.; Kaufman, K. J. *Chem. Phys. Lett.* **1979**, 64, 522-527.

43. Ireland, J. F.; Wyatt, P. A. H. *Adv. Phys. Org. Chem.* **1976**, 12, 131-221.

44. E. M. Kosower; Huppert, D. *Ann. Rev. Phys. Chem.* **1986**, 37, 127-156.

45. Brand, L.; Laws, W. R. *NATO Adv. Sci. Inst. Ser. Series A* **1983**, 69, 319-340.

46. Gafni, A.; Brand, L. *Chem. Phys. Lett.* **1978**, 58, 345.

47. Park, H. -R.; Mayer, B.; Wolschann, P.; Köhler, G. *J. Phys. Chem.* **1994**, 98, 6158-6166.

SECTION I. EXCITED STATE KINETICS OF PROTON TRANSFER EQUILIBRIA

INTRODUCTION

The excited state population kinetics of 2-naphthol serves as an excellent introduction into the calculation of excited state lifetimes and amplitudes. The 2-naphthol system contains only two protonation states hence the calculations are simplified.

Two State Equilibria

Figure 1 illustrates the calculated equilibrium ground state populations for the conjugate acid/base equilibrium described by equation (1).

$$BH^+ \leftrightarrow B + H^+ \qquad (1)$$

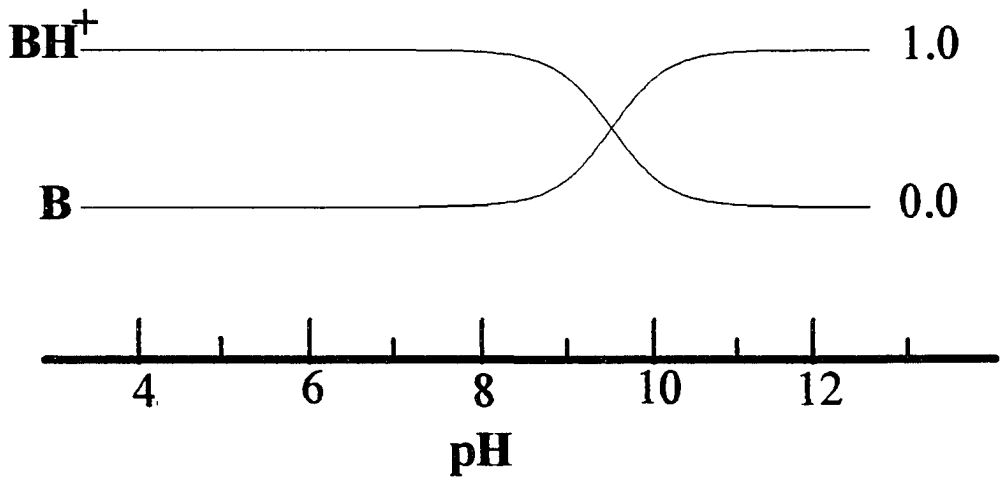

FIGURE 1 Calculated ground state equilibrium populations for a two state system verses pH. The populations are normalized to one and the ground state pK_a equals 9.5.

The curves of Figure 1 were calculated from equations (2) and (3)

$$K_a = \frac{B \times H^+}{BH^+} \tag{2}$$

$$1 = BH^+ + B \tag{3}$$

where B and BH^+ are the populations of the base and acid form, respectively, and H^+ is the hydrogen ion concentration. Equation (3) arises from the normalization of the conjugate acid and base populations to one. Equations (4) and (5) are obtained by solving equations (2) and (3) for B and BH^+.

$$B = \frac{K_a}{K_a + H^+} \tag{4}$$

$$BH^+ = \frac{H^+}{K_a + H^+} \tag{5}$$

Figure 1 was calculated with the ground state pK_a equal to 9.5. It is important to observe in this Figure that for pH values lower than 8 the ground state consists of more than 99 percent BH^+ and for pH values greater than 11 the ground state consists of more than 99 percent B. In the pH region between 8 and 11 populations of both B and BH^+ are significant. The

ground state ionization constant for the equilibrium (pKa = 9.5) occurs in the pH region between 8 and 11 and this is the reason for the nonzero populations of both species. The crossing point in Figure 1 occurs when pH = pKa. At this pH the concentrations of the conjugate acid and base are the same ($[B] = [BH^+]$). If the conjugate acid and base absorb at different wavelengths then a series of absorption spectra taken at increasing pH values will reveal the ground state pKa of the system by observing absorption spectra changes. Such a process is called a spectrophotometric titration.

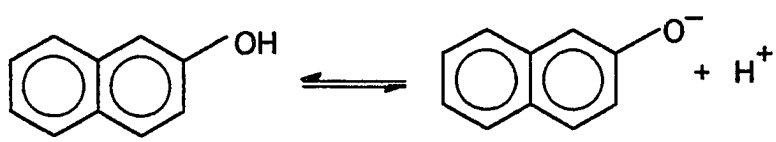

(6)

2-Naphthol exists in equilibrium with its conjugate base naphtholate as described in equation (6). The ground state pKa of 2-naphthol is reported as 9.5 [2]. Thus Figure 1 describes the ground state populations of the 2-naphthol system. A spectrophotometric titration for 2-naphthol is illustrated in Figure 2 for the pH range 2.3 to 11.6. For pH values less than 8.5 Figure 1 predicts the ground state population at equilibrium to be dominated by the conjugate acid. Therefore the absorption curves taken at pH values 2.33 (curve a) through 8.33 (curve f) in Figure 2 must originate from 2-naphthol. As the pH is increased from 8.33 in Figure 2 then absorption from naphtholate becomes significant. Absorption

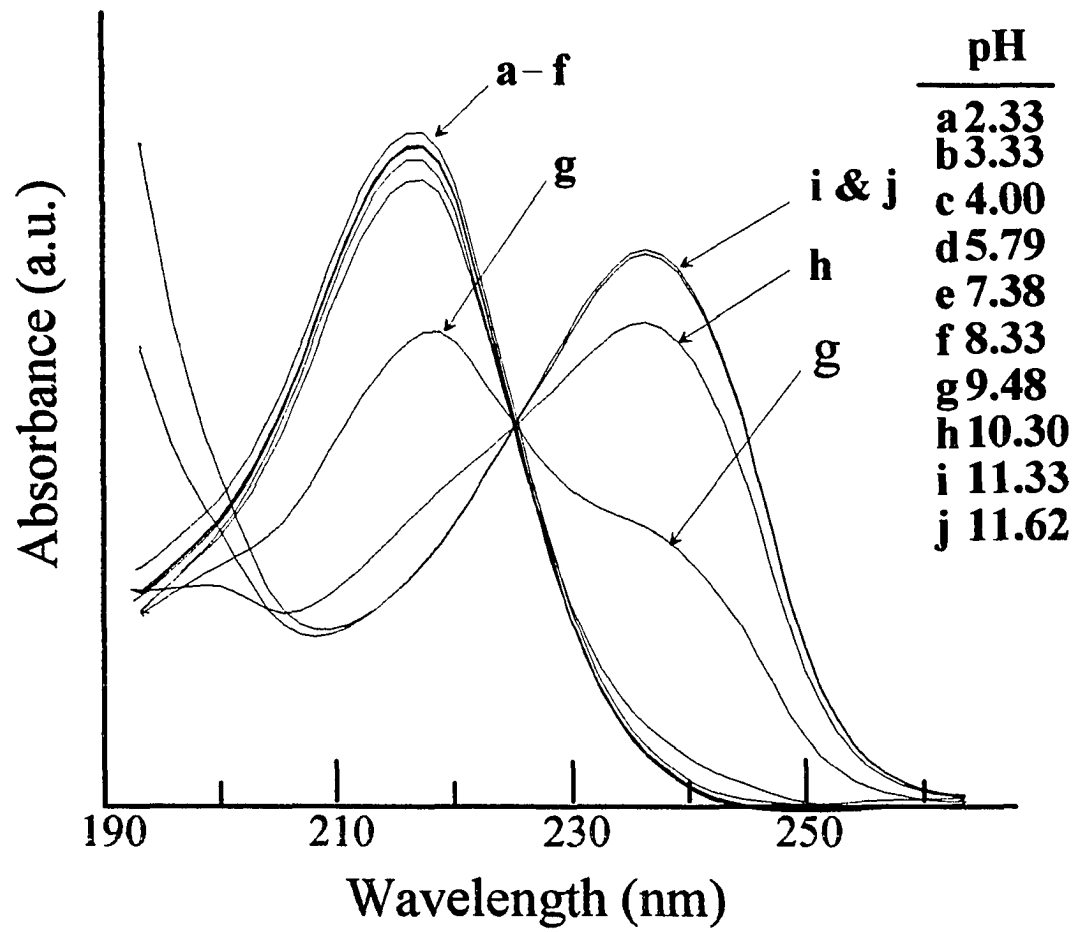

FIGURE 2 Spectrophotometric titration of 2-naphthol obtained on a Perkin Elmer Lambda 3B UV/VIS spectrophotometer. The pH was adjusted by adding small amounts of $HCl_{(aq)}$ and $NaOH_{(aq)}$ to a relatively large volume of an aqueous solution of 2-naphthol to keep concentration changes negligible. The absorption band with peak at ~215nm is that of the acid form, naphthol, and the absorption band with peak at ~240nm is that of the conjugate base, naphtholate. This Figure is used to illustrate isosbestic behavior and does not show the lowest energy bands of 2-naphthol.

from naphtholate is a major component of the absorption curves taken at pH = 9.48 (curve g) and 10.3 (curve h). As the pH is increased further, only the absorption spectra of naphtholate is observed when the pH is greater than 11 as in curves i and j. The ground state pKa in a spectrophotometric titration is reached when the absorption spectrum drastically changes. The ground state pKa determined by Figure 2 is very near that of curve g at a pH of 9.48. At approximately 230nm all the absorption curves in Figure 2 are observed to cross and this crossing point is called an isosbestic point. Isosbestic points occur in absorption spectra when only two absorbing species exist in the ground state equilibrium and both species absorb at different wavelengths.

A fluorometric titration consists of a series of emission spectra taken at different pH values. The excited state ionization constant can be determined through a fluorometric titration if one or both species fluoresce. The excited state ionization constant of 2-naphthol was found by fluorometric titration to be 2.8 [1]. The ground state pKa of the 2-naphthol system is 9.5; thus, there is a large difference between the ground and excited state ionization constants, Ka and Ka^* respectively, of 2-naphthol. Differences between Ka and Ka^* of six to ten orders of ten are not uncommon in many compounds [2].

Proton transfer occurs in the excited state of a conjugate acid/base equilibrium due to the difference between the ground and excited state ionization constants. Figure 3 represents the calculated ground and excited state populations of the 2-naphthol system at equilibrium. In Figure 3 BH^+ and B represent naphthol and naphtholate, respectively, in the ground state

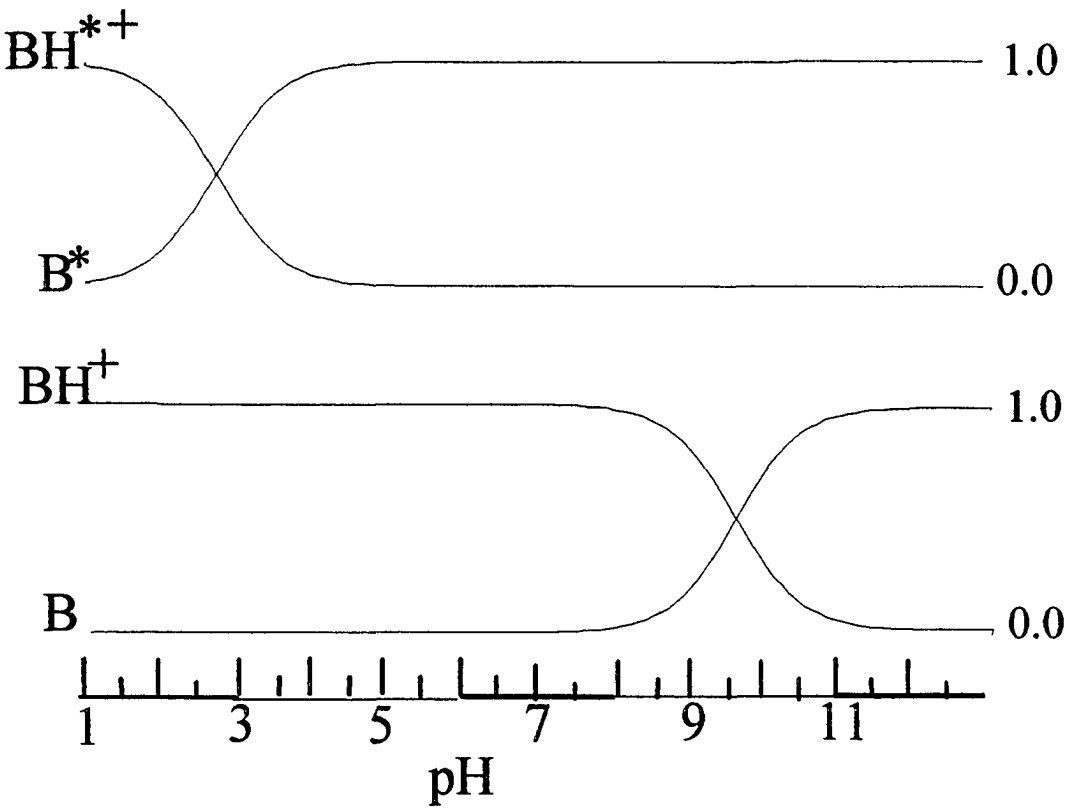

FIGURE 3 The top two curves represent the excited state equilibrium populations verses pH for a conjugate acid/base pair with $pKa^* = 2.8$. The bottom two curves represent the ground state populations at equilibrium verses pH for an acid/base pair with pKa = 9.5. The ground and excited state populations are separately normalized to one.

with pKa = 9.5 and BH^{+*} and B^* represent naphthol and naphtholate, respectively, in the excited state with pKa^*= 2.8. Naphthol is a stronger acid in the excited state than in the ground state because $pKa^* < pKa$. This tendency is revealed in Figure 3 where naphthol is shown to form naphtholate in the excited state when above pH ~3. The absorption spectrum of naphthol in Figure 1 is at a higher energy than the absorption spectrum of naphtholate. Thus upon excitation naphthol will be at a higher energy than its conjugate base and will tend to lose a proton to form excited naphtholate at a lower energy.

The Förster cycle is a thermodynamic relation that predicts the difference between the ground and excited state ionization constants when the individual absorption and emission maxima are known for the conjugate acid/base pair. The Förster cycle is illustrated in Figure 4 where ΔE_{BH^+} and ΔE_B are the energy differences between the zero point vibrational levels of the ground and excited states for the conjugate acid and base, respectively [1-3]. Absorption usually occurs from the zero point vibrational level of the ground state to a nonzero vibrational level of the excited state and emission usually occurs from the zero point vibrational level of the excited state to a nonzero vibrational level in the ground state. Hence the zero point energy difference is usually unknown and must be estimated for most compounds. The estimated zero point energy difference for the conjugate acid ΔE_{BH^+} is described by equation (7) where the absorption and emission maxima for BH^+ are $\upsilon_{abs}^{BH^+}$ and $\upsilon_{em}^{BH^+}$, respectively.

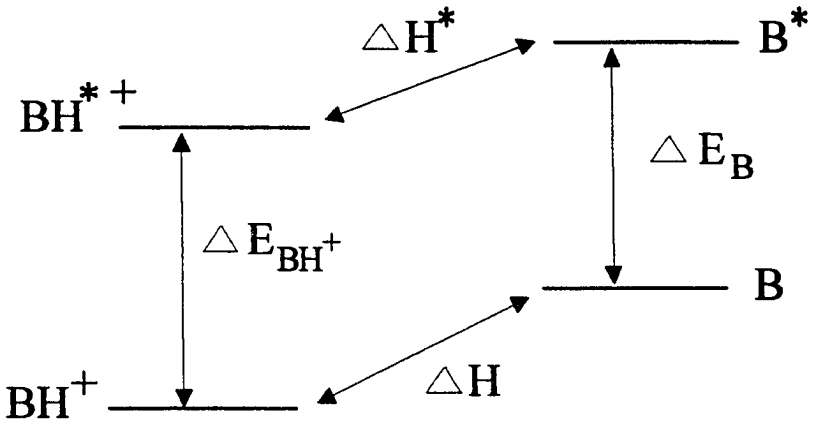

FIGURE 4 Förster cycle where BH^+ and B designate the respective acid and base form in the ground state. BH^{*+} and B^* represent the respective acid and base forms in the excited state. ΔE_{BH^+} and ΔE_B represent the zero point energy differences between the ground and excited states for the conjugate acid and base, respectively. ΔH and ΔH^* are the heats of ionization for the ground and excited states, respectively, h is Planck's constant and c is the speed of light.

$$\Delta E_{BH^+} \approx \frac{hc\left(\upsilon_{abs}^{BH^+} + \upsilon_{em}^{BH^+}\right)}{2} \qquad (7)$$

The estimated zero point energy difference for the conjugate base ΔE_B is described by equation (8) where the absorption and emission maxima for B are υ_{abs}^{B} and υ_{em}^{B}, respectively.

$$\Delta E_B \approx \frac{hc\left(\upsilon_{abs}^{B} + \upsilon_{em}^{B}\right)}{2} \qquad (8)$$

From Figure 4 we may write equation (9):

$$\Delta H - \Delta H^* = \Delta E_{BH^+} - \Delta E_B \qquad (9)$$

where ΔH and ΔH^* are the respective heats of ionization for the ground and excited states. The Gibbs free energy function is related to the thermodynamic equilibrium constant K through equation (10) [4]

$$\Delta G = -RT\ln(K) \qquad (10)$$

$$\Delta G = \Delta H - T\Delta S \tag{11}$$

where R is the gas constant and T is the temperature. Combining equations (9), (10) and the Gibbs relation (11) will result in equation (12)

$$\Delta H - \Delta H^{*} = \Delta E_{BH^{+}} - \Delta E_{B} = T\left(\Delta S - \Delta S^{*}\right) - RT \ln\left(K/K^{*}\right) \tag{12}$$

where ΔS, ΔS^{*}, K and K^{*} are the ground and excited state reaction entropies and ionization constants, respectively. If equal reaction entropies are assumed in the ground and excited states then equation (12) becomes equation (13).

$$\frac{\Delta E_{BH^{+}} - \Delta E_{B}}{RT} = \ln\left(K^{*}/K\right) \tag{13}$$

Substituting equations (7) and (8) into equation (13) results in equation (14)

$$\ln\left(K^{*}/K\right) = \left(hcN/RT\right)\left[\left(\upsilon_{abs}^{BH^{+}} + \upsilon_{em}^{BH^{+}} - \upsilon_{abs}^{B} - \upsilon_{em}^{B}\right)/2\right] \tag{14}$$

where h is Planck's constant, c is the speed of light, and N is Avogadro's number. If the units of h are in erg·sec/molecule, c is in cm/s, and the natural logarithm of equation (14) is converted to the base ten logarithm then equation (14) becomes equation (15).

$$pK - pK^* \approx \left(0.625/T\right)\left[\left(\upsilon_{abs}^{BH^+} + \upsilon_{em}^{BH^+} - \upsilon_{abs}^{B} - \upsilon_{em}^{B}\right)/2\right] \qquad (15)$$

The Förster cycle described by equation (15) predicts the difference between the ground and excited state ionization constants when the absorption and emission maxima are known for the conjugate acid base pair. Even though the Förster cycle may predict a nonzero difference between the ground and excited ionization constants, proton transfer may not take place in the excited state. Proton transfer may not occur because the Förster cycle does not take into account the relative rates of the excited state processes occurring in the excited state. The excited state may exist for only a very short period of time with the result that equilibrium is not attained in the excited state. This nonequilibrium condition occurs in the excited state of 2-naphthol. According to Figure 3 at pH = 7.5 only naphtholate will exist in the excited state upon equilibration. When naphthol is directly excited at pH = 7.5 emission from both naphthol and naphtholate is observed [5]. The proton transfer in the excited state of 2-naphthol is thus kinetically limited by the quenching, fluorescence, and protonation/deprotonation reaction rates in the excited state.

Excited state protonation/deprotonation rate constants, ionization constants, and excited state lifetimes and amplitudes may be found through kinetic investigations by time resolved fluorescent techniques such as time correlated single photon counting. Figure 5 is a general kinetic scheme for a conjugate acid/base pair in their ground and excited states. The upper equilibrium in Figure 5 depicts the excited state and the lower equilibrium depicts the ground state. Upon excitation the excited acid, BH^{*+}, may leave the excited state through fluorescence or quenching. These two processes have a combined rate constant designated as k_{BH^+}. BH^{*+} may instead lose a proton to form the excited conjugate base, B^*. This excited state deprotonation reaction is described by the rate constant k_1. B^* may reach the ground state through fluorescence or quenching with the combined rate constant k_B. B^* may also recombine with a proton to form BH^{*+} as designated by the bimolecular rate constant k_2. The differential rate expressions describing the decay of BH^{*+} and B^* are described by equations (16) and (17), respectively.

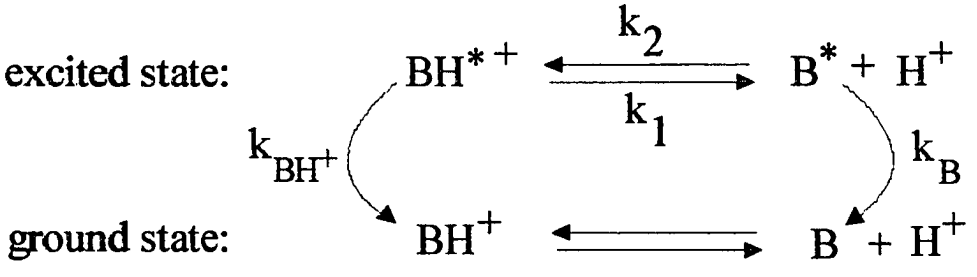

FIGURE 5 A kinetic model which designates the excited state rate constants for a few of the processes that may occur in a two state system.

$$-\frac{dBH^{*+}}{dt} = \left(k_{BH^+} + k_1\right)BH^{*+} - \left(k_2 \cdot H^+ \cdot B^*\right) \tag{16}$$

$$-\frac{dB^*}{dt} = \left(k_B + k_2 \cdot H^+\right)B^* - \left(k_1 \cdot BH^{*+}\right) \tag{17}$$

Solution of equations (16) and (17) leads to expressions of the form:

$$I_{BH^{*+}}(t) = \alpha_1 \exp\left[-t/\tau_1\right] + \alpha_2 \exp\left[-t/\tau_2\right] \tag{18}$$

$$I_{B^*}(t) = \beta_1 \exp\left[-t/\tau_1\right] + \beta_2 \exp\left[-t/\tau_2\right] \tag{19}$$

where $I_{BH^{*+}}(t)$ and $I_{B^*}(t)$ are the respective fluorescence intensities due to BH^{*+} and B^* at time t. The lifetimes, τ_1 and τ_2 along with the amplitudes, α_1, α_2, β_1, and β_2, are functions of the designated rate constants in Figure 5 and the pH. Equations (18) and (19) reveal that the time correlated fluorescence intensity decays of both BH^{*+} and B^* will be biexponential because each species has two identical excited state lifetimes, τ_1 and τ_2. A biexponential decay will always be detected in this system regardless of the detection wavelength with the exception of a single wavelength [5]. In equations (18) and (19) an individual amplitude results for each of the identical lifetimes of the two species. Thus the

excited state kinetics of a two state system results in a biexponential decay and a total of four excited state amplitudes.

The solution of differential equations is often complicated and not quickly done. Finding a solution to the set of differential equations (16) and (17) is simplified with the utilization of the Laplace transform. The Laplace transform [6] of a function is defined in equation (19a)

$$f(s) = \mathcal{L}\{F(t)\} = \int_0^\infty e^{-st} F(t)dt \qquad (19a)$$

where $f(s)$ is the Laplace transform of the function $F(t)$. The Laplace transform of a derivative is described by equation (19b)

$$\mathcal{L}\left\{\frac{dF}{dt}\right\} = sf(s) - F(0) \qquad (19b)$$

where $F(0)$ is the value of the function being integrated at time $t = 0$. A set of differential equations may thus be converted to a set of algebraic equations in s through the use of the Laplace transform.

In order to find the theoretical excited state lifetimes τ_1 and τ_2 the Laplace transform is initially used and equations (16) and (17) become equations (20) and (21). $\mathcal{L}_{BH^{*}{}_{+}}$ and $\mathcal{L}_{B^{*}}$

are the respective Laplace transforms of the excited state populations of the acid BH^{*+} and base B^{*}.

$$-s\cdot\mathcal{L}_{BH^{*+}} + BH_0^{*+} = \left(k_{BH^+} + k_1\right)\mathcal{L}_{BH^{*+}} - \left(k_2\cdot H^+\cdot\mathcal{L}_{B^*}\right) \tag{20}$$

$$-s\cdot\mathcal{L}_{B^*} + B_0^{*} = \left(k_B + k_2\cdot H^+\right)\mathcal{L}_{B^*} - \left(k_1\cdot\mathcal{L}_{BH^{*+}}\right) \tag{21}$$

BH_0^{*+} and B_0^{*} are the respective initial excited state populations of the acid and its conjugate base. Equations (20) and (21) are solved for the initial populations resulting in equations (22) and (23), respectively.

$$BH_0^{*+} = \left(k_{BH^+} + k_1 + s\right)\mathcal{L}_{BH^{*+}} \qquad -\left(k_2\cdot H^+\right)\mathcal{L}_{B^*} \tag{22}$$

$$B_0^{*} = \qquad -k_1\mathcal{L}_{BH^{*+}} \qquad +\left(k_B + k_2\cdot H^+ + s\right)\mathcal{L}_{B^*} \tag{23}$$

$$\begin{vmatrix} \left(k_{BH^+} + k_1 + s\right) & -k_2 \\ -k_1 & \left(k_B + k_2\cdot H^+ + s\right) \end{vmatrix} = 0 \tag{24}$$

If BH_0^{*+} and B_0^{*} are set to zero then the determinant of the coefficients of equations (22) and (23) is described by equation (24). The determinant results in a pH dependent quadratic

equation in s. The quadratic equation may then be solved by using the quadratic formula. The negative inverses of the two solutions are the pH dependent lifetimes of the system. This can easily be shown through Cauchy's Residue theorem [8,9] which will be discussed later in this section using equations (78) through (81). The behavior of the two pH dependent lifetimes for this system are illustrated in Figure 6. The curves of Figure 6 were calculated with a Borland C++ program that is described in the section appendix. The theoretical lifetimes were calculated as a function of pH with the rate constants fixed at the following values: $k_1 = 0.051 ns^{-1}$, $k_2 = 0.50 M^{-1} ns^{-1}$, $k_{BH^+} = 0.149\ ns^{-1}$, and $k_B = 0.11\ ns^{-1}$. The excited state ionization constant pK_a^* was fixed at the value 2.8. The fixed values of the rate constants and the excited state ionization constant used to calculate Figure 6 are the literature values reported for 2-naphthol [5]. Thus Figure 6 represents the theoretical excited state lifetimes for the 2-naphthol system as a function of pH.

The detailed method of determining the four pH dependent amplitudes is discussed in detail later in this section of the dissertation leaving the interpretation of the amplitude calculations to be emphasized here. The amplitude calculations require the fixed values of the rate constants, the ionization constant, and the initial excited state populations. In the amplitude calculations the initial excited state populations of naphthol and naphtholate were normalized to one and it is assumed that only naphthol is directly excited meaning that BH_0^{*+} and $BH_0^{*+} = 1.0$ and $B_0^* = 0.0$. Figure 7 is a plot of the theoretical excited state amplitudes of equations (18) and (19). Equivalent values for the rate constants and excited

state ionization constant were used to calculate both Figures 6 and 7. Therefore Figure 7 represents the theoretical amplitudes for the 2-naphthol system as a function of pH. In Figure 7 when pH < 1.0 there is only one non zero amplitude that being α_2 because both β_1 and β_2 approach zero in this pH region. Thus any emission observed from the naphthol system when pH < 1.0 will be single exponential in character and be due solely to either naphthol or naphtholate. Figure 3 told us that for pH values less than one the formation of excited naphthol is strongly favored in the excited state (i.e. the excited back reaction dominates: $BH^{*+} \leftarrow B^* + H^+$). This suggests that the emission observed for pH < 1.0 is from naphthol and not naphtholate. Therefore the lifetime τ_2 associated with the amplitude α_2 when pH < 1.0 is assigned to be the lifetime of 2-naphthol and is described by the upper lifetime curve (~7.2ns) of Figure 6 at low pH values. Both the ground and the excited state favor the formation of naphtholate for pH values greater than 10 as illustrated in Figure 3. For such high pH values the forward reaction $BH^{*+} \rightarrow B^* + H^+$ dominates and any observed emission will be due solely to naphtholate. The lifetime of naphtholate may be read from Figure 6 by the upper lifetime curve (~9.4ns) at high pH values. From Figures 3 and 7 it is seen that in the pH region between 1 and 4 the excited state reaction is reversible and the emission of both naphthol and naphtholate will have bi-exponential decay laws.

The lower lifetime curve in Figure 6 may be divided into two regions. For pH values less than 2.8 the lower lifetime curve represents the rate of naphtholate combining with a proton to form naphthol. For pH values greater than 2.8 the direction of the proton transfer

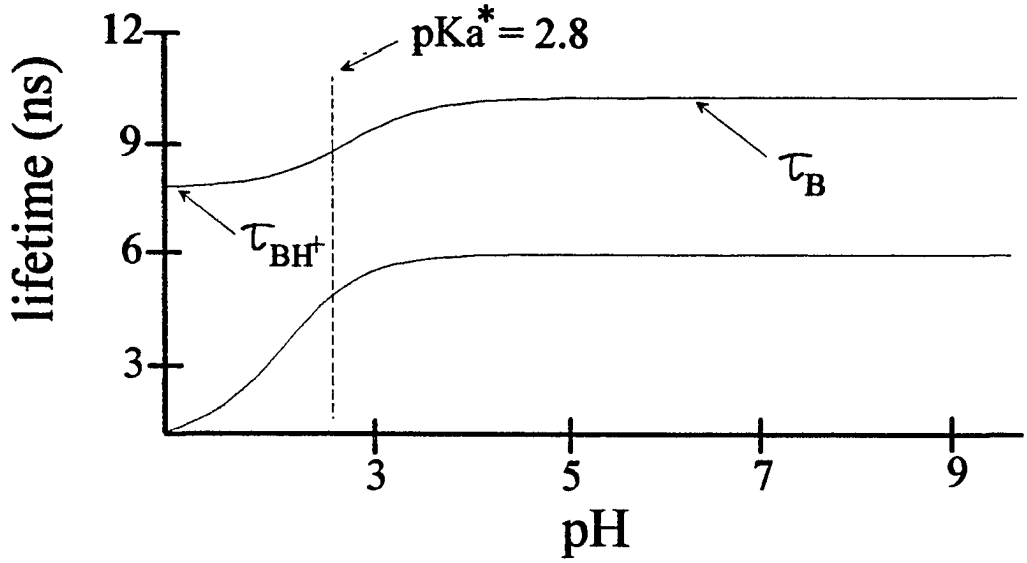

FIGURE 6 The lifetimes of the excited state are calculated as a function of pH. The upper curve represents initially the lifetime of 2-naphthol and at higher pH values it becomes the lifetime of naphtholate. The lower curve illustrates the rate of decay of naphthol and the rise of the naphtholate excited state population.

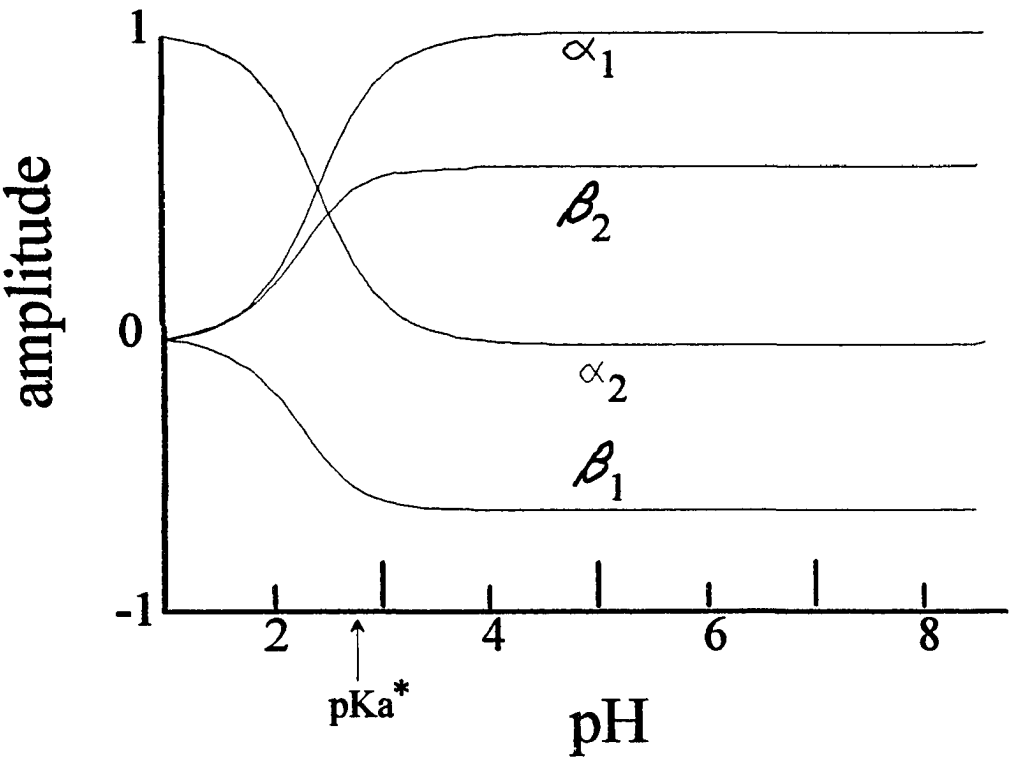

FIGURE 7 The excited state amplitudes are calculated as a function of pH. The calculations were made with the same parameters used for Figure 6 with the additional requirement that only naphthol is directly excited and the excited populations are normalized to one.

is reversed and the forward reaction begins to dominate where naphtholate is formed from naphthol. Thus for pH values greater than 2.8 the lower lifetime curve represents the rate of decay of the naphthol excited state population and the rise of the naphtholate excited state population.

The compound 2-naphthol tends to lose a proton in the excited state because $pK_a^* < pK_a$. The situation is reversed for a compound like acridine. Large heterocyclic molecules like acridine tend to gain a proton in the excited state [1]. The ground state ionization constant for acridine is 5.5 and its excited state ionization constant is 10.7. The equilibrium populations for acridine in the ground and excited state have been calculated and are illustrated in Figure 8. In the acridine system the excited state forward reaction is a second order protonation reaction that depends on the concentrations of acridine and the hydrogen ion. In the pH region between six and nine excited state protonation should occur from the thermodynamic point of view of Figure 8. However emission from the protonated form of acridine is not observed when $6 < pH < 9$ [1]. In this pH region the emission from the protonated form of acridine is not observed due to the very short lifetime of acridine's excited state. Through the addition of ammonium nitrate the hydrogen ion concentration is increased without a concomitant increase in pH. This allows the excited state protonation reaction to occur within the short time duration of the excited state and emission from the protonated acridine to be observed [1].

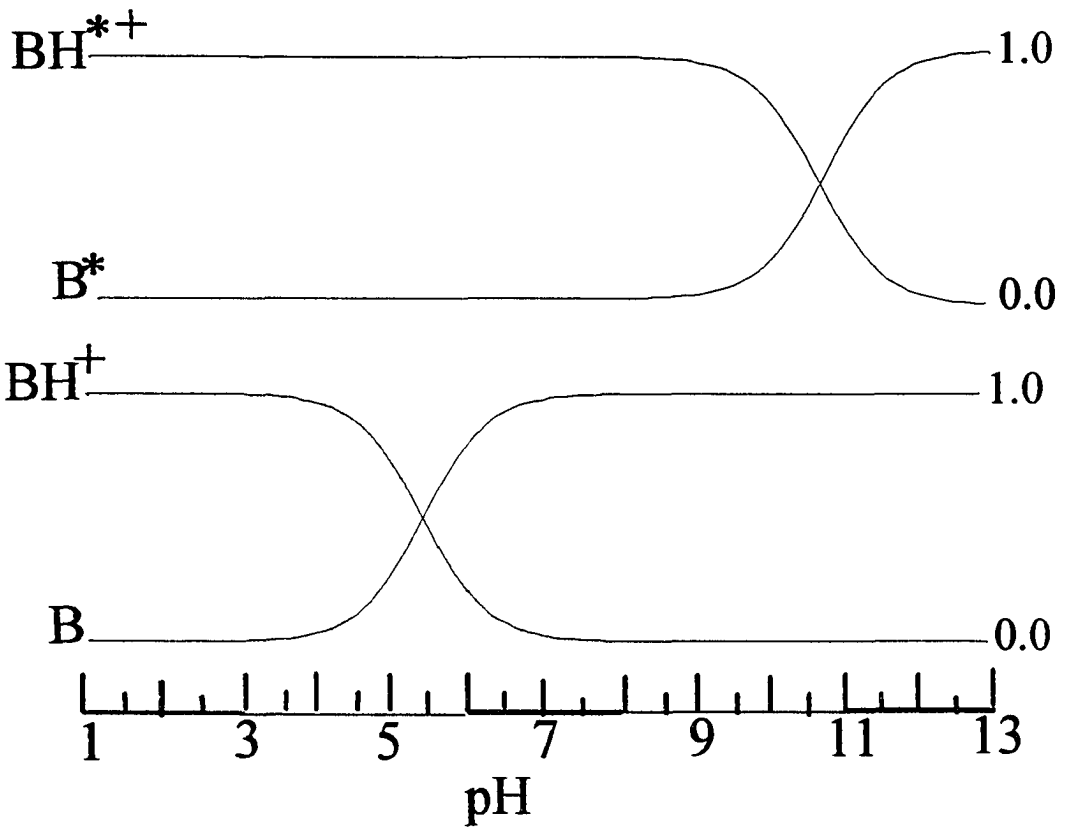

FIGURE 8 The top two curves represent the excited state populations expected if equilibrium is attained for the conjugate acid/base pair in the acridine system verses pH. The bottom two curves represent the ground state populations at equilibrium verses pH for the acid/base pair. The curves were calculated with a ground state $pK_a = 5.5$ and an excited state $pK_a^* = 10.7$. The calculated populations are normalized to one.

Overall, the fluorescence intensity decay from a two state reversible system such as 2-naphthol is characterized by a double exponential decay law. Each emitting species is associated with an identical set of two lifetimes. These decay times are independent of emission wavelength. Four excited state amplitudes will be required to describe the excited state populations of a two state system. Both the lifetimes and the excited state amplitudes are functions of the rate constants, the ionization constant, and the pH. In the case of 2-naphthol the rate constant designating the back reaction is pH dependent because $pK_a^* < pK_a$. A kinetic investigation of the decay parameters of a kinetic model reveals the theoretical excited state lifetimes of each emitting species and the ionization constant of the system.

Four State Sequential Proton Transfer Equilibria

The naphthol/naphtholate system is very simple in that there are only two protonation states in the excited state involving a single ionization constant. The system requires solving a quadratic equation to determine the theoretical lifetimes of the excited state. The excited state kinetics of many other systems are much more complicated because they may involve multiple proton transfers, and/or tautomerization. Such processes quickly increase the difficulty in finding solutions to the set of differential rate equations extracted from the chosen kinetic model.

(a)

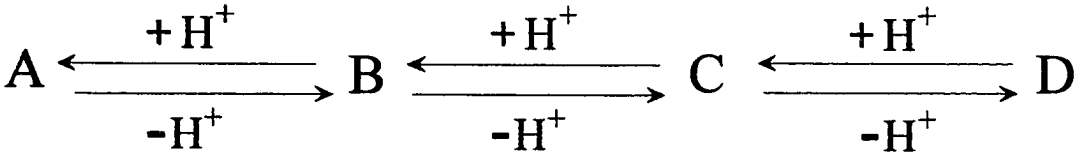

(b)

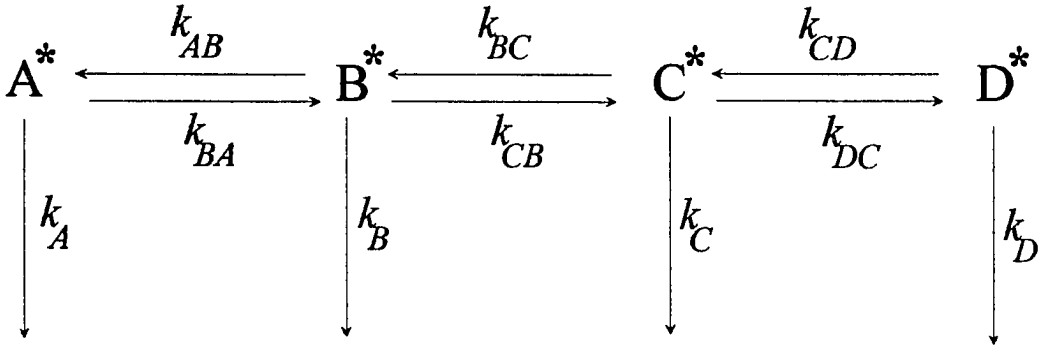

FIGURE 9(a) Model for a 4 species, sequential ionization equilibrium. The Figure emphasizes the proton transfer direction. Calculations of the ground and excited state equilibrium populations for this model are described in the text. (b) Kinetic model for a 4 species excited state equilibrium. Only the equilibrium occurring in the excited state is shown here. See text for a complete description of the designated excited state rate constants. The direction of the proton transfers is indicated in Figure 9a.

The equilibrium ground state populations of the four species designated in Figure 9a may be calculated in an analogous fashion as that shown for the ground state populations of the 2-naphthol system.

$$K_{a1} = \frac{B \times [H^+]}{A} \tag{25}$$

$$K_{a2} = \frac{C \times [H^+]}{B} \tag{26}$$

$$K_{a3} = \frac{D \times [H^+]}{C} \tag{27}$$

$$1.0 = A + B + C + D \tag{28}$$

In equations (25) through (28) K_{a1}, K_{a2}, and K_{a3} are the ground state ionization constants, A, B, C, and D are the ground state populations, and $[H^+]$ is the hydrogen ion concentration. Equations (25) through (27) originate from the three proton transfer equilibria in Figure 9a and equation (28) normalizes the ground state populations to one. Utilization of Maple V.2 software allows equations (25) through (28) to be solved for the ground state populations. The relations are equations (29) through (32).

$$A = \frac{\left[H^+\right]^3}{K_{a1} \times \left[H^+\right]^2 + K_{a1} \times K_{a2} \times \left[H^+\right] + K_{a1} \times K_{a2} \times K_{a3} + \left[H^+\right]^3} \quad (29)$$

$$B = \frac{K_{a1} \times \left[H^+\right]^2}{K_{a1} \times \left[H^+\right]^2 + K_{a1} \times K_{a2} \times \left[H^+\right] + K_{a1} \times K_{a2} \times K_{a3} + \left[H^+\right]^3} \quad (30)$$

$$C = \frac{K_{a1} \times K_{a2} \times \left[H^+\right]}{K_{a1} \times \left[H^+\right]^2 + K_{a1} \times K_{a2} \times \left[H^+\right] + K_{a1} \times K_{a2} \times K_{a3} + \left[H^+\right]^3} \quad (31)$$

$$D = \frac{K_{a1} \times K_{a2} \times K_{a3}}{K_{a1} \times \left[H^+\right]^2 + K_{a1} \times K_{a2} \times \left[H^+\right] + K_{a1} \times K_{a2} \times K_{a3} + \left[H^+\right]^3} \quad (32)$$

Equations (29) through (32) can be used to calculate the theoretical ground state equilibrium populations of species A through D for any given pH and set of ground state ionization constants. The relative excited state equilibrium populations may be calculated in a similar fashion if the system remains in the excited state long enough to attain equilibrium. The excited state equilibrium populations can be described through equations (29) through (32) by replacing A, B, C, and D with their respective excited populations

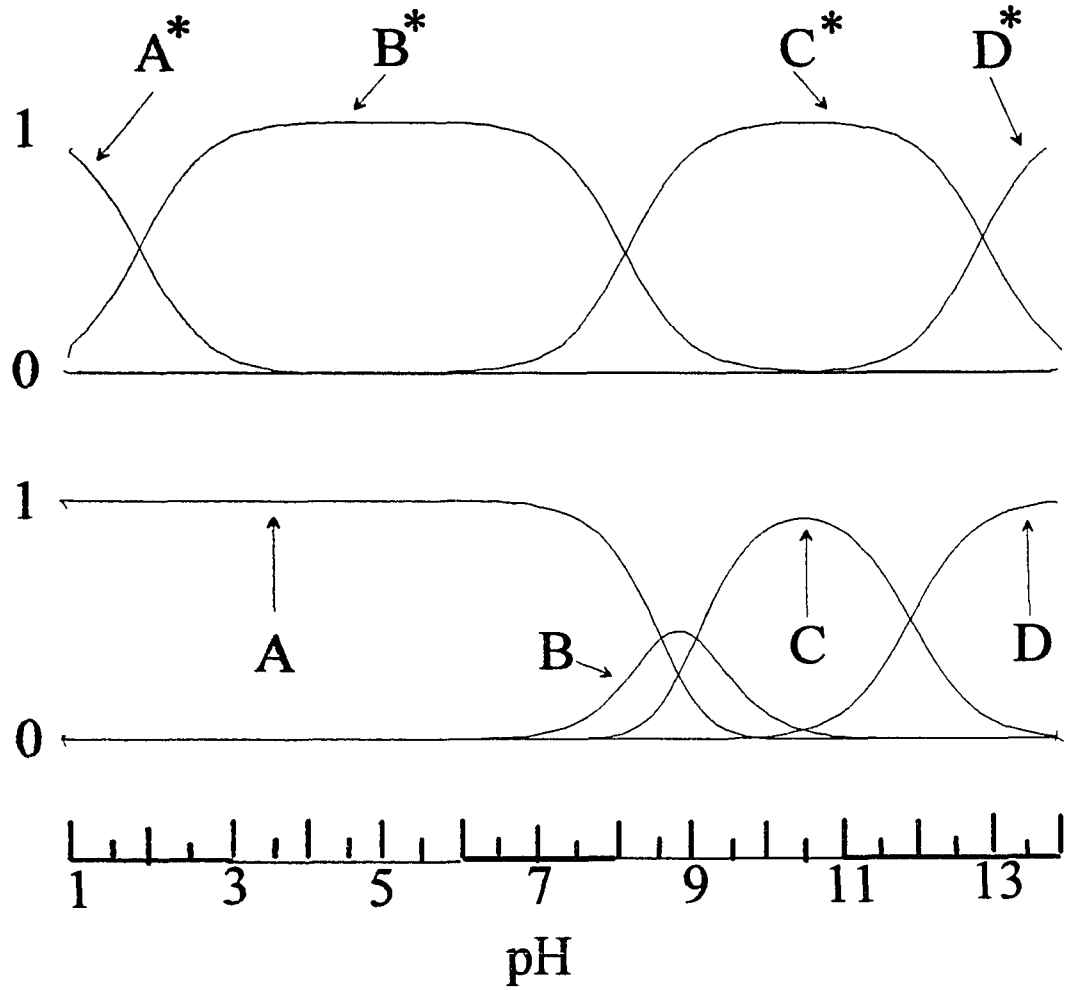

FIGURE 10 The bottom four curves represent the calculated ground state populations of the four species, A, B, C, and D at equilibrium. The top four curves represent the calculated excited state populations (A^*, B^*, C^*, and D^*) expected if equilibrium is attained in the excited state. The ground and excited state ionization constants used in the calculations of the above equilibrium population curves are stated in the text and are the optimum values for the excited state kinetics of the compound 4-2C in the first manuscript. The populations in the ground and the excited state are separately normalized to one.

A^*, B^*, C^*, and D^*. The ground state ionization constants must also be replaced with their respective excited state counterparts K^*_{a1}, K^*_{a2}, and K^*_{a3}.

Figure 10 is an illustration of the theoretical ground and excited state equilibrium populations verses pH for the model in Figure 9a for a particular set of ionization constants. This model was found to agree with the experimental data found for the 9-aminoacridine carboxamides discussed in the first manuscript. The excited and ground state ionization constants used to calculate Figure 10 are the optimum values found for the carboxamide 4-2C and are: $pK^*_{a1} = 2$, $pK^*_{a2} = 8.3$, and $pK^*_{a3} = 13$, $pK_{a1} = 8.8$, $pK_{a2} = 9.25$, and $pK_{a3} = 12$. The bottom four curves of this Figure illustrate the theoretical ground state equilibrium populations of the four species as a function of pH. The top four curves of Figure 10 illustrate the theoretical excited state equilibrium populations assuming equilibrium is attained in the excited state. According to this Figure if equilibrium does occur in the excited state then excited species D^* is predominant when the pH is higher than pK^*_{a3}. Species C^* will predominate when the pH is between pK^*_{a3} and pK_{a2} and species B^* is predominant in the pH region between pK^*_{a2} and pK^*_{a1}. Species A^* is predominant for pH values less than pK^*_{a1}. The theoretical ground state equilibrium populations in Figure 10 appear much more complicated than the excited state populations due to the relatively close nature of the ground state pKa values. Near pH = 9 there are three species present in the ground state at equilibrium: A, B, and C.

Figure 9b designates a selection of the excited state processes that may occur in a system with three sequential proton transfer reactions in the excited state. Figure 9b agrees with the time correlated fluorescence data of the 9-aminoacridine carboxamides introduced in the first manuscript. One possibility for the identity of the compounds in Figures 9b and 9a is species A is diprotonated, species B is monoprotonated, species C is neutral, and species D is anionic. In Figure 9b the deprotonation rate constants are designated k_{BA}, k_{CB}, and k_{DC}. The bimolecular protonation rate constants are designated k_{AB}, k_{BC}, and k_{CD}. The direction of the proton transfer is emphasized in Figure 9a. Each protonation rate constant and its respective deprotonation rate constant are related through their excited state ionization constant. These relations are described by equations (33), (34), and (35).

$$K_{a1}^{*} = \frac{B \times [H^{+}]}{A} = \frac{k_{BA}}{k_{AB}} \tag{33}$$

$$K_{a2}^{*} = \frac{C \times [H^{+}]}{B} = \frac{k_{CB}}{k_{BC}} \tag{34}$$

$$K_{a3}^{*} = \frac{D \times [H^{+}]}{C} = \frac{k_{DC}}{k_{CD}} \tag{35}$$

K_{a1}^*, K_{a2}^*, and K_{a3}^* designate the sequential first, second, and third excited state ionization constant that occurs as the pH of the system is increased. k_A, k_B, k_C, and k_D in Figure 9b are the unimolecular rate constants. The inverse of each respective unimolecular rate constant represents the lifetime of the excited state for the respective species in the absence of proton transfer.

The differential rate equations describing the decay of the four excited state populations of Figure 9b are described by equations (36) through (39).

$$-\frac{dA(t)^*}{dt} = (k_A + k_{BA})A(t)^* - k_{AB}\left[H^+\right]B(t)^* \tag{36}$$

$$-\frac{dB(t)^*}{dt} = -k_{BA}A(t)^* + \left(k_B + k_{AB}\left[H^+\right] + k_{CB}\right)B(t)^* - k_{BC}\left[H^+\right]C(t)^* \tag{37}$$

$$-\frac{dC(t)^*}{dt} = -k_{CB}B(t)^* + \left(k_C + k_{DC} + k_{BC}\left[H^+\right]\right)C(t)^* - k_{CD}\left[H^+\right]D(t)^* \tag{38}$$

$$-\frac{dD(t)^*}{dt} = -k_{DC}C(t)^* + \left(k_D + k_{CD}\left[H^+\right]\right)D(t)^* \tag{39}$$

$A(t)^*$, $B(t)^*$, $C(t)^*$, and $D(t)^*$ are the excited state populations as a function of time. Analogous to the situation of 2-naphthol the solution to the differential equations will be of the form described by equations (40) through (43).

$$I_{A^*}(t) = \alpha_1 \exp\left[-t/\tau_1\right] + \alpha_2 \exp\left[-t/\tau_2\right] + \alpha_3 \exp\left[-t/\tau_3\right] + \alpha_4 \exp\left[-t/\tau_4\right] \quad (40)$$

$$I_{B^*}(t) = \beta_1 \exp\left[-t/\tau_1\right] + \beta_2 \exp\left[-t/\tau_2\right] + \beta_3 \exp\left[-t/\tau_3\right] + \beta_4 \exp\left[-t/\tau_4\right] \quad (41)$$

$$I_{C^*}(t) = \gamma_1 \exp\left[-t/\tau_1\right] + \gamma_2 \exp\left[-t/\tau_2\right] + \gamma_3 \exp\left[-t/\tau_3\right] + \gamma_4 \exp\left[-t/\tau_4\right] \quad (42)$$

$$I_{D^*}(t) = \eta_1 \exp\left[-t/\tau_1\right] + \eta_2 \exp\left[-t/\tau_2\right] + \eta_3 \exp\left[-t/\tau_3\right] + \eta_4 \exp\left[-t/\tau_4\right] \quad (43)$$

$I_{A^*}(t)$, $I_{B^*}(t)$, $I_{C^*}(t)$, and $I_{D^*}(t)$ are the emission intensities due to the excited state species A^*, B^*, C^*, and D^*, respectively. Equations (40) through (43) reveal that each excited state species has an identical set of theoretical lifetimes: τ_1, τ_2, τ_3, and τ_4. Since each lifetimes is associated with an individual excited state amplitude, a total of 16 theoretical amplitudes describe the excited state populations of this system. Both the sixteen amplitudes and the four excited state lifetimes are functions of the rate constants designated in Figure 9b, the ionization constants, and the pH. The excited state amplitudes are additionally functions

of the initial excited state populations. The complexity of extracting the lifetimes and amplitudes from the differential set of equations (36) through (39) is reduced through utilization of the Laplace transform. The Laplace transform will reduce the problem from solving a set of differential equations to solving a set of algebraic equations to obtain the theoretical excited state lifetimes and amplitudes of the system. The calculations for the extraction of the lifetimes will be discussed first followed by the amplitude calculations.

The first step in obtaining the theoretical excited state lifetimes is to take the Laplace transform of the differential equations described by equations (36) through (39). The respective Laplace transformations of equations (36) through (39) are described by equations (44) through (47).

$$-s\cdot a(s)+\left[A^*\right]_0=\left(k_A+k_{BA}\right)a(s)-k_{AB}\left[H^+\right]b(s) \tag{44}$$

$$-s\cdot b(s)+\left[B^*\right]_0=-k_{BA}a(s)+\left(k_B+k_{AB}\left[H^+\right]+k_{CB}\right)b(s)-k_{BC}\left[H^+\right]c(s) \tag{45}$$

$$-s\cdot c(s)+\left[C^*\right]_0=-k_{CB}\cdot b(s)+\left(k_C+k_{DC}+k_{BC}\left[H^+\right]\right)c(s)-k_{CD}\left[H^+\right]d(s) \tag{46}$$

$$-s\cdot d(s)+\left[D^*\right]_0=-k_{DC}\cdot c(s)+\left(k_D+k_{CD}\left[H^+\right]\right)d(s) \tag{47}$$

In equations (44) through (47) $\left[A^*\right]_0$, $\left[B^*\right]_0$, $\left[C^*\right]_0$, and $\left[D^*\right]_0$ are the respective initial excited state populations of species A^*, B^*, C^*, and D^*. a(s), b(s), c(s), and d(s) are the respective Laplace transformations of the excited state populations $A(t)^*$, $B(t)^*$, $C(t)^*$, and $D(t)^*$. Through the incorporation of the Laplace transformation the set of differential equations (36) through (39) have become a set of algebraic equations described by equations (44) through (47). Rewriting equations (44) through (47) by solving for the initial excited state populations results in equations (48) through (51).

$$\left[A^*\right]_0 = \left(k_A + k_{BA} + s\right)a(s) - k_{AB}\left[H^+\right]b(s) \tag{48}$$

$$\left[B^*\right]_0 = -k_{BA}\cdot a(s) + \left(k_B + k_{AB}\left[H^+\right] + k_{CB} + s\right)b(s) - k_{BC}\left[H^+\right]c(s) \tag{49}$$

$$\left[C^*\right]_0 = -k_{CB}\cdot b(s) + \left(k_C + k_{DC} + k_{BC}\left[H^+\right] + s\right)c(s) - k_{CD}\left[H^+\right]d(s) \tag{50}$$

$$\left[D^*\right]_0 = -k_{DC}\cdot c(s) + \left(k_D + k_{CD}\left[H^+\right] + s\right)d(s) \tag{51}$$

The determinant consisting of the coefficients of equations (48) through (51) with the initial excited state populations set to zero is described by equation (52).

(52)

$$0=\begin{vmatrix} k_A+k_{BA}+s & -k_{AB}\left[H^+\right] & 0 & 0 \\ -k_{BA} & k_B+k_{AB}\left[H^+\right]+k_{CB}+s & -k_{BC}\left[H^+\right] & 0 \\ 0 & -k_{CB} & k_C+k_{DC}+k_{BC}\left[H^+\right]+s & -k_{CD}\left[H^+\right] \\ 0 & 0 & -k_{DC} & k_D+k_{CD}\left[H^+\right]+s \end{vmatrix}$$

Equation (52) will result in a fourth order polynomial equation in s. It will be shown later in detail that the negative inverses of the four roots of this polynomial are the four excited state lifetimes mentioned in equations (40) through (43): τ_1, τ_2, τ_3, and τ_4.

The resulting fourth order polynomial from equation (52) has the form

$$f(x)=0=x^n+a_1x^{n-1}+a_2x^{n-2}+a_3x^{n-3}+...+a_{n-1}x+a_n \qquad (53)$$

where $n=4$ and $a_1,a_2,a_3...a_n$ are nonzero coefficients. Equation (53) may be rewritten as equation (54)

$$f(x)=0=(x-\alpha_1)(x-\alpha_2)(x-\alpha_3)...(x-\alpha_n) \qquad (54)$$

where α_1, α_2, α_3,...α_n are the roots of the n^{th} order polynomial $f(x)$ that we are trying to find. There are many different methods to find the roots of this equation. Graeffe's root

squaring technique [7] is one of these methods and will find all the roots of $f(x)$ simultaneously. Graeffe's method is applicable when the n^{th} degree polynomial of equation (53) is set equal to zero and the coefficients are all non zero, (i.e. $a_n \neq 0$). The roots should also follow $|\alpha_1| \geq |\alpha_2| \geq ... |\alpha_n|$ as this property of the roots is essential for Graeffe's method to operate correctly. Consider the function $\phi(x)$ in equation (55).

$$\phi(x) = (-1)^n f(x) f(-x) \tag{55}$$

If the general form of the n^{th} degree polynomial (54) is placed in equation (55) for $f(x)$ then $\phi(x)$ is rewritten as equation (56).

$$\phi(x) = \left(x^2 - \alpha_1^2\right)\left(x^2 - \alpha_2^2\right)...\left(x^2 - \alpha_n^2\right) \tag{56}$$

This may easily be seen for example if $f(x) = (9 + x)$ then $\phi(x) = (9 + x)(9 - x)$ $= \left(81 - x^2\right)$. Since $\phi(x)$ is a polynomial with only even powers a second polynomial $f_2(x)$ may be defined

$$f_2(x) = \phi\left(\sqrt{x}\right) = (x - \alpha_1)(x - \alpha_2)(x - \alpha_3)...(x - \alpha_n) \tag{57}$$

where the roots of $f_2(x) = 0$ are the squares of the roots of the original polynomial (54). If this root squaring procedure is repeated we will then have a sequence of polynomials such as $(f_2, f_4, f_8, f_{16}, f_{32},...)$ where the subscripts indicate the power the roots have been raised to with respect to the roots of the original polynomial equation. Any polynomial in this sequence, $f_m(x)$, may be represented by equation (58)

$$f_m(x) = \left(x - \alpha_1^m\right)\left(x - \alpha_2^m\right)\left(x - \alpha_3^m\right)...\left(x - \alpha_n^m\right) = 0 \tag{58}$$

where m is a power and is a multiple of two. Equation (58) contains the roots $(\alpha_1^m, \alpha_2^m, \alpha_3^m,...\alpha_n^m)$ which are the roots to the original n^{th} degree polynomial in (54) raised to the m^{th} power.

The purpose of the root squaring procedure is to produce a polynomial with roots that differ greatly in magnitude. The roots of such a polynomial may then be approximated by simple functions of its coefficients. For example if the roots of the original n^{th} degree polynomial function $f(x)$ are real and $|\alpha_1| \geq |\alpha_2| \geq ... |\alpha_n|$ then the ratios described in equation (59) may be made as small as desired by making m large.

$$\left|\alpha_2^m / \alpha_1^m\right|, \left|\alpha_3^m / \alpha_2^m\right|, \cdots \left|\alpha_n^m / \alpha_{n-1}^m\right| \tag{59}$$

Expanding equation (58) results in an equation in the form of equation (60)

$$f_m(x) = x^n - \left(\alpha_1^m + \ldots\right)x^{n-1} + \left(\alpha_1^m\alpha_2^m + \ldots\right)x^{n-2} - \left(\alpha_1^m\alpha_2^m\alpha_3^m + \ldots\right)x^{n-3}$$

$$+\ldots+(-1)^n\alpha_1^m\alpha_2^m\alpha_3^m\ldots\alpha_n^m \qquad (60)$$

where the last term is the zeroth order term of the expansion. Equation (60) may be represented as equation (61).

$$f_m(x) = x^n - A_1x^{n-1} + A_2x^{n-2} - A_3x^{n-3} + \ldots + (-1)^n A_n \qquad (61)$$

$A_1, A_2, A_3 \ldots A_n$ are the coefficients of the expansion in (61). From equations (60) and (61) the roots are approximated from the coefficients. The approximations are described in (62).

$$\alpha_1^m \cong A_1, \qquad \alpha_2^m \cong {}^{A_2}\!/_{A_1}, \qquad \alpha_3^m \cong {}^{A_3}\!/_{A_2}, \qquad \alpha_n^m \cong {}^{A_n}\!/_{A_{n-1}} \qquad (62)$$

The backbone of Graeffe's method is that the coefficients for any polynomial $f_m(x)$ in the sequence of root squared polynomials, $(f_2, f_4, f_8, f_{16}, f_{32}\ldots)$, may be calculated from its

preceding polynomial in the sequence through an algorithm. The algorithm is described in equation (63).

$$ {}_{j+1}A_i = (-1)^i \left[{}_jA_i^2 + 2\sum_{\ell=1}^{i} (-1)^{\ell} {}_jA_{i+\ell} \times {}_jA_{i-\ell} \right] \qquad (63) $$

The coefficients, $(A_1, A_2, A_3, \ldots A_n)$, in the root approximations of (62) are found iteratively with this algorithm. The first iteration of the algorithm will determine the coefficients for $f_2(x)$, the next iteration will use the coefficients of $f_2(x)$ to calculate the coefficients for $f_4(x)$. This procedure continues until the coefficients of a polynomial in the sequence $(f_2, f_4, f_8, f_{16}, f_{32} \ldots)$ satisfy the conditions of (62). In the algorithm the iteration is designated by the presubscripts on the coefficients. The postsubscripts designate the coefficient. Therefore the symbol ${}_jA_i$ represents the value of the i^{th} coefficient on the j^{th} pass of the iteration procedure. i must be between $0 \le i \le n$ because there are $(n+1)$ coefficients for an n^{th} degree polynomial. For the initial iteration the initial coefficients used are represented as the set ${}_0A_i$ and equal the coefficients of the original polynomial in equation (53) (i.e. ${}_0A_0 = a_1$, ${}_0A_1 = a_2$, ${}_0A_2 = a_3$, and ${}_0A_3 = a_4$). Upon each iteration the coefficients of a polynomial further in the root squared sequence are found and are used to estimate the roots through the assumptions depicted in (62). The roots are then substituted into the original polynomial equation (53) to determine their validity and sign. If

any of the roots are not solutions to the polynomial equation within a defined region of error then the recently calculated coefficients are returned to the algorithm to calculate new coefficients for the next polynomial in the sequence. After each iteration the roots will differ more greatly in magnitude and the root approximations in (62) will more closely estimate the roots.

Although Graeffe's method gives approximations to all the roots of equation (53) simultaneously it has difficulty in locating complex roots. When the roots are real and distinct then the coefficients (A_1, A_2, A_3,...A_n) are approximately squared at each iteration. However the coefficient A_i is not squared upon each iteration when the roots are not distinct (i.e. $|\alpha_i| = |\alpha_{i+1}|$) or are complex. Another problem with the root squaring technique is that the coefficients developed in the iterations may quickly leave the floating point range of the computer.

Graeffe's root squaring procedure may be more clearly understood if it is followed through in the solution of the fourth order polynomial from the determinant (52). The polynomial has the form of equation (64)

$$f(x) = a_0x^4 + a_1x^3 + a_2x^2 + a_3x + a_4 = (x - r_1)(x - r_2)(x - r_3)(x - r_4) = 0 \quad (64)$$

where a_0, a_1, a_2, a_3, and a_4 are the coefficients found directly from the determinant (52). The coefficients are functions of the hydrogen ion concentration and the designated rate

constants in the kinetic scheme of Figure 9b. The section appendix contains the exact form of a_0, a_1, a_2, a_3, and a_4 obtained from the determinant (52). The first polynomial in Graeffe's sequence of root squared polynomials is found by first performing the operation described in equation (55). The result is equation (65) and is a polynomial of only even powers.

$$\phi(x) = (-1)^n f(x)f(-x) = \left(x^2 - r_1^2\right)\left(x^2 - r_2^2\right)\left(x^2 - r_3^2\right)\left(x^2 - r_4^2\right) \tag{65}$$

The next operation is directed by equation (58) with the result described by equation (66).

$$f_{m=2}(x) = \phi\left(\sqrt{x}\right) = \left(x - r_1^2\right)\left(x - r_2^2\right)\left(x - r_3^2\right)\left(x - r_4^2\right) \tag{66}$$

Equation (66) describes the first polynomial in Graeffe's sequence of root squared polynomials because the roots of (66) are the squares of the roots of the original polynomial (64). In a similar fashion the next polynomial in the sequence is found where the roots of (67) are now to the fourth power of the roots of equation (64).

$$f_{m=4}(x) = \left(x - r_1^4\right)\left(x - r_2^4\right)\left(x - r_3^4\right)\left(x - r_4^4\right) \tag{67}$$

For each polynomial in the sequence the subscript, m, on f represents the power the roots of the original equation have been raised to. The coefficients for any polynomial in the sequence, $f_m(x) = 0$, are found by the algorithm described earlier in equation (63). This algorithm is written more clearly in (68) by omitting the iteration presubscripts.

$$b_i = (-1)^i \left[c_i^2 + 2 \sum_{\ell=1}^{i} (-1)^{\ell} c_{i+\ell} c_{i-\ell} \right] \tag{68}$$

The coefficients, b_i, for any polynomial in the sequence are calculated from the coefficients, c_i, of the preceding polynomial in the sequence. The coefficients, b_i, of the first polynomial, $f_{m=2}(x)$, are found by using the initial coefficients from the determinant (52) for c_i. Thus for the first iteration, initially $c_0 = a_0$, $c_1 = a_1$, $c_2 = a_2$, $c_3 = a_3$, and $c_4 = a_4$. From the algorithm (68) the coefficients for $f_2(x)$ are:

$$i = 0 \qquad b_0 = c_0 = 1.0 \tag{69}$$

$$i = 1 \qquad b_1 = -c_1^2 + 2c_2c_0 \tag{70}$$

$$i = 2 \qquad b_2 = c_2^2 - 2c_3c_1 + 2c_4c_0 \tag{71}$$

$$i=3 \qquad b_3 = -c_3^2 + 2c_4c_2 - 2c_5c_1 + 2c_6c_0$$
$$= -c_3^2 + 2c_4c_2 \tag{72}$$

$$i=4 \qquad b_4 = c_4^2 - 2c_5c_3 + 2c_6c_2 - 2c_7c_1 + 2c_8c_0$$
$$= c_4^2 \tag{73}$$

Equations (72) and (73) are simplified because $c_i = 0$ for $i > n$ and in this case the polynomial being solved is fourth order so $n = 4$. The coefficients b_0, b_1, b_2, b_3, and b_4 are the coefficients of the polynomial $f_2(x)$ and are used to estimate simultaneously all the roots of equation (64) using the approximations given in (62).

$$\alpha_1^2 = b_1/b_0 = b_1 \qquad \alpha_2^2 = b_2/b_1 \qquad \alpha_3^2 = b_3/b_2 \qquad \alpha_4^2 = b_4/b_3 \tag{74}$$

After taking the square root of the approximations in (74), the first estimate of the roots of the fourth order polynomial (64) will have been found. Each approximated root is then substituted into the original equation (64) to check its validity and sign. If all four roots are not satisfactory then the root squaring procedure continues and the algorithm (68) will use the coefficients it found for $f_2(x)$ to determine the coefficients for $f_4(x)$ (i.e. $c_0 = b_0$, $c_1 = b_1$, $c_2 = b_2$, $c_3 = b_3$, and $c_4 = b_4$). The resulting set of coefficients from the second iteration of the algorithm are the coefficients for $f_4(x)$. The coefficients for $f_4(x)$ are then

used to make a second estimate of the roots. However this time m = 4 and the square root must be taken twice to recover the approximated roots described in (62). Each root's validity and sign are then again checked by direct substitution into equation (64). If all four roots have not been found within a defined range of error then a third iteration occurs. The root squaring procedure continues until all four roots are satisfactorily found. Usually less than fifteen iterations are needed before all roots are simultaneously found. In the following paragraphs the roots of determinant (52) will be shown to be the negative inverses of the four excited state lifetimes τ_1, τ_2, τ_3, and τ_4 of the kinetic model described in Figure 9b.

To find relations for the excited state amplitudes equations (44) through (47) must be revisited. In these equations a(s), b(s), c(s), and d(s) are the respective Laplace transformations of the excited state populations of $A(t)^*$, $B(t)^*$, $C(t)^*$, and $D(t)^*$. The transformations a(s), b(s), c(s), and d(s) each have the generic form $f(s)$ described by equation (75)

$$f(s) = \frac{\sum_{n=0}^{3} a_n s^n}{\sum_{n=0}^{4} b_n s^n} = \frac{g(s)}{h(s)} \qquad (75)$$

where g(s) is a third order polynomial and h(s) is a fourth order polynomial. The determinant (52) is represented in equation (75) as h(s). Therefore the coefficients, b_n, of h(s) are the

coefficients of the fourth order polynomial derived from the determinant (52). Since h(s) is not a function of the initial excited state populations then each f(s) will have identical denominators described by h(s). Each fixed set of rate and excited state ionization constants will result in an identical set of roots in the polynomial h(s). Therefore each excited state population will have four identical roots in the denominator of (75). Since g(s) is a third order polynomial and h(s) is a fourth order polynomial, equation (75) may be rewritten as equation (76)

$$f(s) = \frac{a_0 s^3 + a_1 s^2 + a_2 s + a_3}{(s+\alpha_1)(s+\alpha_2)(s+\alpha_3)(s+\alpha_4)} \tag{76}$$

where $-\alpha_1$, $-\alpha_2$, $-\alpha_3$, and $-\alpha_4$ are the roots of the fourth order polynomial h(s). The excited state populations $A(t)^*$, $B(t)^*$, $C(t)^*$, and $D(t)^*$ are recovered by finding the respective inverse Laplace transforms of a(s), b(s), c(s), and d(s). The inverse Laplace transform of a function [6] is indicated on the left hand side of equation (77) where

$$\mathcal{L}^{-1}\{f(s)\} = F(t) \tag{77}$$

F(t) generically represents $A(t)^*$, $B(t)^*$, $C(t)^*$, and $D(t)^*$. In equation (76) f(s) has four singularities at $-\alpha_1$, $-\alpha_2$, $-\alpha_3$, and $-\alpha_4$. The integral in (77) may be found through Cauchy's Residue Theorem [8,9] described in equation (78).

$$F(t) = \sum \left(\text{Res } e^{st} f(s) \right) \tag{78}$$

In equation (78) the generic excited state population F(t) is the sum of the residues of the function $e^{st} f(s)$. Since the singularities $-\alpha_1$, $-\alpha_2$, $-\alpha_3$, and $-\alpha_4$ are all simple poles of f(s), then each residue of f(s) may be written using equation (79)

$$\text{Res}(f; -\alpha_n) = \lim_{s \to -\alpha_n} (s - \alpha_n) f \tag{79}$$

where $f = e^{st} f(s)$ and α_n generically represents the simple poles of f(s). Therefore each excited state population F(t) may be found through substituting the generic form of f(s) in equation (76) into equations (79) and (78). The resulting form of F(t) is found in equation (80)

$$F(t) = \lim_{s \to -\alpha_1} \frac{(s+\alpha_1)\left[a_0 s^3 + a_1 s^2 + a_2 s + a_3\right]}{(s+\alpha_1)(s+\alpha_2)(s+\alpha_3)(s+\alpha_4)} e^{st}$$

$$+ \lim_{s\to-\alpha_2} \frac{(s+\alpha_2)\left[a_0s^3+a_1s^2+a_2s+a_3\right]}{(s+\alpha_1)(s+\alpha_2)(s+\alpha_3)(s+\alpha_4)}e^{st}$$

$$+ \lim_{s\to-\alpha_3} \frac{(s+\alpha_3)\left[a_0s^3+a_1s^2+a_2s+a_3\right]}{(s+\alpha_1)(s+\alpha_2)(s+\alpha_3)(s+\alpha_4)}e^{st}$$

$$+ \lim_{s\to-\alpha_4} \frac{(s+\alpha_4)\left[a_0s^3+a_1s^2+a_2s+a_3\right]}{(s+\alpha_1)(s+\alpha_2)(s+\alpha_3)(s+\alpha_4)}e^{st} \qquad (80)$$

and contains a sum of the residuals of f(s). Equation (81) is obtained by canceling similar factors in the numerator and denominator of equation (80) and by taking the prescribed limits of each term.

$$F(t) = \frac{\left[-a_0\alpha_1{}^3+a_1\alpha_1{}^2-a_2\alpha_1+a_3\right]}{(\alpha_2-\alpha_1)(\alpha_3-\alpha_1)(\alpha_4-\alpha_1)}e^{-\alpha_1t}$$

$$+ \frac{\left[-a_0\alpha_2{}^3+a_1\alpha_2{}^2-a_2\alpha_2+a_3\right]}{(\alpha_1-\alpha_2)(\alpha_3-\alpha_2)(\alpha_4-\alpha_2)}e^{-\alpha_2t}$$

$$+ \frac{\left[-a_0\alpha_3{}^3+a_1\alpha_3{}^2-a_2\alpha_3+a_3\right]}{(\alpha_1-\alpha_3)(\alpha_2-\alpha_3)(\alpha_4-\alpha_3)}e^{-\alpha_3t}$$

$$+ \frac{\left[-a_0\alpha_4^3 + a_1\alpha_4^2 - a_2\alpha_4 + a_3\right]}{(\alpha_1-\alpha_4)(\alpha_2-\alpha_4)(\alpha_3-\alpha_4)} e^{-\alpha_4 t} \qquad (81)$$

In equation (81) it is easily seen that the roots $-\alpha_1$, $-\alpha_2$, $-\alpha_3$, and $-\alpha_4$ of h(s) are the lifetimes of the excited state for the kinetic model described in Figure 9b. Thus each excited state population $A(t)^*$, $B(t)^*$, $C(t)^*$, and $D(t)^*$ is characterized with an identical set of four lifetimes $-1/\alpha_1$, $-1/\alpha_2$, $-1/\alpha_3$, and $-1/\alpha_4$. Equation (81) also reveals that each excited state population, F(t), will have four distinct theoretical amplitudes. Thus an overall total of sixteen distinct theoretical amplitudes will be produced in a four species model.

Each F(t) has its own individual set of coefficients a_n in the numerator of equation (76). Every set of coefficients a_n is found through a different third order polynomial g(s) in equation (75). The different g(s) polynomials for each excited state population are found through creating different determinants from the coefficients of equations (48) through (51). For example to find g(s) for the excited state population of a(s) the determinant described in equation (82) is prepared.

(82)

$$g(s) = \begin{vmatrix} [A^*]_0 & -k_{AB}[H^+] & 0 & 0 \\ [B^*]_0 & k_B + k_{AB}[H^+] + k_{CB} + s & -k_{BC}[H^+] & 0 \\ [C^*]_0 & -k_{CB} & k_C + k_{DC} + k_{BC}[H^+] + s & -k_{CD}[H^+] \\ [D^*]_0 & 0 & -k_{DC} & k_D + k_{CD}[H^+] + s \end{vmatrix}$$

In this determinant the coefficients of a(s) in equations (48) through (51) are replaced with the initial excited state populations. Thus g(s) for each excited state population is always a third order polynomial and is a function of the rate constants, hydrogen ion concentration, and initial excited state populations. After calculating the determinant of equation (82) the excited state population $A(t)^*$ is recovered through equation (81). Similarly to find $B(t)^*$, $C(t)^*$, or $D(t)^*$ their determinant g(s) is found by replacing their respective coefficients of b(s), c(s), or d(s) in equations (48) through (51) with the initial excited state populations. In the end each excited state population $A(t)^*$ through $D(t)^*$ will have four distinct amplitudes that are functions of the rate constants, initial excited state populations, and the hydrogen ion concentration.

Various computer programs have been written to determine the theoretical excited state lifetimes and amplitudes for the kinetic model of Figure 9b. The theoretical lifetimes have been calculated as functions of pH for specified values of rate and ionization constants using a Borland C++ computer program located in the section appendix. The coefficients of the fourth order polynomial, $a_0 = 1$, a_1, a_2, a_3, and a_4, derived from the determinant described in equation (52) were found using Maple V.2 software. The coefficients were placed directly into the Borland C++ lifetime program to avoid error. The lifetime program incorporates Graeffe's root squaring technique to find the roots of the fourth order polynomial. The final results of the Borland lifetime program were independently verified through a program written in Maple V.2 that calculated the lifetimes at a fixed value of pH,

rate, and ionization constants. The determination of the excited state amplitudes requires calculations additional to those used in finding the lifetimes. Four separate Borland computer programs were written to determine the sixteen excited state amplitudes described in equations (40) through (43). The amplitude calculating programs incorporate Graeffe's method to determine the roots of the third order polynomial g(s) to find the sixteen theoretical amplitudes described generically by equation (81). The amplitudes are calculated for chosen values of the initial excited state populations, rate constants, and ionization constants. The initial excited state populations are calculated within the program and depend parametrically on the values assigned to the ground state ionization constants. The amplitude programs also incorporate absorption/detection efficiencies for each species to account for any differences in fluorescence efficiency and wavelength detection dependency. Both the amplitude and lifetime programs along with other required programs are discussed in detail in the section appendix.

Four State Tautomer Equilibrium

Many different kinetic schemes were attempted to fit the picosecond time resolved fluorescence decay data of the 9-aminoacridine carboxamides studied in the first manuscript. The various kinetic models included three, four, and even five excited state species. In the end the kinetic model of Figure 9b resulted in the best agreement with the experimental data of the first manuscript. One of the kinetic models that was initially attempted was the four

species tautomer model described in Figure 11. The tautomer model was initially chosen because of the possibility of tautomerization in the 9-aminoacridine parent compound [10-16]. The tautomer model includes an equilibrium between an excited acid, A*, and its excited conjugate base, B*. The model allows A^* to interconvert with its excited tautomer C^* and B^* to interconvert with its excited tautomer D*. Diagonal rate constants were later incorporated in an attempt to optimize the tautomer model with the data of the first manuscript. The diagonal rate constants proved unnecessary and provided no additional avenues to pursue within the tautomer model.

Computer programs were written to determine the theoretical lifetimes and amplitudes of the tautomer model described in Figure 11. The purpose of Figure 12 is simply to illustrate a few trends of the four excited state lifetimes of the tautomer model with changing pH. The calculations were simplified by assuming the two deprotonation rate constants, k_{BA} and k_{DC}, are equal and the interconversion rate constants are also assumed to be equal: $k_{CA} = k_{AC} = k_{DB} = k_{BD}$. The values used for the unimolecular lifetimes of species A^* and C^* were fixed at 10ns (i.e. $k_A = k_C = 0.1ns^{-1}$) while the unimolecular lifetimes of species B^* and D^* were fixed at 3ns (i.e. $k_B = k_D = 0.33ns^{-1}$). pK_a^{BA} and pK_a^{DC} were fixed at 8.0. The nine illustrations in Figure 12 are organized such that from left to right the proton transfer rate k_{BA} increases and from bottom to top the interconversion rate k_{CA} increases. Thus Figure 12 reveals the behavior of the excited state lifetimes of this system with respect to pH by varying the rate constants k_{BA} and k_{CA}. There are three major trends that can be

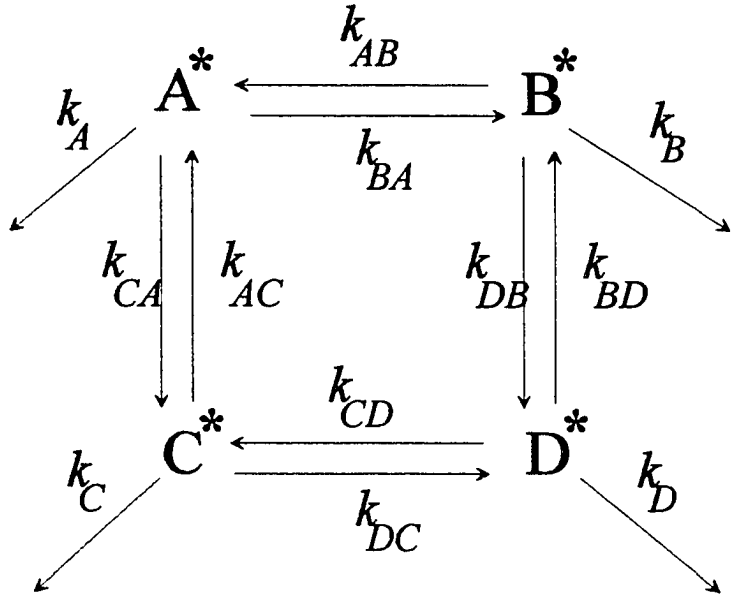

FIGURE 11 Kinetic model for a four species kinetic equilibrium between the acidic tautomers, A^* and C^* and the basic tautomers B^* and D^*. The horizontal rate constants k_{BA}, and k_{DC} designate intermolecular deprotonations, and the horizontal rate constants k_{AB}, and k_{CD} designate bimolecular protonation reactions. The vertical rate constants k_{CA}, k_{AC}, k_{DB}, and k_{BD}, designate intramolecular processes describing the interconversion between tautomers A^* and C^* and the tautomers B^* and D^*, respectively. The rate constants k_A, k_B, k_C, and k_D designate the unimolecular excited state decay. Only the equilibrium occurring in the excited state is shown here.

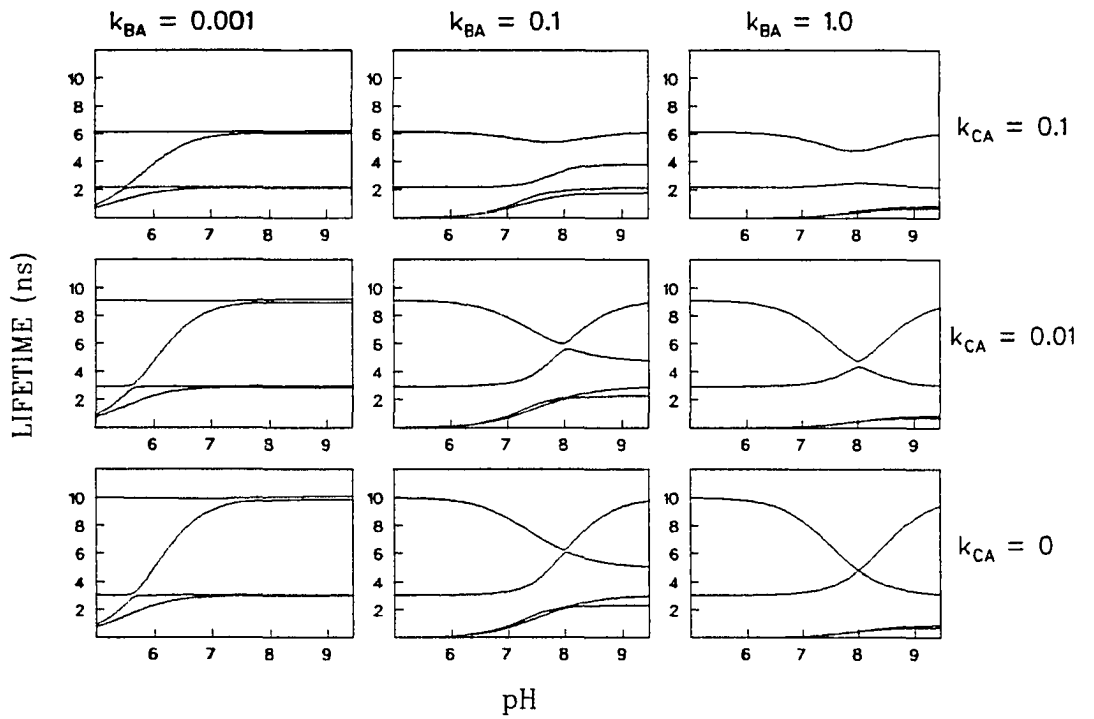

FIGURE 12 Nine theoretical kinetic plots of the theoretical lifetimes verses pH for the four species tautomer model of Figure 11. The calculations were carried out using the technique described earlier for the four species sequential proton transfer system. The unimolecular rate constants are fixed along with the interconversion rate constants (see text for their values) while values of k_{BA} and k_{CA} are varied.

seen in Figure 12. One trend is illustrated in the boxes where k_{BA} is small ($k_{BA} = 0.001$) as in the extreme upper left hand corner of Figure 12 where $k_{BA} = 0.001$ and $k_{CA} = 0.1$. Here, the four excited state lifetimes become independent of pH as the pH is increased. The lifetimes in this case are dependent on pH when pH < 7 because the protonation reaction is significant (i.e. the quantity $k_{AB}[H^+]$ is no longer negligible below pH = 7). Thus in the cases where $k_{BA} = 0.001$ for high pH values only two experimental lifetimes will be observed according to this model. The theoretical lifetimes of the tautomer system are also noticed to get shorter as the interconversion rate k_{CA} is increased. This is expected because as the rate of interconversion is increased an additional route for the decay of the excited state species arises. Another trend may be seen where the proton transfer and interconversion rates are both large in comparison to the unimolecular decay rates k_A and k_B. The extreme of this case is illustrated in the upper right hand corner of Figure 12 where $k_{BA} = 1.0$ and $k_{CA} = 0.1$. Under these conditions the two long lifetime curves illustrate avoided intersections. A final observation is that when $k_{CA} = 0.0$ then the excited state system becomes an uncoupled pair of two-state acid\base proton transfer equilibria. At $k_{CA} = 0.0$ the two long component lifetime curves become intersecting functions of pH that resemble the lifetimes observed in the 2-naphthol system.

References

1. Brand, L.; Laws, W.R., In *Time-Resolved Fluorescence Spectroscopy in Biochemistry and Biology NATO Adv. Sci. Inst. Serv. Series A*, **1983**, vol. 69, 319-340.

2. J. F. Ireland; P. A. H. Wyatt *Adv. Phys. Org. Chem.* **1976**, 12, p.131.

3. Jaffe, H. H.; Jones, H. L. *J. Org. Chem.* **1965**, 30, 964.

4. Atkins, P. W. In *Physical Chemistry* 3rd Edn., Oxford University Press: **1986**.

5. Laws, W. R.; Brand, L. *J. Phys. Chem.* **1979**, 83, 795.

6. Savant, C. J. In *Fundamentals of the Laplace Transformation* McGraw-Hill Book Company, Inc.: New York, NY, **1962**.

7. Carnahan, B.; Luther, H. A.; Wilkes, J. O. *Applied Numerical Methods* John Wiley and Sons: New York, NY, **1969**, p. 141.

8. Arfken, G. In *Mathematical Methods for Physicists* Academic Press: New York, NY, Third Edn., **1985**.

9. Saff, E. B.; Snider, A. D. In *Fundamentals of Complex Analysis* Prentice Hall: Englewood Cliffs, NJ, **1976**.

10. Capomacchia, A.C.; Casper, J.; Schulman, S. G. *Journal of Pharmaceutical Sciences* **1974**, 63(8), 1273.

11. Capomacchia, A.C.; Schulman, S.G. *Journal of Pharmaceutical Sciences* **1974**, 64(7), 1256.

12. Faure, R.; Galy, J.P.; Elguero, V. J.; Galy, A. M.; Barbe, *J. Chemica Scripta* **1979**, 15, 62.

13. Bacon, N.; Boulton, A. J.; Brownlee, R.T.C.; Katritzky, A. R.; Topsom, R. D. *J. Chem. Soc.* **1965**, 5230.

14. Mason, S.F.; *J. Chem. Soc.* **1959**, 1281.

15. Acheson, R. M.; Burstall, M. L.; Jefford, C. W.; Sansom, B. F. *J. Chem. Soc.* **1954**, 3742.

16. Short, L. N. *J. Chem. Soc.* **1952**, 4584.

EXCITED STATE PROTON TRANSFERS IN 9-AMINOACRIDINE CARBOXAMIDES

A paper reprinted with permission from *Journal of Physical Chemistry* 1995, 99, 8927.

Charles A. Smith, Hai-Chou Chang, Walter S. Struve, Graham J. Atwell, William A. Denny

Abstract

Excited state proton transfers have been investigated for several isomeric and homologous N-(dimethylaminoalkyl)-9-aminoacridine carboxamides in a time-correlated single photon counting fluorescence study. The pH behavior of these DNA intercalators' steady-state absorption and fluorescence spectra has also been investigated. While the excited state pK_a^* for removal of a proton from the singly protonated species is close to the ground state pK_a in the parent molecule 9-aminoacridine, the presence of the carboxamide substituent renders pK_a^* much lower than pK_a for the corresponding deprotonation in the present compounds. This fact, along with the presence of an additional deprotonation site at the distal N atom of the side chain, endows these molecules with complex pH dependence in their excited state kinetics. Triexponential model functions are generally required to fit the experimental fluorescence decays. The pH dependence of the component lifetimes and pre-exponential factors can be simulated with a kinetic model for sequential deprotonations involving four aminoacridine species in both the ground and fluorescing states. These results

provide a baseline study for comparisons with these intercalators' excited state kinetics in DNA.

Introduction

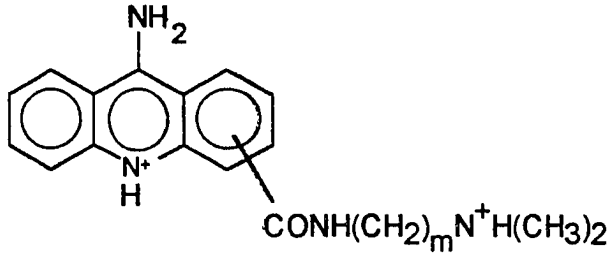

1

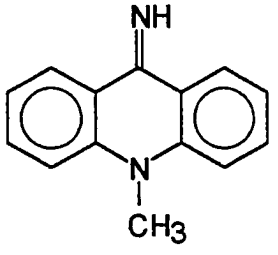

2

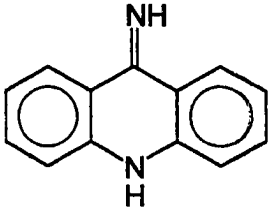

3

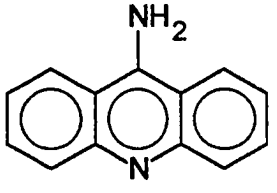

4

The N-(dimethylaminoalkyl)-9-aminoacridine carboxamides (**1**) belong to a large and growing class of molecules that intercalate in DNA. Introduced by Denny and coworkers in 1984 [1], these compounds have many properties in common with intercalators that function as effective antitumor agents. Like amsacrine [2], mitoxantrone [3], and ametantrone [4], they contain a fused tricyclic aromatic chromophore that provides a large area for van der Waals contact with adjacent base pairs. The DNA binding affinity is enhanced by the

chromophore's charge-transfer acceptor capacity, and it is abetted by the electron-withdrawing carboxamide substituent.

Strong DNA-intercalator binding does not ensure antitumor activity *in vivo*. The parent 9-aminoacridine is a well-known intercalator [5], but exhibits low cytotoxicity. Most cytotoxic neutral aromatic intercalators have one [6] or two [7,8] cationic side chains. While the DNA binding affinity of such intercalators is enhanced by appended cationic functional groups, the resulting antitumor activity appears to be more dependent on altered DNA binding kinetics than on binding equilibria. Kinetic studies [9-11] suggest that their biological activity correlates with slow DNA-intercalator dissociation rates and with long intercalator residence times at particular DNA binding sites. Wakelin et al. [12] studied the biological activity and binding kinetics of compounds **1**. (We will hereafter use the nomenclature *m*-*n*C to denote the species **1** in which the carboxamide side chain is substituted in the *m*-position of the aminoacridine chromophore, and contains *n* carbon atoms between its proximal and distal N atoms.) The only known biologically active molecule in this class is 4-2C, in which the side chain contains two spacer carbons and is located in the 4-position of the acridine chromophore. Concomitantly, only 4-2C shows kinetic evidence for the existence of an unusually stable DNA binding mode. A binding model was proposed in which the 4-2C chromophore intercalates DNA from the narrow groove, and forms a bifurcated hydrogen bond between suitably spaced side chain N atoms and an adjacent cytosine oxygen atom. The

geometric requirements of this model appear to be consistent with the observed side chain selectivity in cytotoxicity.

As a preliminary to studying fluorescences of compounds **1** bound to DNA , we have investigated their steady-state and time-resolved fluorescence spectroscopy in solution. Their complicated, pH-dependent excited state kinetics are consistent with the presence of at least two (and probably more) distinct proton transfer equilibria, involving at least three different excited state species. This situation arises in part because the distal N atom of the side chain provides an additional protonation site, so that ground-state compounds **1** are diprotonated at sufficiently low pH (< 8-9). Analysis of the pH dependence in fluorescence lifetimes and pre-exponential factors, together with thermodyamic arguments based on the Förster cycle (see below) indicates that the excited state pK_a* values for dissociation of the first proton from compounds **1** are significantly lower than the corresponding ground state pK_a values. This situation contrasts with that in 9-aminoacridine, whose excited state kinetics show relatively little pH dependence.

Materials and Methods

The principal components in the time-correlated single photon counting apparatus [16] included a Hamamatsu R1564U microchannel plate phototube with a B&H Electronics AC3011 21 dB preamplifier, an EG&G Ortec 457 time-to-amplitude converter, a Tennelec TC455 quad constant-fraction discriminator used for both START and STOP pulses, and an EG&G ACE multichannel analyzer. Samples were excited at ~400 nm with 10 ps fwhm

frequency-doubled pulses from a synchronously pumped styryl 8 dye laser that was cavity-dumped at 3.8 MHz. Samples were housed between λ/4 optical flats separated by a 180 μm Teflon spacer. This assembly was sometimes rotated at 0.015 Hz in order to minimize sample photochemistry during counting periods. The photon counting instrument function varied from 80 to 120 ps fwhm. Rotational diffusion and energy transport effects were eliminated by passing fluorescences through a 54.7° magic-angle polarizer. Sample concentrations were ≤ 0.05 mM, which minimized self-absorption. Count rates were limited to < $5x10^3$ counts/sec. Fluorescence profiles were transferred to an Electra 486DX-33 personal computer, where convolute-and-compare analyses based on a Simplex method were performed in Borland C++. Analysis of fluorescence from N-acetyl tryptophan amide in water (<0.05 mM) showed that its emission was single-exponential (χ^2 < 1.11) with lifetime 2995±40 ps [17].

The synthesis and characterization of the 9-aminoacridine carboxamides **1** have been described previously [1,12]. These were obtained as dihydrochlorides, in which the 9-aminoacridine chromophore and the distal N atom are protonated at neutral pH. 9-Aminoacridine hydrochloride was obtained from Sigma. All absorption spectra were evaluated on a Perkin-Elmer Lambda 3B UV-vis spectrophotometer. Static fluorescence and excitation spectra were obtained on a Spex Fluoromax or Fluorolog 2 spectrofluorimeter with 4.3 nm excitation and detection bandpass. For experiments in non-neutral water solution, the pH was adjusted using increments of concentrated HCl or KOH, and monitored using a Fisher Scientific 915 pH meter.

RESULTS

The UV-visible absorption spectra of compounds **1** in water at neutral pH (Figure 1) are analogous to those of the parent molecule 9-aminoacridine. They are dominated by an intense visible electronic band system (360-450 nm), and a weaker but well-resolved near-UV band system at 300-360 nm. Both band systems are markedly influenced by the position of the carboxamide substituent, as illustrated for 2-2C, 3-2C, and 4-2C in Fig. 1a. Figure 1b shows that the spectra are relatively insensitive to the number of carbon spacers in the carboxamide side chain. The visible band system of **1** in water typically exhibits a 1150-1300 cm^{-1} vibrational progression similar to that observed in 9-aminoacridine. These absorption spectra are essentially independent of concentration between 10^{-4} and 10^{-6} M, and show no evidence for aggregation.

The effects of pH on the absorption spectra of 9-aminoacridine, 4-2C, 4-5C, and 2-2C are shown in Fig. 2. In all of these aminoacridines, the visible band system acquires a long-wavelength shoulder at high pH, indicating the presence of equilibria between protonated and unprotonated species. The near-UV band system is also sensitive to pH. For 9-aminoacridine, the pH-dependent absorption spectra converge at eight sharply defined isosbestic points between 275 and 430 nm. However, the intersections among pH-dependent spectra are more scattered in the other three compounds 4-2C, 4-5C, and 2-2C. This scatter is minor in 4-2C and 2-2C, but is quite noticable between 300 and 350 nm in 4-5C. This indicates that while the proton transfer equilibrium involves only two ground state species in

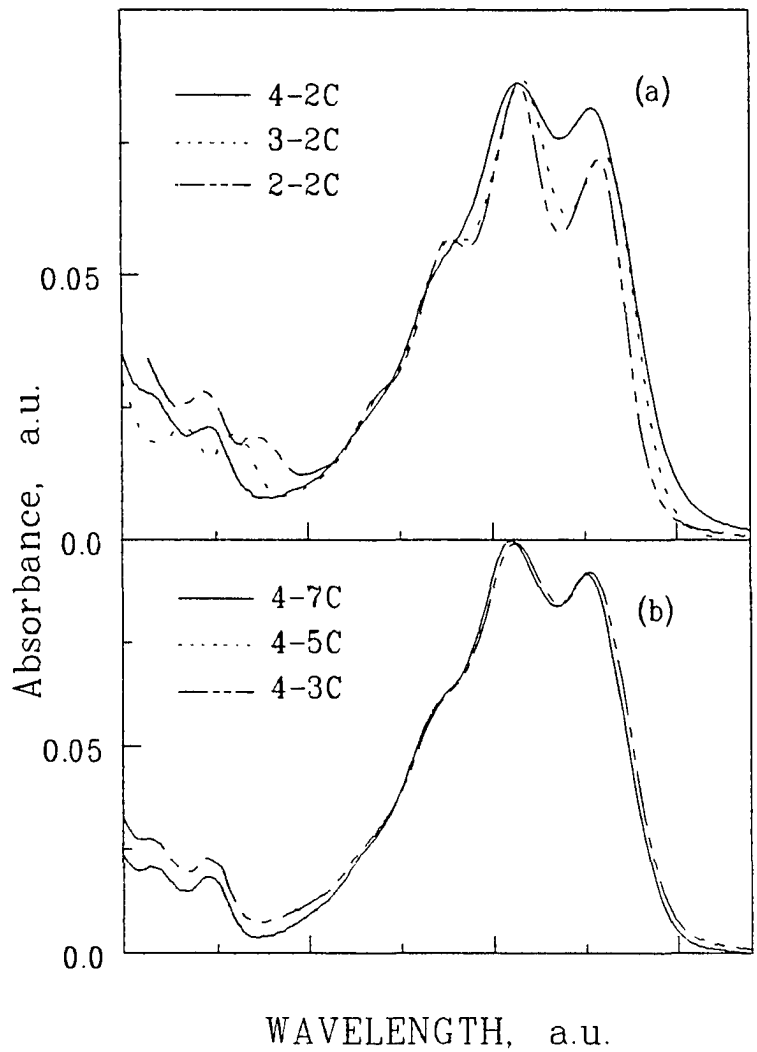

Figure 1. Absorption spectra of *m*-*n*C in water at neutral pH, illustrating the effects of (a) carboxamide substituent position *m* on the aminoacridine chromophore and (b) number *n* of carbon spacers between proximal and distal N atoms in the carboxamide side chain. Spectra are normalized together at the maximum absorption wavelength for comparison.

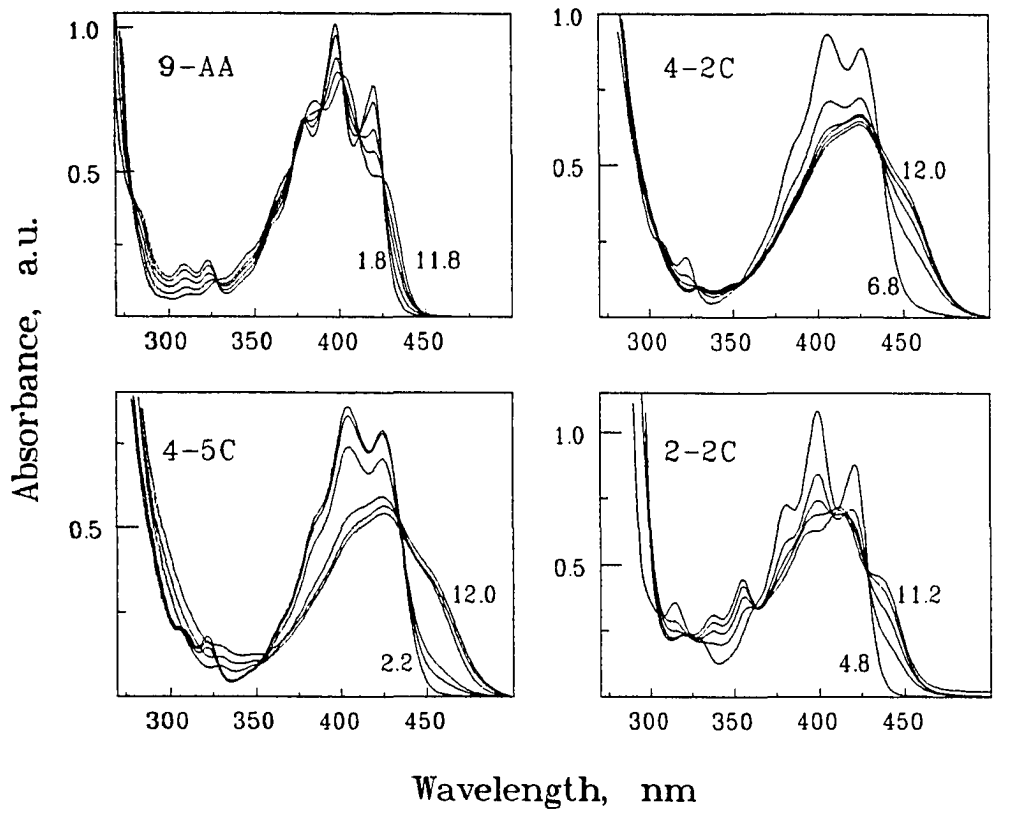

Figure 2. pH dependence of absorption spectra for 9-aminoacridine, 4-2C, 4-5C, and 2-2C in water. Total chromophore concentration is constant in each pH series. Small figures in each panel denote the lowest and highest pH values in each series. Actual pH values are: (for 9-aminoacridine) 1.8, 9.3, 9.8, 10.2, 11.8; (for 4-2C) 6.8, 8.6, 9.4, 10.4, 11.2, 12.0; (for 4-5C) 2.2, 7.7, 8.9, 9.9, 11.6, 12.0; (for 2-2C) 4.8, 8.8, 9.5, 10.1, 11.2.

9-aminoacridine, more than two ground state species contribute to the absorption spectra of the carboxamides. While impurities may account for some of the latter species *a priori*, analyses of the pH dependence in the carboxamide fluorescence kinetics show that this is unlikely (see below). The departures from isosbestic behavior are most pronounced at the highest pH (>10) in Fig. 2. For pH significantly lower than 9, the ground state proton transfer equilibria in compounds **1** appear to be essentially binary.

Figure 3 shows a pH titration of the ratio of absorption coefficients for 4-2C at 450 and 425 nm. The inflection point in this plot occurs at pH 8.0-8.5, which is consistent with pK_a = 8.3 reported for 4-2C in its electronic ground state [18]. This behavior appears to be analogous to a ground-state proton transfer equilibrium that occurs in the visible absorption band system of 9-aminoacridine itself, which exhibits pK_a = 9.9 [19] to 10.0 [20] for the dissociation of a proton from singly protonated aminoacridine. The presence of the electron-withdrawing carboxamide group in 4-2C appears to be responsible for its lower pK_a value. Subsequent ground-state dissociation of a proton from neutral 9-aminoacridine reportedly occurs with pK_a = 15.9, producing an anionic RNH^- species [20].

The pH dependence in the fluorescence excitation spectra of 9-aminoacridine, 4-2C, 4-5C, and 2-2C is shown in Fig. 4. In the case of 9-aminoacridine, this pH evolution closely parallels the pH behavior in the corresponding absorption spectra (Fig. 2). When the monitored emission wavelength is 480 nm, the isosbestic points in the 9-aminoacridine absorption spectra are mirrored by similar isosbestic points in its fluorescence excitation

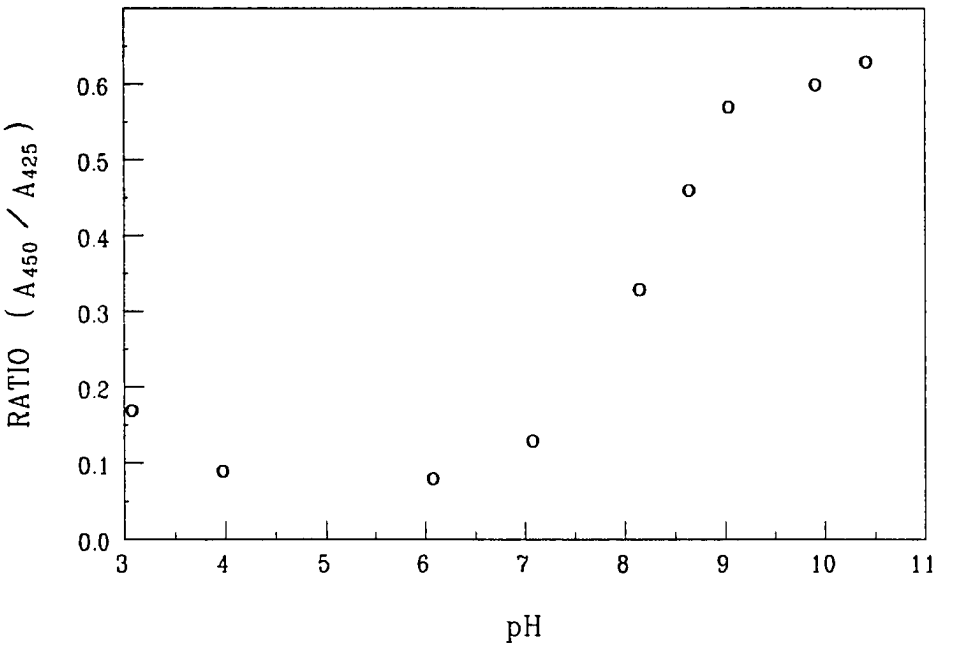

Figure 3. pH titration of the ratio $\varepsilon_{450}/\varepsilon_{425}$ of absorption coefficients for 4-2C in aqueous solution.

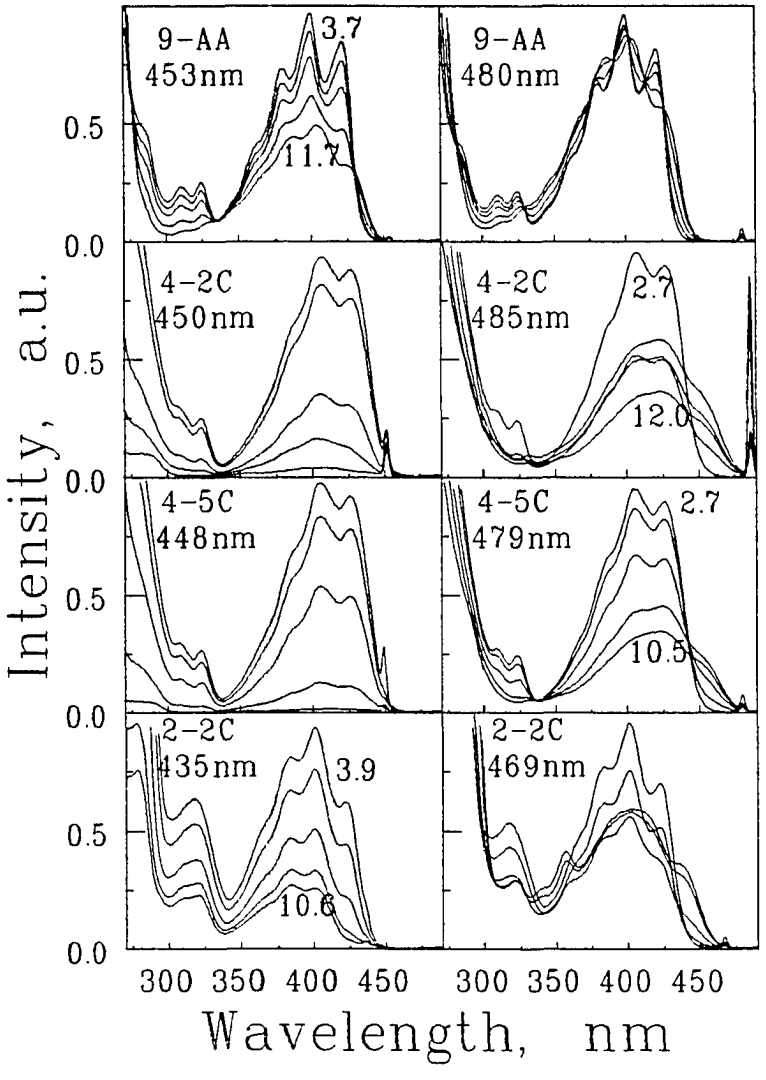

Figure 4. pH dependence in the fluorescence excitation spectra of 9-aminoacridine, 4-2C, 4-5C, and 2-2C in water. Detection wavelengths are given in each panel; excitation and detection bandpass was 2 nm. Total chromophore concentration is constant in each pH series. Small figures in each panel give lowest and highest pH values in each series. Actual pH values are: (for 9-aminoacridine) 3.7, 9.3, 9.8, 10.4, 11.7; (for 4-2C) 2.7, 7.4, 8.6, 9.4, 10.6, 12.0; (for 4-5C) 2.7, 7.9, 8.5, 9.6, 10.5; (for 2-2C) 3.9, 8.0, 8.7, 9.8, 10.6.

spectra. Hence, only two excited state species contribute materially to the fluorescence excitation spectra of 9-aminoacridine. However, the fluorescence excitation spectra of 4-2C, 4-5C, and 2-2C are strongly nonisosbestic, particularly at high pH. For these molecules, the excited state equilibria are not binary proton transfer equilibria.

In all cases, the fluorescence excitation spectrum monitored at any wavelength for a given pH exhibits relative intensities for the visible and near-UV band systems (e.g. at 360-450 nm and 300-360 nm in 4-2C) that are similar to those in the corresponding absorption spectrum. This suggests that for pH considerably higher or lower than pK_a, these two band systems arise largely from different electronic transitions in the same ground state species, rather than from different ground state species (e.g. tautomers). However, similar excitation spectra would arise if the visible and near-UV band systems arose from distinct ground-state species that equilibrated rapidly during the fluorescence lifetime.

pH-dependent fluorescence spectra of 4-2C and 2-2C excited at 400 nm are shown in Fig. 5. The excited state pK_a^* values are not directly obtainable from pH titrations of these steady-state spectra, because fluorescence spectra are governed by excited state proton transfer kinetics as well as by pK_a^* values when the kinetics are not rapid compared to the radiative decay rates.

The pH-dependent fluorescence decays of 9-aminoacridine and carboxamides 2-2C, 3-2C, 4-2C, 4-3C, 4-4C, 4-5C, and 4-7C were extensively studied under 400 nm excitation and broadband detection ($\lambda > 450$ nm), with the results shown in Figs. 6 and 7. In 9-

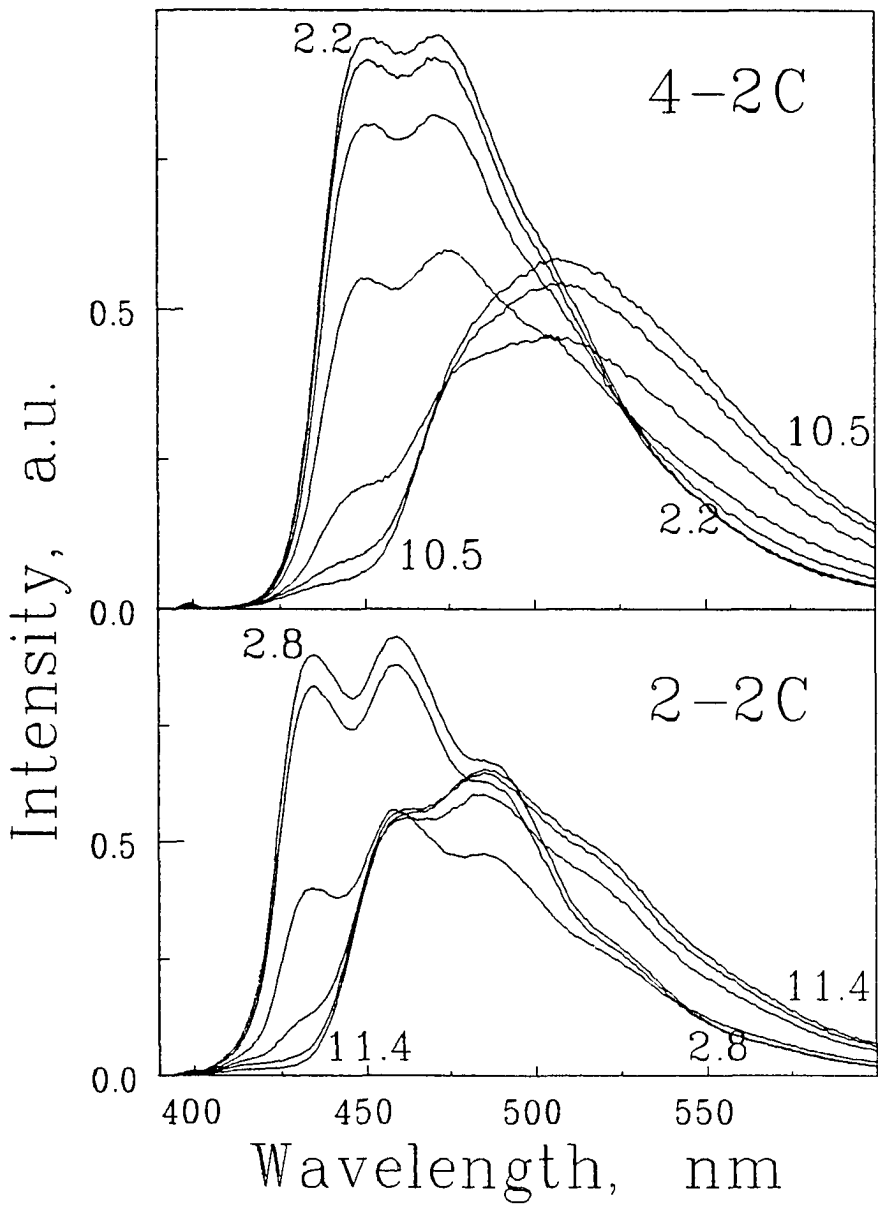

Figure 5. pH dependence of the fluorescence spectra of 4-2C and 2-2C in water. Detection wavelength is 400 nm; excitation and detection bandpass was 2 nm. Total chromophore concentration is constant in both pH series. Small figures in each panel give lowest and highest pH values in each series. Actual pH values are: (for 4-2C) 2.2, 6.3, 7.1, 8.0, 8.8, 9.6, 10.5; (for 2-2C) 2.8, 7.4, 8.6, 9.8, 10.7, 11.4.

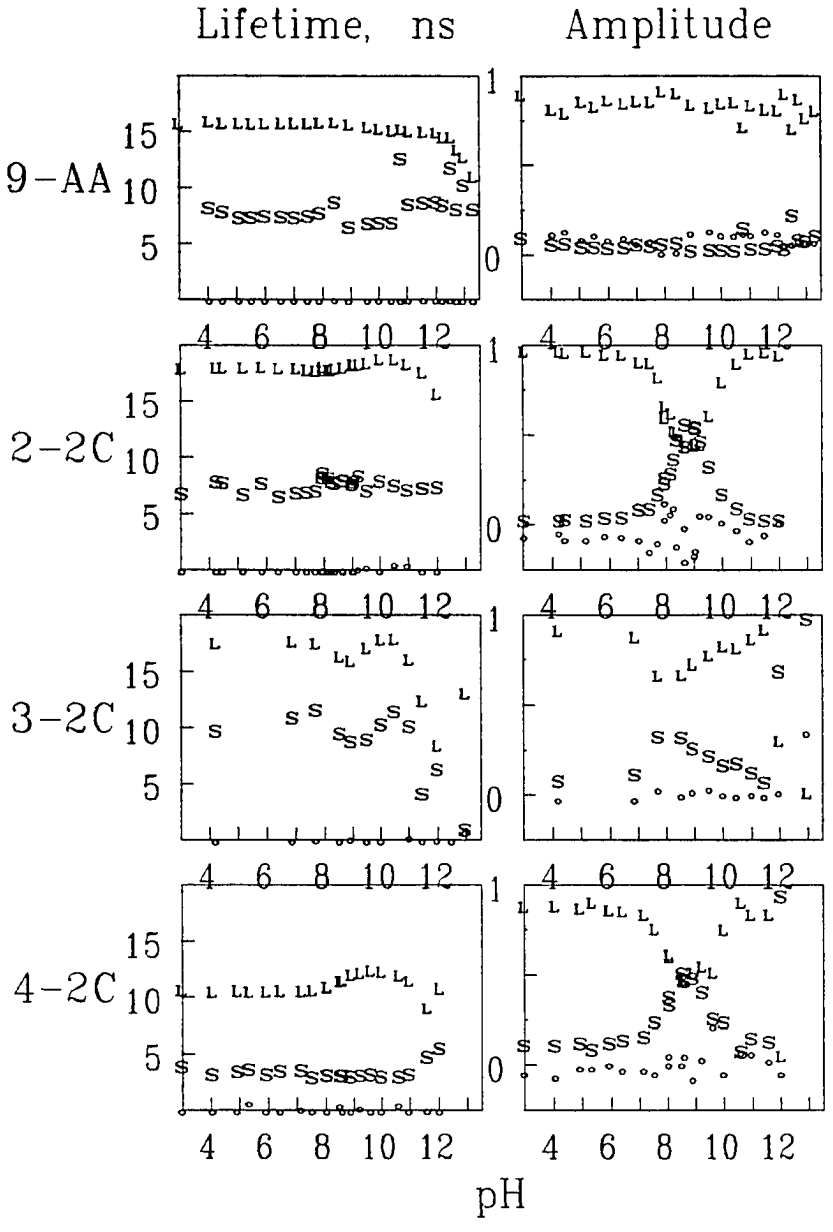

Figure 6. pH dependence of fluorescence component lifetimes and pre-exponential factors for 9-aminoacridine, 2-2C, 3-2C, and 4-2C in water, derived from convolute-and-compare analyses of fluorescence decays using a triexpontential model function. Excitation wavelength was 400 nm. Data points for the long, intermediate, and fast components are denoted with the symbols L, S, and O, respectively.

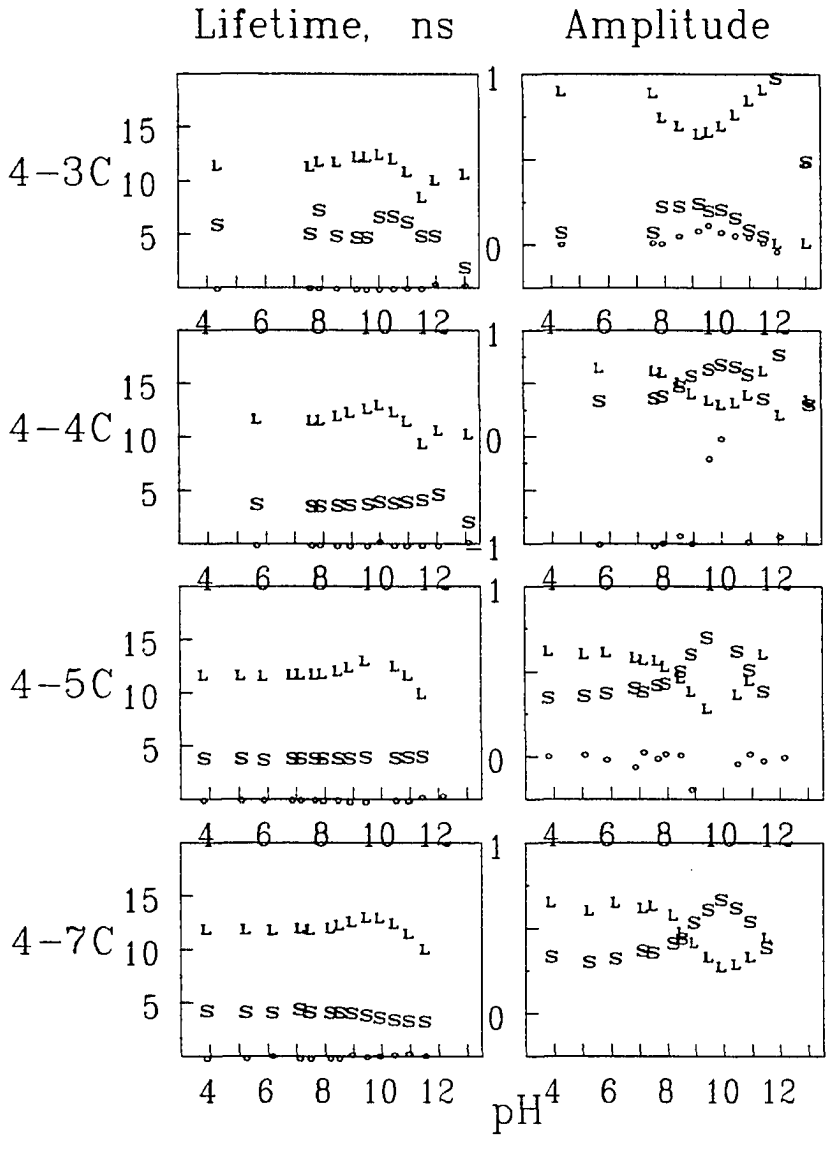

Figure 7. pH dependence of fluorescence component lifetimes and pre-exponential factors for 4-3C, 4-4C, 4-5C, and 4-7C in water. Excitation wavelength was 400 nm. Legend is the same as that in Fig. 6.

aminoacridine, the fluorescence decay is strongly dominated by a 15.9 ns component for pH ≤ 9; minor components (with amplitude ≤ 5%) appear with lifetimes of ~ 6-8 ns and < 1 ns. The long component lifetime decreases slightly to 15.0 ns at pH ~9-10, and then falls off rapidly for pH > 12. However, the amplitudes are essentially insensitive to pH in this parent compound. For the carboxamides, at least three exponential terms are generally required to model the experimental kinetics. In constrast to the case of 9-aminoacridine, the pre-exponential factors vary significantly with pH, and the decays are not always dominated by the long-lifetime component. In compounds 4-2C through 4-7C, the long component lifetime is essentially constant (typically 11-12 ns) as the pH is increased from ~ 4 to ~ 8, and then passes through a local maximum (typically 12-13 ns) at pH 9.5-10, before dropping off at still higher pH. The intermediate component lifetime (typically 3-4.5 ns) changes little for pH between ~ 3 and 10. However, its pre-exponential factor passes through a pronounced maximum, and the long-component pre-exponential factor concomitantly exhibits a local minimum, at pH between 8 and 11. The positions of these extrema in the 4-*n*C series vary somewhat with the number of carbon spacers *n* between the proximal and distal N atoms; they occur at pH ~ 8.5 and ~10 in 4-2C and 4-7C, respectively. The former pH nearly coincides with the pK_a value of 4-2C (cf. ref. 18 and Fig. 3). These pH trends for compounds **1** have no analog in the excited state kinetics of 9-aminoacridine (Fig. 6), in which the pre-exponential factors for the intermediate and short lifetime components are so small that the fluorescence decay is essentially single-exponential for most detection wavelengths [21].

Discussion

The electronic absorption spectrum and chemical reactivity of unprotonated 9-aminoacridine differ fundamentally from those of 1-, 2-, and 4-aminoacridine, whose absorption spectra are very similar to that of their parent molecule acridine [22]. In the latter compounds, the most intense member of the $S_1 \leftarrow S_0$ progression for low pH occurs at ~360 nm. The visible band system of 9-aminoacridine (like those of *m*-*n*C) resembles instead the absorption spectrum of 9-imino-10-methylacridan, **2** [23]. Hence, the visible absorption bands in the 9-aminoacridines may stem from a species with electronic structure analogous to that of 9-iminoacridan (**3**), rather than the 9-aminoacridine structure **4**. This assignment of the lowest-energy (visible) absorption band, proposed long ago by Goodall and Kermack [24], was challenged on the basis of infrared N-H stretching band frequencies in aprotic solvents [25,26]. However, the iminoacridan structure is supported by more recent analyses of electronic band spectra in water [20]. Perhaps for this reason, the S_1 state of 9-aminoacridine lies at considerably lower energy than the S_1 states of acridine and other 9-substituted acridines, such as 9-methyl- and 9-chloroacridine [27]. The visible absorption system in 9-aminoacridine is a strongly allowed, in-plane polarized $\pi \rightarrow \pi^*$ transition [21,27].

9-aminoacridine is singly protonated at neutral pH. X-ray and nuclear magnetic resonance data of related compounds indicate that while unprotonated 1-nitro-9-aminoacridines exist as iminoacridans, they convert to the aminoacridine tautomer when protonated [28,29]. Hence, it appears likely that singly protonated 9-aminoacridine exists as

an aminoacridine rather than an iminoacridan species. The order in which its two N atom sites become deprotonated at higher pH depends on whether the unprotonated species' electronic structure resembles that of 9-iminoacridan (**3**) or 9-aminoacridine (**4**). If structure **3** is correct, the first deprotonation then occurs at the imino group, and the second deprotonation occurs at the heterocyclic N atom. If structure **4** is correct, the first deprotonation site is the pyridine N atom. The second deprotonation then occurs at the amino position, yielding a negatively charged $-NH^-$ species.

The thermodynamic Förster cycle [30-32] has been used to predict excited state pK_a^* values from ground state pK_a values on the basis of steady-state absorption and fluorescence spectra. If the electronic ground and excited states have similar equilibrium geometry in both a protonated species AH^+ and an unprotonated species A, the displacement of pK_a^* from pK_a is approximated by

$$pK_a - pK_a^* = \frac{hc\left(\nu_a^{AH^+} - \nu_a^A + \nu_f^{AH^+} - \nu_f^A\right)}{2(2.303kT)} \qquad (1)$$

where ν_a and ν_f denote the positions in cm^{-1} of the pertinent absorption and fluorescence band maxima. The derivation of Equation 1 presumes that the entropy changes for proton dissociation from AH^+ are similar in the ground and excited states. For 9-aminoacridine, the spectral changes that accompany the first proton dissociation are small (cf. $\left|\nu_a^{AH^+} - \nu_a^A\right| <$

300 cm^{-1} in Fig. 2), with the result that pK_a^* is predicted to be lower than pK_a by at most 0.5 to 0.6 pH units at room temperature. However, the absorption and fluorescence spectra of compounds 4-*n*C ($2 \leq n \leq 7$) and 2-2C exhibit much larger red shifts (Fig. 2) for their first deprotonation. Equation 1 projects that pK_a^* is lower than pK_a by several pH units in the aminoacridine carboxamides. For 4-2C ($pK_a = 8.3$), Equation 1 predicts $pK_a^* = 4.6$, while for 2-2C ($pK_a = 8.6$), it predicts $pK_a^* = 6.7$. These predictions are semiquantitative at best for the aminoacridine carboxamides, since the first deprotonation may be accompanied by significant entropy changes in the side chains. The Förster cycle predictions nevertheless agree qualitatively with our observation (Figs. 6-7) that the fluorescence kinetics are strongly pH-dependent in compounds **1**, but essentially independent of pH in 9-aminoacridine; differentials between pK_a and pK_a^* clearly drive excited state proton transfers. pH titrations of the absorption and fluorescence spectra in 9-aminoacridine [20] show no evidence for the occurrence of excited state proton transfers in the parent molecule.

A third protonation site in the dibasic aminoacridine carboxamides **1** is the distal N atom. (For the proximal N atom in the carboxamide group, pK_a is likely to be in the neighborhood of -1.0, by analogy to acetamide. That site is thus unprotonated under our conditions.) For ordinary aliphatic amines near 300 K, pK_a values are typically 10 to 11 [33]. If protonation of the distal N atom is not strongly influenced by the chromophore π electronic structure, pK_a^* for this site will not differ materially from pK_a. In summary, the available thermodynamic and spectroscopic evidence suggests that in compounds **1**, pK_a for the first

deprotonation is on the order of 8.5 (8.30 for 4-2C, 8.57 for 2-2C [18]), while pK_a^* - as estimated from the Förster cycle - is conservatively several pH units lower than this. Both pK_a and pK_a^* for the distal N atom appear likely to lie near 10-11, if this site does not interact significantly with the chromophore. Finally, Capomacchia et al. [20] reported that pK_a = 15.9 and pK_a^* = 13.2 for the second deprotonation in 9-aminoacridine, yielding an aminoacridine anion RNH^-. The corresponding values of pK_a and pK_a^* for the analogous dissociation of a proton from the dibasic aminoacridine carboxamides **1** are unknown. However, pK_a for this deprotonation must be larger than pK_a ~8.5 for the first deprotonation.

The nonisosbestic behavior in the absorption and fluorescence spectra of compounds **1** (which contrasts with the isosbestic spectra observed in 9-aminoacridine) indicates the presence of more than two ground- and excited-state species in the studied pH range. The fluorescence lifetime and amplitude data in Fig. 6 similarly cannot be understood in terms of a binary excited state equilibrium between protonated and unprotonated aminoacridine species. In a binary equilibrium, the fluorescence decays of both species would be biexponential, and the two species would share common lifetime components [34]. The long component lifetime would change monotonically (from the lifetime of the protonated species to that of the unprotonated species) when the pH passes through pK_a^*. Our experimental decays instead contain at least three components, and the long component lifetime exhibits a local *maximum* at pH 9.5-10 (Fig. 6). We thus consider a sequential deprotonation scheme, involving four

excited state species A, B, C, and D. These represent diprotonated, monoprotonated, neutral (unprotonated), and anionic aminoacridines, respectively (Fig. 8). Deprotonations of species A, B, and C occur with rate constants k_{BA}, k_{CB}, and k_{DC}, respectively. The relevant ground-state pK_a values are denoted pK_{a1}, pK_{a2}, pK_{a3} in increasing order; their excited-state counterparts are pK_{a1}^*, pK_{a2}^*, and pK_{a3}^*. The unimolecular rate constants k_A, k_B, k_C, k_D are the fluorescence decay rates that would occur in the absence of proton transfers. In this

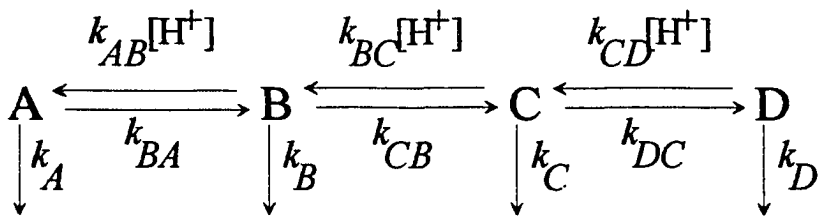

Figure 8. Kinetic scheme for interconversion of four excited-state species A, B, C, D via sequential deprotonation in the aminoacridine carboxamides.

model, each excited state species exhibits four-exponential kinetics, and all four species share the same set of lifetimes. The lifetimes and the (sixteen) amplitudes are not closed-form functions of $[H^+]$ and the rate constants. The pH dependence of the fluorescence lifetimes and amplitudes was therefore simulated in a Borland C++ program (see Appendix). For lifetime simulations, the independent input parameters are the three deprotonation rate

constants, the three excited state equilibrium constants (i.e. pK_{a1}^*, pK_{a2}^*, pK_{a3}^*), and the four unimolecular decay rates. Modeling the pre-exponential factors would require the initial amplitudes $A(0)$, $B(0)$, $C(0)$, and $D(0)$ as well. The latter may be calculated at any pH from the ground state equilibrium constants (pK_{a1}, pK_{a2}, and pK_{a3}), combined with the fluorescence spectra and the absorption coefficients for the four species at the excitation wavelength if they are known.

Typical simulations of the pH dependence in the component lifetimes are superimposed on the experimental lifetime points in Fig. 9 for compound 4-2C, 2-2C, and 4-5C. The pH behavior of the longest-component lifetime is controlled primarily by the excited state pK_a^* values, and by the unimolecular decay rates k_B, k_C, and k_D. This lifetime evolves from k_B^{-1} into k_C^{-1}, and subsequently from k_C^{-1} into k_D^{-1}, as the pH passes through pK_{a2}^* and then through pK_{a3}^*. In this model, the local maxima in this component's lifetime (Figs. 6,7) arise because k_C (the unimolecular decay rate for the unprotonated aminoacridine) is smaller than either k_B or k_D. The positions and widths of these maxima depend on pK_{a2}^* and pK_{a3}^*. The model requires that $pK_{a1}^* < 4$ (for the first excited-state deprotonation), because the empirical intermediate component lifetime (see below) would otherwise vary significantly with pH for $5 < \text{pH} < 7$. The optimal ranges of pK_{a2}^* and pK_{a3}^* are 8-9 and 12-13, respectively, depending on the aminoacridine species (Table I). There is not much leeway or covariance in the parameters governing fits to the long-component lifetimes.

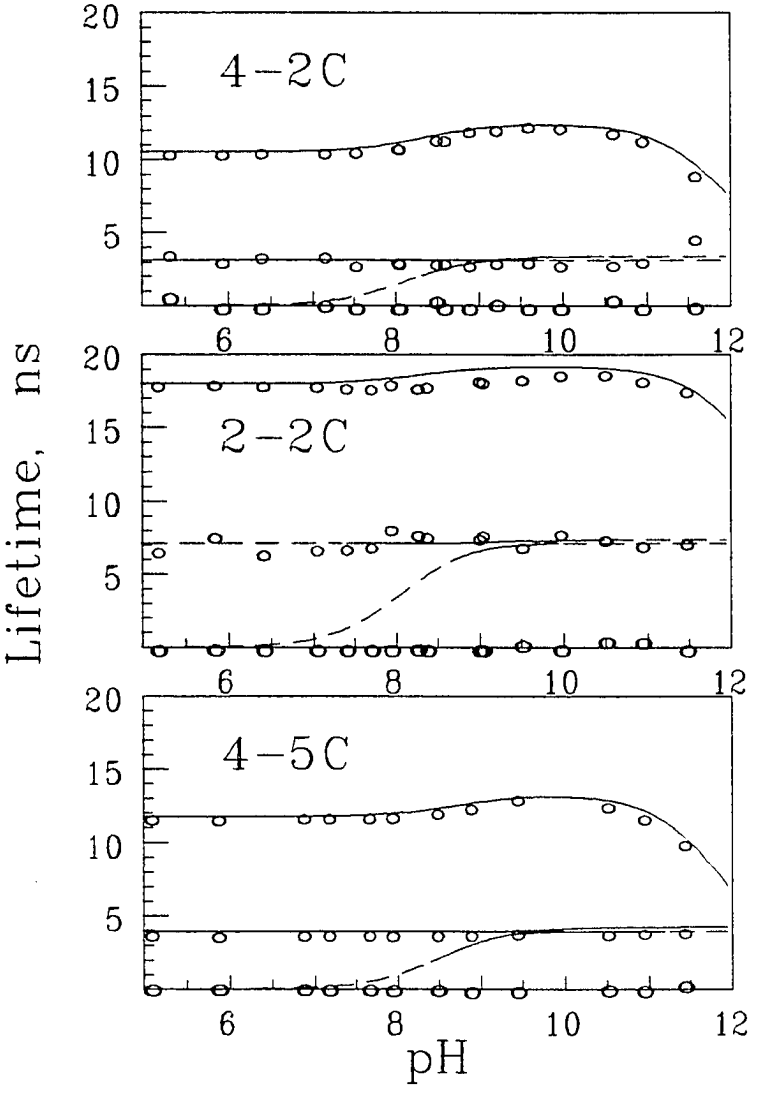

Figure 9. Simulation of pH-dependent lifetimes using the sequential deprotonation kinetic model (Fig. 8) for compounds 4-2C, 2-2C, and 4-5C. Dashed portions of the curves indicate regions where the projected lifetime components exhibit small amplitudes (< 0.1). Data points indicate experimental lifetimes; optimized parameters for these simulations are listed in Table I.

In the fits for compound 4-2C in Fig. 9, two theoretical components appear with lifetimes between 1.5 and 3.5 ns for pH > 8. At most pH, one or the other of these intermediate components exhibits very small amplitude. For these components, the simulated lifetimes in Fig. 9 are plotted as dashed rather than solid curves in the pH ranges where their amplitudes become less than 0.1. For pH < 8, for example, an intermediate component appears in the simulations with a pH-independent lifetime of essentially $(k_A + k_{BA})^{-1} = 3.1$ ns, the reciprocal sum of the diprotonated species' unimolecular decay and deprotonation rates. This component is readily observed, because the predominant ground and excited state species for these pH are A and B, respectively. In the same pH range, a markedly pH-dependent lifetime appears, which corresponds to proton transfers involving species C and/or D (dashed curve in Fig. 9). The latter component is undetectable at these pH, because species C and D are not prevalent as equilibrium species. The rate constants k_A and k_{BA} are covariant in these fits to the intermediate lifetime for pH < 8, and this simulation does not yield unique values for k_A or k_{BA}. The simulated fast (subnanosecond) component lifetime becomes discernible on the scale of Fig. 9 only when the pH becomes higher than pK_{a3}. This lifetime is controlled by the deprotonation rate k_{DC}. While there is considerable scatter in the experimental fast component lifetimes yielded by our triexponential fits, our data for several of the compounds (e.g. 4-3C, 4-5C, and 4-7C) do suggest the presence of a subnanosecond lifetime that increases noticably (as predicted by the model) for pH greater than 10-12.

The pre-exponential factors (Figs. 6-7) are strongly influenced by the initial amplitudes $A(0)$, $B(0)$, $C(0)$, and $D(0)$. These in turn depend on the ground state equilibrium constants pK_{a1}, pK_{a2}, pK_{a3}, and on the relative absorption coefficients of the aminoacridine species at the excitation wavelength (400 nm). They also depend on the fluorescence detection efficiencies for the four species. Since the individual fluorescence spectra overlap extensively and are not separately resolved, the initial amplitudes were modeled by multiplying the fractional ground state equilibrium populations (computed at every pH for assumed pKa_1, pKa_2, and pKa_3) by adjustable parameters that represented combined efficiencies for absorption and fluorescence detection. The rate constants and the excited state equilibrium constants pKa_1^*, pKa_2^*, and pKa_3^* were fixed at their optimized values from the lifetime fits (Table I). The ground state pK_a values were then varied, along with the relative absorption/detection efficiencies, to simulate the total fluorescence profiles as weighted sums of four-exponential decay laws for the individual species. The optimized fits to the 4-2C experimental pre-exponential factors are shown in Fig. 10 for the three components with lifetimes $\geq$ 1 ns. The 10-12 ns component (which is primarily associated with unimolecular decay via k_B, k_C, or k_D) shows a positive decay amplitude at all pH. This simulated amplitude, like the experimental long component amplitudes, lies between 0.7 and 1.0 at most pH, but exhibits a minimum near pH 9. The 3.1 ns component (which corresponds to $(k_A+k_{BA})^{-1}$) exhibits a (positive) decay amplitude for pH < 9.25, and a (negative) rise amplitude for pH > 9.25. The third component (which exhibits lifetimes of 2-

Table I. Rate constants and excited state equilibrium constants from simulations of fluorescence lifetimes using sequential deprotonation model in Figure 8. [a]

	2-2C	4-2C	4-5C
pK_{a1}*	2	2	2
pK_{a2}*	8.3	8.3	8.7
pK_{a3}*	13.0	13.0	13.0
$k_A + k_{BA}$	*0.14*	*0.32*	*0.26*
k_B	0.055	0.095	0.085
k_C	0.052	0.080	0.075
k_D	0.20	0.75	0.90
k_{CB}	0.08	0.20	0.15
k_{DC}	0.50	0.50	0.50

[a] The parameters k_A and k_{BA} (numerical values in italics) are covariant, and model fits only yield values for $k_A + k_{BA}$. All rate constants are in ns^{-1}.

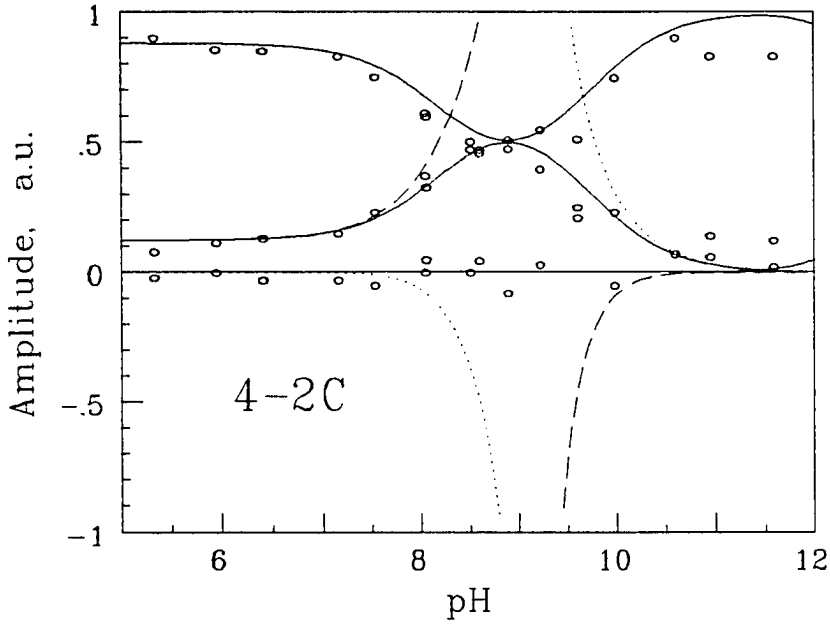

Figure 10. Simulation of pre-exponential factors for 4-2C using the kinetic model of Fig. 8. For the intermediate-lifetime components, the dashed curves give the 3.1 ns component amplitude, the dotted curves give the 1.5-3.5 ns component amplitude, and the lower solid curve gives their sum. The upper solid curve gives the long-component amplitude. Data points indicate experimental pre-exponential factors.

3.5 ns at pH for which this component is observable) conversely shows rise and decay amplitudes for pH > 9.25 and < 9.25, respectively. Components with lifetimes as closely spaced as 3.1 and 2-3.5 ns are experimentally unresolvable, and would become merged into a single component in our convolute-and-compare analyses. Hence, Figure 10 also displays the sum of the latter two amplitudes as a solid curve. This sum is positive at all pH, and it closely resembles the amplitude of the experimental intermediate component at most pH. Optimized pK_a values from simulation of the fluorescence pre-exponential factors for 2-2C, 4-2C, and 4-5C are listed in Table II.

Figure 10 belies the complexity of the modeled excited state kinetics. For example, the fractional ground and excited state equilibrium populations are shown for 4-2C as functions of pH in Fig. 11. In this Figure, the pK_a and pK_a^* values (Table II) are derived from optimized fits to the experimental lifetimes and pre-exponential factors, respectively. At pH 8.5, the simulated 4-2C excited state populations are (with lifetimes in nanoseconds):

$$A(t) = 0.63\exp(-t/3.1)$$

$$B(t) = 0.48\exp(-t/3.1) - 0.45\exp(-t/2.4) + 0.28\exp(-t/11.6)$$

$$C(t) = -0.84\exp(-t/3.1) + 0.43\exp(-t/2.4) + 0.47\exp(-t/11.6)$$

For simplicity, these expressions omit a fourth, subnanosecond component that occurs with small amplitude. At this pH, the predominant ground-state species are A (63%) and B (31%),

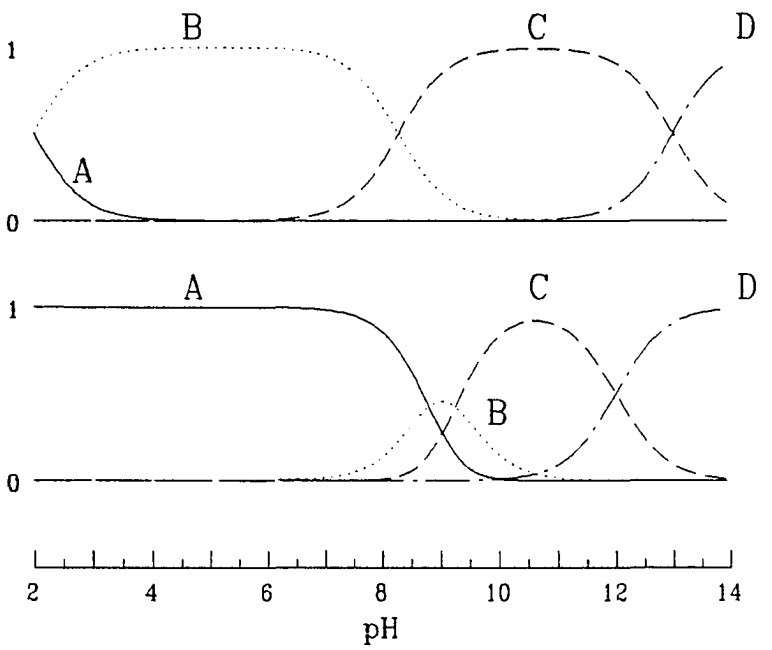

Figure 11. Fractional ground and excited state equilibrium populations for 4-2C, computed using $pK_{a1} = 8.8$, $pK_{a2} = 9.25$, $pK_{a3} = 12$, and $pK_{a1}^* = 2$, $pK_{a2}^* = 8.3$, $pK_{a3}^* = 13$ (Tables I and II).

Table II. Ground state equilibrium constants from simulations of pre-exponential factors using the sequential deprotonation model in Figure 8.

Compound	pK_{a1}	pK_{a2}	pK_{a3}
4-2C	8.8	9.25	12
	8.3 [a]	9.35	11
2-2C	9.25	9.5	13
	8.57 [a]	9.0	12
4-5C	9.5	10.75	13.5

[a] pK_{a1} fixed at spectroscopic value (Ref. 18)

whereas the major excited state species are B (39%) and C (61%). While excited species A exhibits single-exponential decay with 3.1 ns kinetics, the excited species B and C show both rise and decay behavior. The sum of these three populations, weighted by the set of absorption/detection efficiencies that yields the optimal fit to the experimental pre-exponential factors in Fig. 6, is

$$F(t) = 1.94\exp(-t/3.1) - 0.88\exp(-t/2.4) + 1.29\exp(-t/11.6)$$

In a least-squares analysis of such a fluorescence decay, the first two components would appear as a single decay component with a lifetime near 3 ns, and the substantial 2.4 ns rise component would be masked. This example illustrates the extent to which the empirical pre-exponential factors in Figs. 6 and 7 are composite properties of the excited state kinetics.

The pre-exponential factors are sensitive to the absorption and fluorescence spectra. The small differences in these properties among compounds *m*-*n*C (cf. Figs. 1 and 5) readily account for the species variations in the distribution of amplitudes between the long- and intermediate-lifetime components (Figs. 6 and 7). The positions of the extrema in these two amplitudes are influenced by the ground state pK_a values. Larger values of pK_{a2} shift these extrema to higher pH; simulation of the experimental amplitudes for 4-5C (Fig. 12) requires a higher value of pKa_2 than for 4-2C (10-11, versus 9.25).

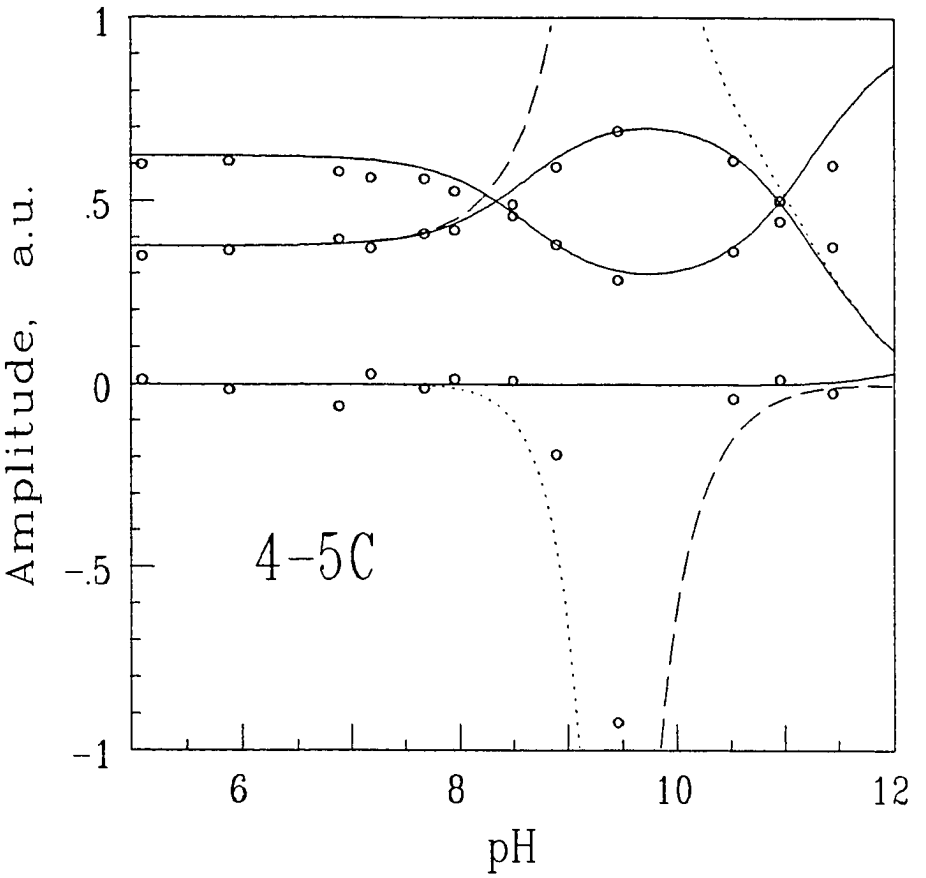

Figure 12. Simulation of pre-exponential factors for 4-5C using the kinetic model of Fig. 8. The legend is analogous to that of Fig. 10.

Simulations were also attempted using kinetic schemes other than the one in Fig. 8. These included a sequential deprotonation scheme involving only three species, and a four-species scheme in which two interconvertible tautomeric species (e.g. aminoacridine ↔ iminoacridine) undergo independent intermolecular proton transfers. The first of these schemes was insufficiently flexible to simulate the experimental lifetimes, while the second one could not produce realistic pH behavior in the pre-exponential factors.

In our simulations, pK_{a1}* is significantly lower than pK_{a1} for the first deprotonation in the aminoacridine carboxamides **1**. This situation reverses the trend in most aromatic heterocycles, which tend to gain rather than lose a proton in their excited states. For acridine, pK_a and pK_a* are 5.5 and 10.7, respectively [35]. However, pK_a and pK_a* nearly coincide in 9-aminoacridine, while the presence of the electron-withdrawing carboxamide group in compounds *m-n*C evidently causes their excited states to deprotonate. Förster cycle calculations suggest that pK_{a1}* for compound 4-2C is on the order of 4-5. Analysis of our kinetic data for 4-2C suggests that pK_{a1}* may be somewhat lower than this, because its intermediate component lifetime is essentially independent of pH in acidic solution. While pK_{a1}* has been set at 2 in our simulations, essentially identical lifetimes and pre-exponential factors can be simulated with pK_{a1}* as high as 3.5 without changing any of the other parameters. The pK_{a1} values that optimize our fits to the pre-exponential factors for 4-2C and 2-2C (8.8 and 9.25, respectively) are slightly higher than the ones (8.3 and 8.57) obtained from titrations of their absorption spectra [18]. When this parameter is frozen at the

spectroscopic value for 4-2C or 2-2C, readjusting pK_{a2} and pK_{a3} (Table I) yields a slightly poorer (but still acceptable) fit to the pre-exponential factors.

The first deprotonation occurs at either the amino group or the pyridine N atom, depending on whether neutral 9-aminoacridine more closely resembles structure **3** or **4**. The chemical and spectroscopic evidence [22-26] suggests that the iminoacridan structure **3** may be more correct. Owing to the clustering of several pK_a and pK_a^* values near 8-11 (Fig. 11), the order in which the subsequent two deprotonations occur (at the distal N atom, and at the amino group or at the heterocyclic N atom) is unclear. However, our simulations suggest that second and third deprotonations occur in the same order in the ground and excited states, because the simulations otherwise yield excited state kinetics very different from those observed in Figs. 6 and 7.

We finally comment on the subnanosecond component that is observed in **1** for nearly all pH. For pH < pK_{a3}, our simulations predict the occurrence of picosecond proton transfers. Due to scatter arising from limited time resolution and the small amplitudes of these components, the value of k_{DC} (which controls the kinetics of the rapid proton transfers at high pH) is not well defined by our measurements. Variations in k_{DC} from 0.5 to 5 ns^{-1} have little effect on the lifetimes on the scale of Figs. 6 and 7. Dynamic excited state solvation is ubiquitous in the fluorescence spectroscopy of molecules in polar solvents, and this process is likely to contribute to the empirical subnanosecond components as well.

Acknowledgements

We thank Ms. JeNell Pederson for her help with the time-correlated photon counting studies in this project.

Appendix

We consider the kinetic scheme for four excited state species in Fig. 8, in which the excited state proton transfer kinetics are controlled by the deprotonation rate constants k_{BA}, k_{CB}, k_{DC} along with the equilibrium constants pK_{a1}^*, pK_{a2}^*, pK_{a3}^*. The protonation rate constants k_{AB}, k_{BC}, k_{CD} are related to these via

$$\frac{k_{BA}}{k_{AB}} = K_{a1}^* = \frac{[B][H^+]}{[A]}$$

$$\frac{k_{CB}}{k_{BC}} = K_{a2}^* = \frac{[C][H^+]}{[B]} \qquad \text{(A1)}$$

$$\frac{k_{DC}}{k_{CD}} = K_{a3}^* = \frac{[D][H^+]}{[C]}$$

so that excited state species A predominates over excited state species B at equilibrium when the pH is lower than pK_{a1}^*, etc. The four rate constants k_A, k_B, k_C, and k_D are the "unimolecular" excited state decay rates. The Laplace transforms *a(s)*, *b(s)*, *c(s)*, and *d(s)* of the four excited state populations *A(t)*, *B(t)*, *C(t)*, and *D(t)* have the generic form

$$f(s) = \frac{\sum_{n=0}^{3} a_n s^n}{\sum_{n=0}^{4} b_n s^n} \equiv \frac{g(s)}{h(s)} \tag{A2}$$

where the coefficients a_n and b_n are functions of the rate constants and the initial excited state populations $A(0)$, $B(0)$, $C(0)$, and $D(0)$. These coefficients (generated by expanding 4x4 determinants that arise in solving the simultaneous linear equations for the Laplace transforms) were evaluated symbolically using Maple V.2 software, and translated directly into Borland C++ code to circumvent human error. The real-valued roots $-k_1$, $-k_2$, $-k_3$, $-k_4$ of the fourth-order polynomial *h(s)* were obtained using the Graeffe root-squaring algorithm [36]; these roots are by definition simple poles in the Laplace transform

$$f(s) = \frac{g(s)}{(s+k_1)(s+k_2)(s+k_3)(s+k_4)} \tag{A3}$$

The inverse Laplace tranform *F(t)* of *f(s)* is then given by the sum of residues in the function $e^{st} f(s)$ at these poles [37], i.e.

$$F(t) = \frac{g(-k_1)}{(k_2-k_1)(k_3-k_1)(k_4-k_1)} e^{-k_1 t} + \frac{g(-k_2)}{(k_1-k_2)(k_3-k_2)(k_4-k_2)} e^{-k_2 t}$$
$$+ \frac{g(-k_3)}{(k_1-k_3)(k_2-k_3)(k_4-k_3)} e^{-k_3 t} + \frac{g(-k_4)}{(k_1-k_4)(k_2-k_4)(k_3-k_4)} e^{-k_4 t} \tag{A4}$$

Hence, the excited state populations *A(t)* through *D(t)* in this model are four-exponential functions of time, and (since the coefficients b_n in the polynomial *h(s)* arise from the simultaneous equations' determinant of coefficients) all four populations share the same set of lifetimes. However, the coefficients a_n in the polynomial *g(s)* are different for each of the Laplace transforms *a(s)* through *d(s)*, so that the four excited state species collectively exhibit sixteen distinct amplitudes according to Eqs. A4.

References

1. Atwell, G. J.; Cain, B. F.; Baguley, B. C.; Finlay, G. J.; Denny, W. A. *J. Med. Chem.* **1984**, *27*, 1481.

2. Cain, B. F.; Atwell, G. J. *Eur. J. Cancer* **1974**, *10*, 539.

3. Griffen, J. P.; Newman, R. A.; McCormack, J. J.; Krakoff, I. H. *Cancer Treat. Rep.* **1982**, *66*, 1323.

4. Piccart, M. *Eur. J. Cancer* **1981**, *17*, 775.

5. Lerman, L. S. *J. Mol. Biol.* **1961**, *3*, 18.

6. Zee-Cheng, R. K.-Y.; Podrebarac, E. G.; Menon, C. S.; Cheng. C. C. *J. Med. Chem.* **1979**, *22*, 501.

7. Zee-Cheng, R. K.-Y.; Cheng, C. C. *J. Med. Chem.* **1978**, *21*, 291.

8. Murdock, K. C.; Child, R. G.; Fabio. P. F.; Angier, R. B.; Wallace, R. E.; Durr, F. E.; Citarella, R. V. *J. Med. Chem.* **1979**, 22, 1024.

9. Muller, W.; Crothers, D. M. *J. Mol. Biol.* **1968**, *35*, 251.

10. Feigon, J.; Denny. W. A.; Leupin, W.; Kearns, D. R. *J. Med. Chem.* **1984**, *27*, 450.

11. Denny, W. A.; Atwell, G. J.; Baguley, B. C.; Wakelin, L. P. G. *J. Med. Chem.* **1985**, *28*, 1568.

12. Wakelin, L. P. G.; Atwell, G. J.; Rewcastle, G. W.; Denny, W. A. *J. Med. Chem.* **1987**, *30*, 855.

13. Deamer, D. W.; Prince, R. C.; Crofts, A. R. *Biochim. Biophys. Acta* **1972**, *274*, 323.

14. Casadio, R.; Baccarini-Melandri, A.; Zannoni, C.; Melandri, B. A. *FEBS Letts.* **1974**, *49*, 203.

15. Walker, E. B.; Yoon, M.; Song, P-S. *Biochim. Biophys. Acta* **1981**, *634*, 289.

16. Lin, S.; Struve, W. S. *J. Phys. Chem.* **1991**, *95*, 2251.

17. Petrich, J. W.; Chang, M. C.; McDonald, D. B.; Fleming, G. R. *J. Amer. Chem. Soc.* **1983**, *105*, 3824.

18. Atwell, G. J.; Rewcastle, G. W.; Baguley, B. C.; Denny, W. A. *J. Med. Chem.* **1987**, *30*, 664.

19. Orgel, L. E. In *The Chemistry of Heterocyclic Compounds: Acridines*, Ed. R. M. Acheson (Wiley-Interscience, New York, 1956)

20. Capomacchia, A. C.; Casper, J.; Schulman, S. G. *J. Pharm Sci.* **1974**, *63*, 127.

21. Barkley, M. D.; Kowalczyk, A. A.; Brand, L. *J. Chem. Phys.* **1981**, *75*, 3581.

22. L. E. Orgel, in *The Chemistry of Heterocyclic Compounds: Acridine*, ed. R. M. Acheson, (Wiley-Interscience, New York, NY, 1956), Ch. VII.

23. Albert, W.; Ritchie, J. *J. Chem. Soc.* **1943**, *1943*, 458.

24. Goodall, W.; Kermack, J. *J. Chem. Soc.* **1936**, *1936*, 1546.

25. Mason, S. F. *J. Chem. Soc.* **1959**, *1959*, 1281.

26. Bacon, N.; Boulton, A. J.; Brownslee, R. T. C.; Katritzky, A. R.; Topsom. R. D. *J. Chem. Soc.* **1965**, *1965*, 5230.

27. Kasama, K.; Kikuchi, K.; Nishida, Y.; Kokubun, H. *J. Phys. Chem.* **1981**, *85*, 4148.

28. Stezowski, J. J.; Kollat, P.; Bogucka-Ledóchowska, M.; Glusker, J. P. *J. Am. Chem. Soc.* **1985**, *107*, 2067.

29. Boyd, M.; Denny, W. A. *J. Med. Chem.* **1990**, *33*, 2656.

30. Weller, A. *Progr. React. Kinetics* **1961**, *1*, 189.

31. Vander Donckt, E. *Progr. React. Kinetics* **1970**, *5*, 273.

32. Jaffe, H. H.; Jones, H. L. *J. Org. Chem.* **1965**, *30*, 964.

33. Perrin, D. D.; Dempsey, B.; Serjeant, E. P. *pK_a Prediction for Organic Acids and Bases* (Chapman and Hall, London, 1981), p. 22.

34. Laws, W. R.; Brand, L. *J. Phys. Chem.* **1979**, *83*, 795.

35. Gafni, A.; Brand, L. *Chem. Phys. Letts.* **1978**, *58*, 346.

36. Carnahan, B.; Luther, H. A.; Wilkes, J. O. *Applied Numerical Methods* (John Wiley & Sons, New York, 1969), p. 141.

37. Saff, E. B.; Snider, A. D. *Fundamentals of Complex Analysis* (Prentice-Hall, Englewood Cliffs, NJ, 1976), p. 242.

SECTION II. EXCITED STATE PROTON TRANSFER IN 9-AMINOACRIDINE CARBOXAMIDES IN DNA

INTRODUCTION

This section describes the principal conformational features of different types of DNA found through X-ray diffraction techniques of both natural DNA fibers and crystals of short-length DNA sequences. Different nucleic acid double helices are distinguished by the sequence of the base pairs, structural differences of their major and minor grooves, and differences in sugar puckering of their sugar-phosphate backbones.

A description of the intercalation process of drug molecules in DNA is presented with particular emphasis on the known intercalator 9-aminoacridine. The X-ray studies of DNA fibers and crystals to this date have had much more success in studying the structure of different types of DNA in comparison to DNA-drug intercalated complexes. The "universal" neighbor exclusion rule for intercalation is defined and challenged. Increasing the knowledge of drug intercalation will be directly useful in drug design by allowing the strengthening of the DNA-drug interaction or perhaps tailoring certain drugs for specific DNA sequences that have particular functional biological roles.

DNA Structure

The hereditary material contained in our bodies is a linear polymer called deoxyribonucleic acid (DNA) [1]. The more evolved a living organism is then the longer the length of the total DNA it contains [2]. Each repeating unit in the DNA polymer is called a nucleotide. A chain of nucleotides is called a polynucleotide and consists of an arrangement of nucleotides where the sugar of each nucleotide is linked by a phosphate group to the sugar

of the adjacent nucleotide. A general nucleotide is pictured in Figure 1 and is composed of a cyclic furanoside type sugar (β-D-2'-deoxyribose) that is phosphorylated in the C-5' position. At the C-1' position on the furanose ring one of four different bases is attached by a β-glycosyl $C_{1'} - N$ linkage. Figure 2 illustrates the four bases of DNA and the N atom that participates in the $C_{1'} - N$ linkage of the base to the sugar ring is indicated by a star (*) symbol. The four bases include two purine bases (adenine and guanine) and two pyrimidine bases (cytosine and thymine). The numbering scheme of Figures 1 and 2 is such that the sugar atoms are distinguished from the base atoms by giving the sugar atoms a prime. The most important feature of DNA is that these long polynucleotide chains are twisted about each other in the form of a regular double helix.

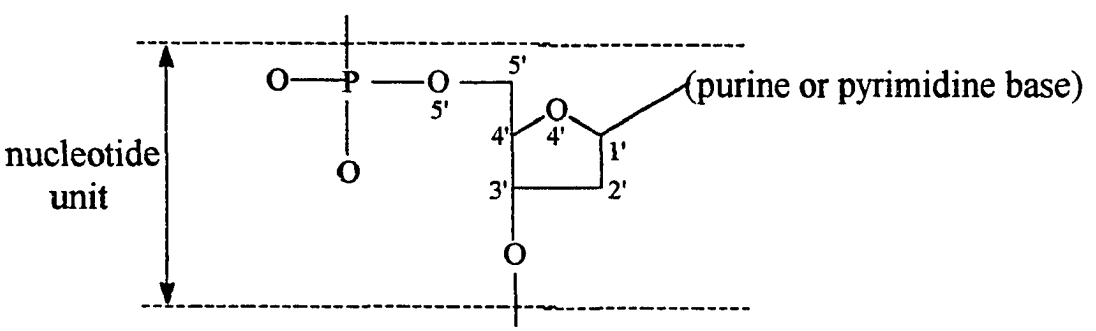

FIGURE 1 A single polynucleotide unit of DNA. The purine or pyrimidine base is attached at the C-1' atom of the furanose ring.

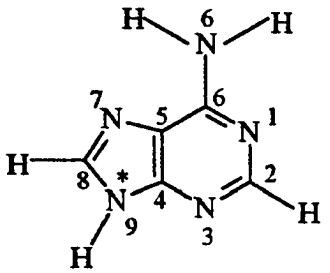

adenine

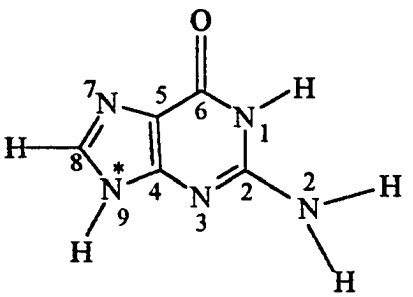

guanine

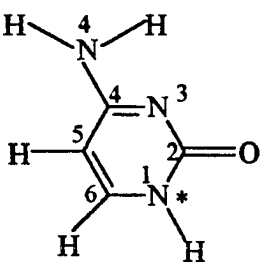

cytosine

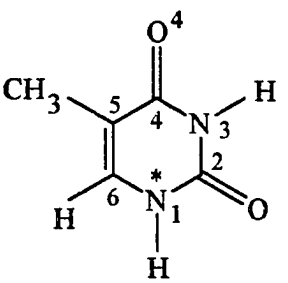

thymine

FIGURE 2 Chemical structure of the bases of DNA.

The 3-dimensional structure of DNA is the reason for many of its properties [2]. The most powerful technique to study the structural features of DNA is X-ray crystallography. In the early 1960's pure homogeneous DNA was not available for crystallization for X-ray analyses so diffraction patterns of DNA fibers under various conditions (e.g. humidity, salt, alcohol) were carried out [4]. The structural information obtained from fiber diffraction techniques using natural DNA fibers provides average structural information over the entire DNA molecule. Watson and Crick created a model of the 3-dimensional structure of DNA that arose partly out of the early X-ray analyses of DNA fibers [3]. The Watson-Crick model consists of two polynucleotide chains running in opposite directions and coiled around a common axis to form a right handed double helix. The purine and pyrimidine bases in their model of DNA are approximately perpendicular to the helix axis and are separated by a distance of ~3.4 Å [2]. The phosphate and deoxyribose sugar units run along the outside of the double helix and form a "backbone." Chagraff et al. [5] discovered that for DNA's of various compositions the ratios of adenine (A) to thymine (T) and guanine (G) to cytosine (C) were always one to one (i.e. 1:1 = A:T = G:C). In agreement with Chagraff's discovery the Watson-Crick model pairs the bases A with T and G with C. This pairing of the bases of DNA is often called Watson-Crick base pairing. The double helix in the Watson-Crick model is stabilized by hydrogen bonds connecting the paired bases and also by interactions between stacked bases on the same polynucleotide strand. Figure 3 shows AT base pairs connected by two hydrogen bonds and GC base pairs connected by three hydrogen bonds.

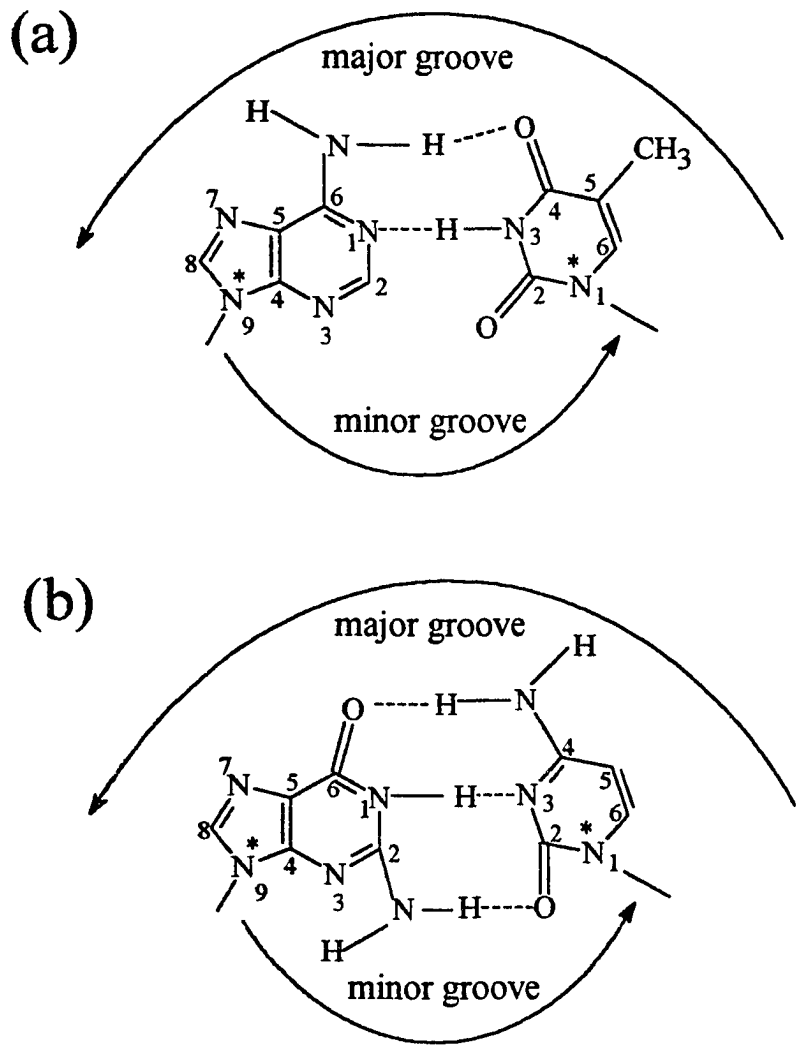

FIGURE 3 The major and minor grooves are lined with different potential hydrogen bond donors and acceptors. Figure (a) illustrates the hydrogen bonds between the base pair AT and (b) illustrates the hydrogen bonding between the base pair GC.

The development of triester methods of DNA synthesis has made it possible to prepare DNA of a predetermined sequence and for the first time to allow the growth of pure DNA crystals for X-ray analysis [4]. X-ray analyses of DNA crystals composed of four to twelve sequenced base pairs have shown that DNA at the molecular level has much structural diversity. For example X-ray analysis of crystallized DNA composed of short helical fragments of a repeating sequence of 10 base pairs, called a dodecamer, was synthesized by Dickerson et al. [6] with the sequence of base pairs: CGCGAATTCGCG. The overall structure of this dodecamer was found to closely resemble the Watson-Crick double helix model of DNA. The dodecamer however differed from the Watson-Crick model in that the dodecamer was not uniform in structure and had large local deviations compared to the Watson-Crick model. The Watson-Crick model has 10 base pairs per turn of its right handed double helix so a base pair is related to the next base pair along the DNA chain by a rotation of 36 degrees [1]. In Dickerson's dodecamer however the rotation angles relating each base pair falls in a range of 28 to 42 degrees [3]. Another difference discovered with Dickerson's dodecamer was that the base pairs in the dodecamer were not completely coplanar but twisted. The twisting of the base pairs in DNA is called "propeller twisting" and is pictured in Figure 4. Propeller twisting enhances the stacking of the bases in each DNA strand and allows greater interaction between adjacent bases increasing the stability of the DNA double helix [3]. Both the Watson-Crick model and Dickerson's dodecamer (CGCGAATTCGCG) are referred to as type B-DNA.

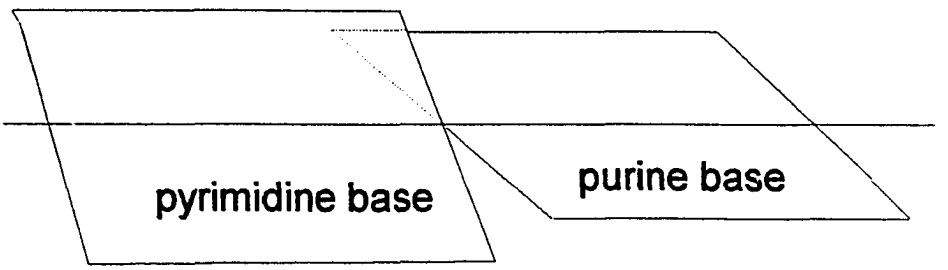

FIGURE 4 The bases of a DNA base pair are not coplanar but twisted.

The outer envelope of the B-DNA double helix is not cylindrically smooth but displays two grooves (major and minor) of different width and depth. The major groove of B-DNA is ~12 Å wide while the minor groove is ~6 Å wide and both grooves are of comparable depth ~8 Å [4]. The larger size of the major groove allows it to be more accessible for interactions with proteins that recognize specific DNA sequences [3]. The grooves arise because the glycosidic bonds of the base pairs are not diametrically opposite each other [1]. As shown in Figure 3 the minor and major grooves are on opposite sides of the DNA double helix and both grooves are lined with potential hydrogen bond donor and acceptor atoms. In the minor groove possible hydrogen bond acceptors include the N-3 atom of both adenine and guanine and the O-2 atom of both thymine and cytosine. The amino group attached to the C-2 atom of guanine can be a hydrogen donor.

X-ray diffraction of dehydrated DNA fibers reveal a different form of DNA called A-DNA. A-DNA appears when the relative humidity is below ~75% [2]. Dehydration favors

A-DNA over B-DNA because the phosphate backbone binds fewer water molecules in A-DNA than in B-DNA [3]. A-DNA like B-DNA is a right handed double helix made up of antiparallel polynucleotide chains held together by Watson-Crick base pairing. Dickerson studied A-DNA through single crystal X-ray analysis of the tetramer CCGG [6]. The A-DNA helix is wider and "stubbier" than the B-DNA helix and the base pairs in A-DNA are much more tilted relative to the helix axis than the base pairs in B-DNA [4]. A-DNA also has a deep major groove relative to B-DNA and a minor groove that nearly vanishes. Many of the structural differences between A- and B-DNA arise from different puckerings of the five member furanoside sugar rings in the sugar-phosphate backbones of A- and B-DNA [3].

The five member sugar rings in the sugar-phosphate backbones of DNA are not planar but can be puckered in an envelope (E) form or in a twist (T) form. Both puckering forms are pictured in Figure 5. The E form of puckering has four of the five atoms in the same plane with the fifth atom out by about 0.5 Å while the T form has two adjacent atoms displaced out of the plane of the remaining three atoms of the sugar ring [2]. If the atom displaced from these four or three atom planes is on the same side as the C-5' atom in Figure 1 then it is called "endo" and atoms displaced on the opposite side of C-5' are called "exo." For example sugar units with the C-2' atom displaced and on the same side as the C-5' atom in the sugar ring results in a $C_{2'}$-endo sugar. Traditionally the $C_{3'}$-endo or $C_{2'}$-exo conformation has been assumed for A-DNA and the $C_{2'}$-endo or $C_{3'}$-exo conformation for B-DNA. However Dickerson et al. has shown that this is an oversimplification [4].

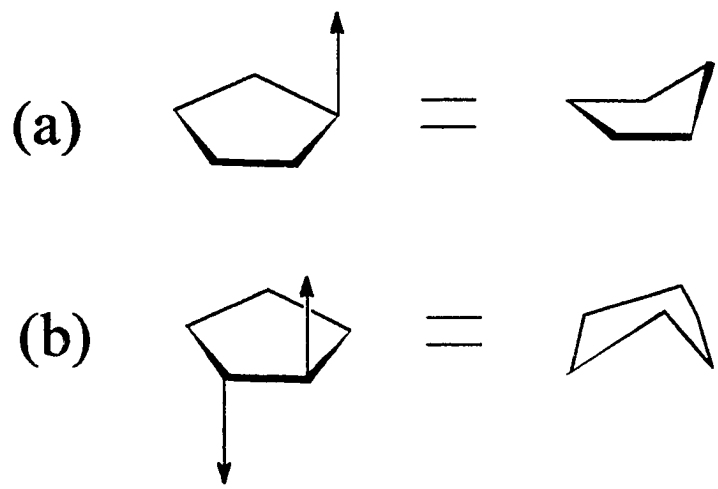

FIGURE 5 The five member sugar ring is nonplanar. It can be puckered in the envelope (E) form in (a) or the twist (T) form in (b).

The third type of DNA helix is called Z-DNA and was discovered by Rich et al. [7] with X-ray analysis of the hexamer CGCGCG. Z-DNA is also a double helix but is left handed in comparison with A- and B-DNA. The minor groove of Z-DNA is deep while the major groove is flattened out. The phosphates in the backbone of Z-DNA are "zigzagged" hence the name Z-DNA. The zigzagging is a consequence of the repeating unit being a dinucleotide rather than a mononucleotide [4]. The electrostatic repulsions between phosphate groups are stronger in Z-DNA than in B-DNA because the closest groups on opposite strands are 8 $\mathring{A}$ rather than 12 $\mathring{A}$ apart [3]. Z-DNA requires a high ionic strength environment to maintain its integrity [10].

X-ray analyses have shown that certain DNA sequences are disposed to certain types of DNA structure. Neighboring sequences will certainly play a role in determining the overall structure of the DNA molecule. It is doubtless that more forms of DNA remain to be discovered [10].

Intercalation

At the macroscopic level the most common cited effects of intercalative agents in DNA are inhibition of cell growth, cell death, and cell transformation [8]. At the subcellular level the anti-cancer activity and cytotoxicity of intercalative agents are associated with interference in some aspect of transcriptional, translational, and replicative processes as well as gross DNA damage and consequent misrepair [10]. For example the known intercalator 9-aminoacridine exhibits frameshift mutagenesis (described later) and is an anti-tumor agent [20].

Intercalation is a mode by which foreign molecules interact with nucleic acids. Intercalation occurs when the foreign molecule possesses a planar aromatic chromophore with dimensions similar to a base pair in DNA corresponding to about three fused six-member rings [24]. Charge transfer interactions have been shown to be important in the binding of intercalating ligands to DNA [28]. Many intercalators are thus cationic and/or possess one [25] or two [26, 27] cationic side chains. The side chains seem to provide additional stabilization to the drug-DNA complex and influence the kinetics of the binding process [24]. The now generally accepted intercalation model suggested by Lerman [9]

describes intercalation as the insertion of the flat aromatic ring portion of the intercalator in-between adjacent stacked base pairs of a double stranded polynucleotide. The environment for an intercalated drug in DNA resembles that of an organic solvent because the intercalated drug is surrounded by purine, pyrimidine, and sugar moieties. Striking evidence of this organic environment has been illustrated by intercalated dyes in DNA where there are striking similarities of the spectroscopic properties of intercalated dyes and of the same dyes dissolved in organic solvents [13]. Kinetic studies by Marcandalli et. al. [33] have shown that for a group of intercalating dyes, including 9-aminoacridine, both the molecular structure of the dye and the type of DNA deeply influence the dynamics of the intercalation process. This is consistent with the idea that in order for a molecule to intercalate it must approach DNA through either the major or minor groove making the relative dimensions of the two grooves sterically important [10].

The intercalation process results in a number of changes to DNA molecular properties overall making DNA longer and stiffer. As a drug molecule intercalates it causes a lengthening of DNA due to insertion of the drug molecule between adjacent base pairs of DNA. The theoretical length extension for B-DNA is 3.4 $\mathring{A}$ per intercalated drug molecule [8]. One result of intercalated or "stretched" DNA is frameshift mutagenesis. Frameshift mutagenesis is the process where a base pair is miscopied (added or deleted) during the replication process of DNA [29]. The double helix stability of DNA is increased upon intercalation relative to single strand DNA. This is known through increased melting

temperatures of double strand DNA [1]. The melting temperature is the temperature double strand DNA begins to unwind to form single strand DNA. The base pairs at and around the binding site in DNA are partially unwound at intercalation sites [10]. For example the known intercalator ethidium bromide [30] exhibits an unwinding angle of 26 degrees measured relative to non-intercalated sites in DNA [11]. Unwinding angles greater than 26 degrees are indicative of bis-intercalation such as the 48 degree unwinding angle for echinomycin which contains two intercalating chromophores linked by a cyclic octapeptide [12].

The success mentioned in the previous section in determining DNA structure by fiber and single-crystal X-ray diffraction studies has prompted similar studies on DNA-drug intercalated complexes. The structural studies on DNA-drug complexes however have not had much success due to the limitations of the fiber diffraction method and single-crystal techniques. Natural DNA fibers when complexed with intercalative drugs produce poor quality diffraction patterns and this may be due to several reasons [14, 15]. Upon intercalation there may be non-equivalent structural changes to the DNA phosphate backbone and/or to the adjacent base pairs involved in intercalation. Disordered multiple orientations of the intercalated drug molecules in DNA could also complicate the diffraction patterns. Single-crystal studies to this date have been confined to using dinucleosides complexed with an intercalating drug to study DNA-drug intercalative structure [10]. A dinucleoside is pictured in Figure 6 and is the simplest possible model for a DNA-drug complex. The significance and role of end effects in such short DNA fragments is unknown. The structural

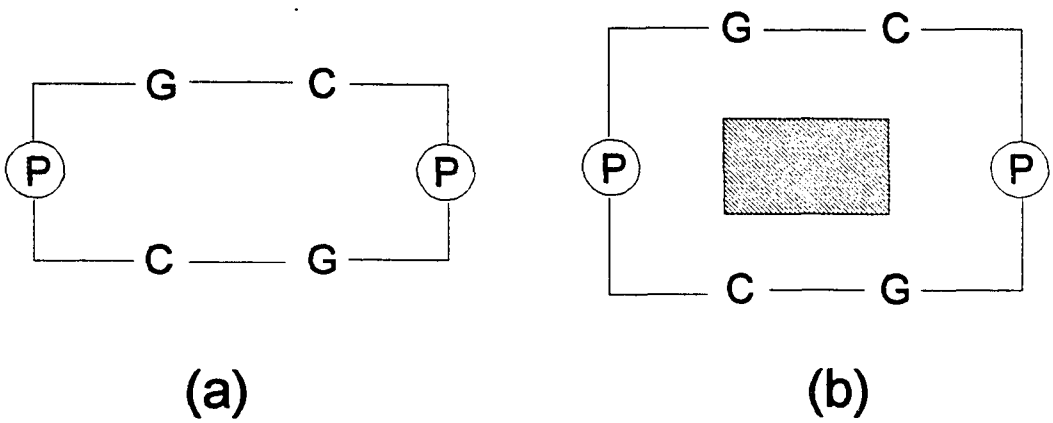

FIGURE 6 Schematic outline of a base paired dinucleoside (a) without intercalated drug and (b) with intercalated drug. Dashed lines indicate base pairing, P indicates the sugar phosphate backbone of DNA while G and C represent the bases guanine and cytosine, respectively.

features determined from such extremely short helical fragments may either be particular to the structure concerned or may be a more general (averaged) property of the dinucleoside crystal [10]. X-ray studies of a crystal consisting of a dinucleoside complex of 9-aminoacridine with 5-iodo-CG base pairs [21, 22] has revealed two distinct intercalated duplex complexes. One has the amino group of 9-aminoacridine pointing towards what would be the minor groove side of DNA and the other complex has 9-aminoacridine rotated 180 degrees and intercalated asymmetrically between the bases of one strand only. The second complex allows sufficient space for several equi-energetic stacking positions for the intercalated 9-aminoacridine molecule. This feature has been proposed to be an integral part

of the mechanism for the observed frameshift mutagenesis observed with 9-aminoacridine [10].

The neighbor exclusion rule is widely regarded as an intrinsic and universal characteristic of the intercalative binding of drugs to DNA [19]. The rule suggests that intercalative DNA binding by small molecules can only occur at every other base pair site. This viewpoint however has been challenged both experimentally and theoretically. Atwell et al. [16] studied the binding of DNA to a diacridine consisting of two charged acridines joined together by a rigid linker chain. Atwell found that both chromophores intercalate even though the shortness of the linker chain precludes the separation of the bound chromophores by more than one base pair. Therefore the intercalation of their diacridine molecule violates the neighbor exclusion rule. Rao et al. [17] carried out molecular mechanics and molecular dynamics simulations to study intercalation complexes between 9-aminoacridine and the base paired heptanucleotide d(CGCGCGC)·d(GCGCGCG). Rao found that the neighbor exclusion rule was both obeyed and violated depending on the stereochemical energy, vibrational entropy, counterion release, and solvent-solute interactions of the system.

In general the number of base pair excluded sites increases in relation to the complexity of the intercalating drug [10]. An intercalated drug molecule may not only exclude the site it occupies from further binding but may exclude one or more neighboring sites as well and this type of binding is called anticooperative binding. The charged phosphate groups of the DNA double helix generate polyelectrolyte effects that are extremely important for DNA

conformations [31]. Thus there may very well be a polyelectrolyte contribution to the drug-DNA anticooperative binding [18]. Friedman et al. [19] outlined a general theory of the anti-cooperativity and salt dependence of ligand-polyion site binding and applied it to the binding of 9-aminoacridine to DNA. The best estimate (with polyelectrolyte effects not taken into account) was two to three base pair sites excluded per bound 9-aminoacridine molecule. However when polyelectrolyte effects are taken into account this number is reduced to one excluded base pair site per intercalated 9-aminoacridine molecule. Polyelectrolyte effects were found to strongly reduce the effective value of the binding constant of 9-aminoacridine to DNA.

In conclusion for the small number of drugs studied to date intercalation can be remarkably site selective and there may be unknown ramifications of drug binding on nucleotides remote from the intercalation site itself [10]. Bret et al. [23] studied the energy transfer rate between various chromophores intercalated in DNA and found evidence of non random distributions for certain pairs of dyes intercalated in DNA. It is important to realize that unwinding angles and binding constants for intercalated molecules are averaged values over all possible sites in the DNA molecule. Compositional and sequence variations in DNA make it an oversimplification to assign a single binding constant to all intercalative binding sites [8]. Preference for intercalative binding can be affected by the type of base pair, side chains on the ligand, and different ring systems of the intercalating chromophore [8]. Sequence preference for 9-aminoacridine intercalated in B-DNA was studied by Cieplak et al.

[32] using Free Energy Perturbation Molecular Dynamics Simulations. Cieplak found that 9-aminoacridine energetically prefers to intercalate into GC rich neighborhoods of DNA.

References

1. Freifelder, D. In *The DNA Molecule* W. H. Freeman and Company: San Francisco, CA **1978**.

2. Saenger, W. In *Principles of Nucleic Acid Structure* Ed. Cantor, C. R., Springer-Verlag: New York, NY, **1984**.

3. Stryer, L. In *Biochemistry* 3rd Edn., W. H. Freeman and Company: New York, NY, **1988**.

4. Dickerson, R. E.; Drew, H. R.; Conner, B. N.; Wing, R. M.; Fratini, A. V.; Kopka, M. L. *Science* **1982**, April 30, 216, 475-485.

5. Zamenhof, S.; Brawermann, G.; Chargraff, E. *Biochim. Biophys. Acta* **1952**, 9, 402-405.

6. Dickerson, R. E.; Drew, H. R.; Conner, B. N. In *Biomolecular Stereodynamics* Sarma, R. H. Ed., Adenine Press: New York, NY, **1981**, 1-34.

7. Rich, A.; Nordheim, A.; Wang, A. H. J. *Ann. Rev. Biochem.* **1984**, 53, 791-846.

8. Berman, H. M.; Young, P. R. *Ann. Rev. Biophys. Bioeng.* **1981**, 10, 87-114.

9. Lerman, L. S. *J. Mol. Biol.* **1961**, 3, 18.

10. Neidle, S.; Abraham, Z. *CRC Crit. Rev. in Biochem.* **1984**, Vol. 17, Issue 1, 73-121.

11. Wang, J. C. *J. Mol. Biol.* **1974**, 89, 783.

12. Wakelin, L. P. G.; Waring, M. J. *Biochem. J.* **1976**, 157, 721.

13. Lober, G. *J. Luminescence* **1981**, 22, 221-265.

14. Arnott, S.; Chandrasekaran, R. In *Proc. 2nd SUNYA Conversation in the Discipline of Biomolecular Stereodynamics*, Sarma, R. H. Ed., Adenine Press: New York, **1981**, 99.

15. Arnott, S. In *Topics in Nucleic Acid Structure* Neidle, S. Ed., Macmillan Press: London, **1981**, 65.

16. Atwell, G. J.; Stewart, G. M.; Leupin, W.; Denny, W. A. *J. Am. Chem. Soc.* **1985**, 107, 4335.

17. Rao, S. N.; Kollman, P. A. *Proc. Natl. Acad. Sci. U.S.A.* **1987**, 84, 5735-5739.

18. Friedman, R. A. G.; Manning, G. S.; Shahin, M. A. In *Chemistry and Physics of DNA-Ligand Interactions* Kallenbach, N. R. Ed., Adenine Press: Guilderland, NY, **1990**, 37-64.

19. Friedman, R. A.; Shahin, M.; Zuckerbraun, S.; *J. Biomol. Struc. & Dyn.* **1991**, Vol. 8, Issue 5, 977-987.

20. Schurr, J. M.; Wu, P.; Fujimoto, B. S. *Time-Resolved Laser Spectroscopy in Biochemistry II* **1990**, SPIE Vol 1204, 368-379.

21. Sakore, T. D.; Jain, S. C.; Tsai, C. C.; Sobell, H. M. *Proc. Natl. Acad. Sci. U.S.A.* **1977**, 74, 188.

22. Sakore, T. D.; Reddy, B. S.; Sobell, H. M. *J. Mol. Biol.* **1977**, 114, 301.

23. Le Bret, M.; Le Pecq, J.; Barbet, J.; Roques, B. P. *Nucleic Acids Research*, **1977**, Vol. 4, Num. 5, 1361-1379.

24. Atwell, G. J.; Cain, B. F.; Baguley, B. C.; Finlay, G. J.; Denny, W. A. *J. Med. Chem.* **1984**, 27, 1481.

25. Zee-Cheng, R. K.-Y.; Podrebarac, E. G.; Menon, C. S.; Cheng, C. C. *J. Med. Chem.* **1979**, 22, 501.

26. Zee-Cheng, R. K.-Y.; Cheng, C. C. *J. Med. Chem.* **1978**, *21*, 291.

27. Murdock, K. C.; Child, R. G.; Fabio. P. F.; Angier, R. B.; Wallace, R. E.; Durr, F. E.; Citarella, R. V. *J. Med. Chem.* **1979**, 22, 1024.

28. Gabbay, J. *J. Am. Chem. Soc.* **1968**, 90, 6574.

29. Zubay, G. In *Biochemistry* 3rd Edn., Kane, K. Ed., Wm. C. Brown Publishers: Dubuque, IA, **1993**.

30. Atherton, S. J.; Beaumont, P. C. *Photobiochemistry and Photobiophysics* **1984**, 8, 103-113.

31. Wilson, W. D.; Krishnamoorthy, C. R.; Wang, Y.-H.; Smith, J. C. *Biopolymers* **1985**, 24, 1941-1961.

32. Cieplak, P.; Rao, S. N.; Grootenhuis, P. D. J.; Kollman, P. A. *Biopolymers* **1990**, 29, 717-727.

33. Marcandalli, B.; Stange, G.; Holzwarth, *J. F. J. Chem. Soc., Faraday Trans. 1* **1988**, 84, 8, 2807-2819.

FLUORESCENCE KINETICS OF 9-AMINOACRIDINE CARBOXAMIDE INTERCALATORS IN DNA

A paper to be submitted to the *Journal of Physical Chemistry*

Charles A. Smith, Walter S. Struve, Graham J. Atwell, William A. Denny*

Abstract

The effects of DNA binding on the ground and excited state proton transfers of several *N*-((dimethylamino)-alkyl)-9-aminoacridine carboxamide intercalators have been studied by steady-state electronic spectroscopy and by time-correlated single photon counting. The fluorescence kinetics are dominated by intercalators bound to (dA)-(dT) sites, because fluorescence is extensively quenched for intercalators in poly(dG)-poly(dC). Binding to calf thymus DNA increases the equilibrium constant pK_{a1} for the first deprotonation of the ground state aminoacridines by 0.7-1.0 units; it similarly increases the equilibrium constants pK_{a2}, pK_{a2}^* for the second deprotonation in the ground and excited states. However, DNA binding does *not* block excited state proton transfers at the first deprotonation site, since the pH-dependent fluorescence kinetics indicate that pK_{a1}^* for the first excited state deprotonation is several units below pK_{a1}. Hence, specific interactions between the first deprotonation site (which is likely to be the 9-amino group) and the phosphate backbone do not appear to be involved in binding to (dA)-(dT) sites. The steady-state and time-resolved

electronic spectroscopy of the intercalators in the presence of DNA undergo a transition to those of the free intercalator at pH ~ 9.5-10, indicating that dissociation from the polynucleotide occurs at these pH.

Introduction

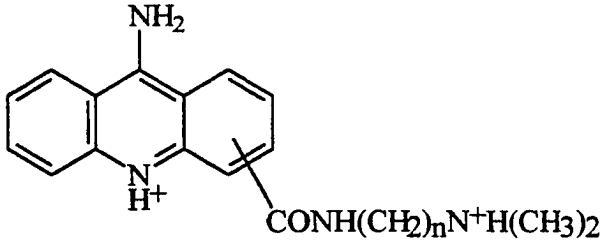

1

While investigating criteria for cytotoxicity in DNA intercalators, Denny and coworkers [1] synthesized a series of N-(dimethylaminoalkyl)-9-aminoacridine carboxamides (**1**). These compounds (hereafter called *m*-*n*C to denote the species in which the side chain is substituted in the *m*-position of the aminoacridine substrate, and contains *n* carbon atoms between the proximal and distal N atoms) are structurally analogous to many known cytotoxic intercalators [2-7]. They contain a fused tricyclic aromatic chromophore with a side chain that is cationic at physiological pH. The binding affinity of all compounds in this series is aided by extensive van der Waals contact between the planar chromophore and the

neighboring DNA base pairs, and the presence of the electron-withdrawing carboxamide group in the side chain fosters DNA-intercalator charge-transfer interactions.

Nevertheless, the only cytotoxic compound in this series is 4-2C, in which the side chain is located at the 4-position and contains 2 carbon spacer atoms. The reason for this striking selectivity is unclear, in part because few techniques exist for direct characterization of DNA-intercalator binding conformations. Kinetic studies of other intercalators [8-10] suggest that their cytotoxicity correlates with slow DNA-intercalator dissociation rates, so that binding kinetics rather than energetics may govern their biological activity. In a similar vein, only compound 4-2C in the series *m-n*C shows kinetic evidence for long-lived DNA-intercalator complexes [11]. However, the possibility remains that the antitumor activity of 4-2C stems from metabolic factors that are unrelated to DNA-intercalator interactions *per se*.

In this work, we have investigated the steady-state and time-resolved electronic spectroscopy of compounds *m-n*C intercalated in double-stranded calf thymus DNA. Their excited state kinetics in solution, extensively investigated in an earlier companion paper [12], are dominated by intermolecular excited-state proton transfer reactions. The presence in *m-n*C of three distinct deprotonation sites with differing pK_a (the pyridine N atom, the distal N atom in the side chain, and the amino group) endows the solution fluorescence kinetics with considerable complexity. The pH-dependent steady-state spectra and fluorescence kinetics both change drastically when *m-n*C is intercalated into DNA, so that the solution studies [12]

provide a useful foil for the effects of the DNA environment on intermolecular proton transfers. Our work thus offers potential insights into DNA-intercalator binding modes.

Materials and Methods

The preparation and identification of the 9-aminoacridine carboxamides **1** have been reported previously [1]. At neutral pH, the carboxamide dihydrochlorides are protonated at the 9-aminoacridine chromophore and at the distal N atom. All absorption spectra were obtained using a Perkin-Elmer Lambda 3B UV-vis spectrophotometer. Steady-state fluorescence spectra were obtained on a Spex Fluorolog 2 spectrofluorimeter with 4.3 nm excitation and detection bandpass. Double-stranded calf thymus DNA was obtained from Sigma Chemical Company. The pH of DNA-carboxamide adducts was adjusted by incremental addition of concentrated HCl or KOH, and monitored using a Fisher Scientific 915 pH meter. In all steady-state and time-resolved experiments, the DNA loading in the DNA-intercalator adducts (expressed as occupied binding sites divided by available binding sites) was $r = 0.06$ unless otherwise specified. If the DNA-intercalator binding probability at a given site is independent of neighboring site occupancy, this loading ensures that the binding sites adjacent to the majority (>90%) of the intercalators are unoccupied.

The time-correlated single photon-counting apparatus [12] incorporated a Hamamatsu R1564U microchannel plate phototube, a B&H Electronics AC3011 21 dB preamplifier, an EG&G Ortec 457 time-to-amplitude converter, a Tennelec TC455 constant-fraction discriminator used for STOP and START pulses, and an EG&G ACE multichannel

analyzer (MCA). Samples (housed between quarter-wavelength optical flats separated by a 180 μm Teflon spacer) were excited at 400 nm with 10 ps fwhm pulses from a frequency-doubled, synchronously pumped styryl 8 dye laser that was cavity-dumped at 3.8 MHz. Fluorescences were analyzed using a magic-angle Glan prism polarizer to eliminate anisotropy decay components arising from energy transfer and/or rotational diffusion. (While rotational diffusion of DNA does not occur during the aminoacridine fluorescence lifetimes reported here, the intercalators become unbound at high pH.) Count rates were less than 5000 counts/s. Fluorescence decays were transferred from the MCA to an Electra 486DX-33 personal computer, where convolute-and compare analyses were carried out using a simplex algorithm in Borland C++. Fluorescence from *N*-acetyltryptophan amide in water (<0.05 mM) was single-exponential ($\chi^2 < 1.11$) with lifetime 2995 ± 40 ps [13].

Results

The steady-state absorption spectrum of double-stranded calf thymus DNA itself varies with pH, as shown in Fig. 1. While the longest-wavelength DNA absorption band maximum at ~250 nm lies considerably to the blue of the *m*-*n*C absorption band systems studied here (350-450 nm), pH increments produce increased baselines at wavelengths overlapping the intercalator bands. The circular dichoism is concomitantly reduced at high pH (data not shown). This situation precludes detailed analyses of isosbestic behavior in the pH-dependent steady-state spectra of the intercalators, which provided evidence for sequential deprotonations in the unbound intercalators [12].

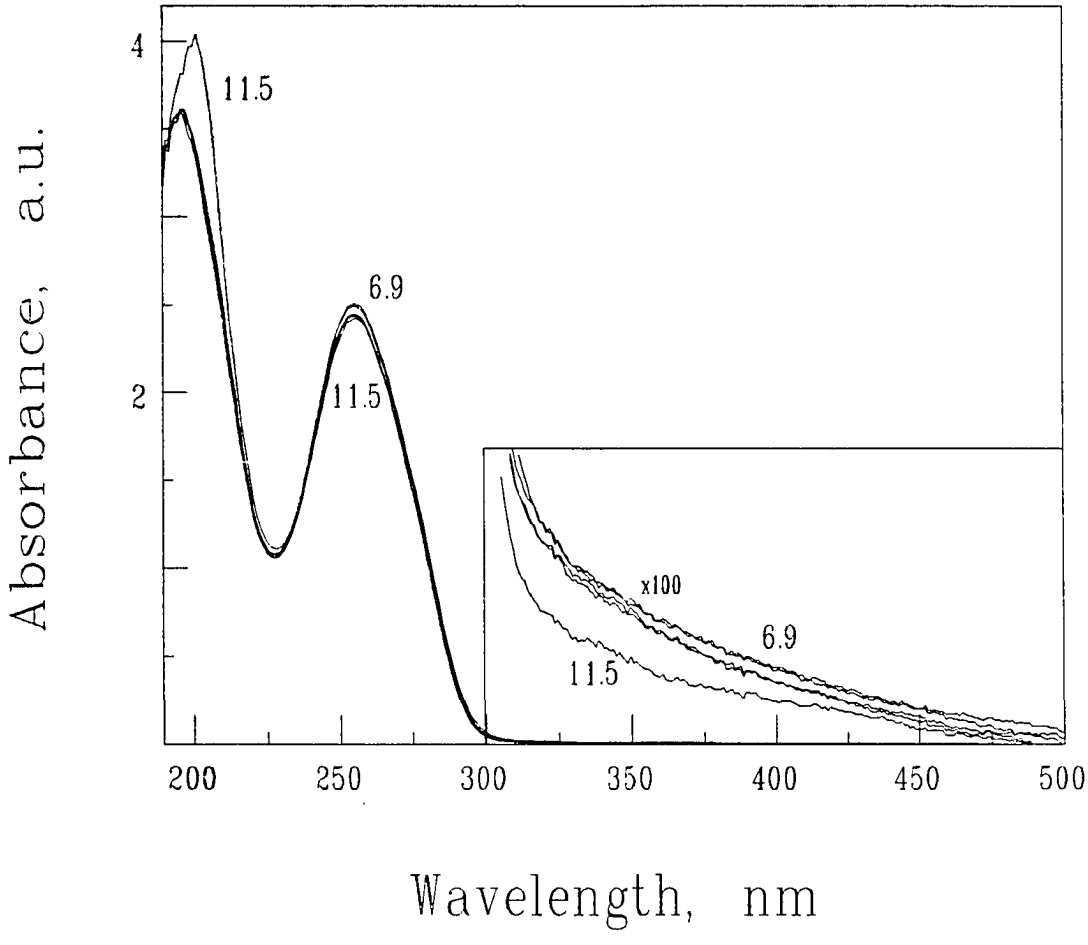

Figure 1. pH dependence of steady-state absorption spectrum for double-stranded calf thymus DNA. pH values are 6.9, 8.0, 9.0, 9.9, and 11.5.

In Figure 2, we contrast the pH-dependence of the absorption spectra for the free and DNA-bound carboxamides 2-2C, 4-2C, and 4-5C. At low pH, the absorption spectra of the bound and free intercalators exhibit similar Franck-Condon envelopes; the bound intercalator spectra are typically red-shifted by 6-9 nm from the free spectra. The free intercalator spectra undergo pH metamorphoses in consequence of successive deprotonations at three different sites on the chromophore and carboxamide side chain [12]. The pH effects on the absorption spectra of the bound intercalators for pH between ~8.5 and ~9.5 are far less marked than in the case of the free intercalators. At high pH (> 9), increased absorption grows in at the red edge of the bound intercalator absorption spectrum (460-490 nm in the case of 4-2C). At very high pH (>11 for 4-2C), a qualitatively different spectrum appears, with vibrational features that contrast with those of the bound intercalator at lower pH. This spectrum closely resembles the free intercalator spectrum in the limit of high pH, suggesting that the DNA-bound intercalators become free at high pH. This interpretation is corroborated by pH trends in the steady-state fluorescence spectra (see below).

Figure 2 indicates that the onset of absorption spectral changes occurs at much lower pH for the free intercalators (pK_a = 8.6 for the first ground state deprotonation in 2-2C, pK_a = 8.3 in 4-2C [12]) than for the corresponding bound intercalators. Hence, intercalation strongly modulates the ground state proton transfer equilibria in these carboxamides.

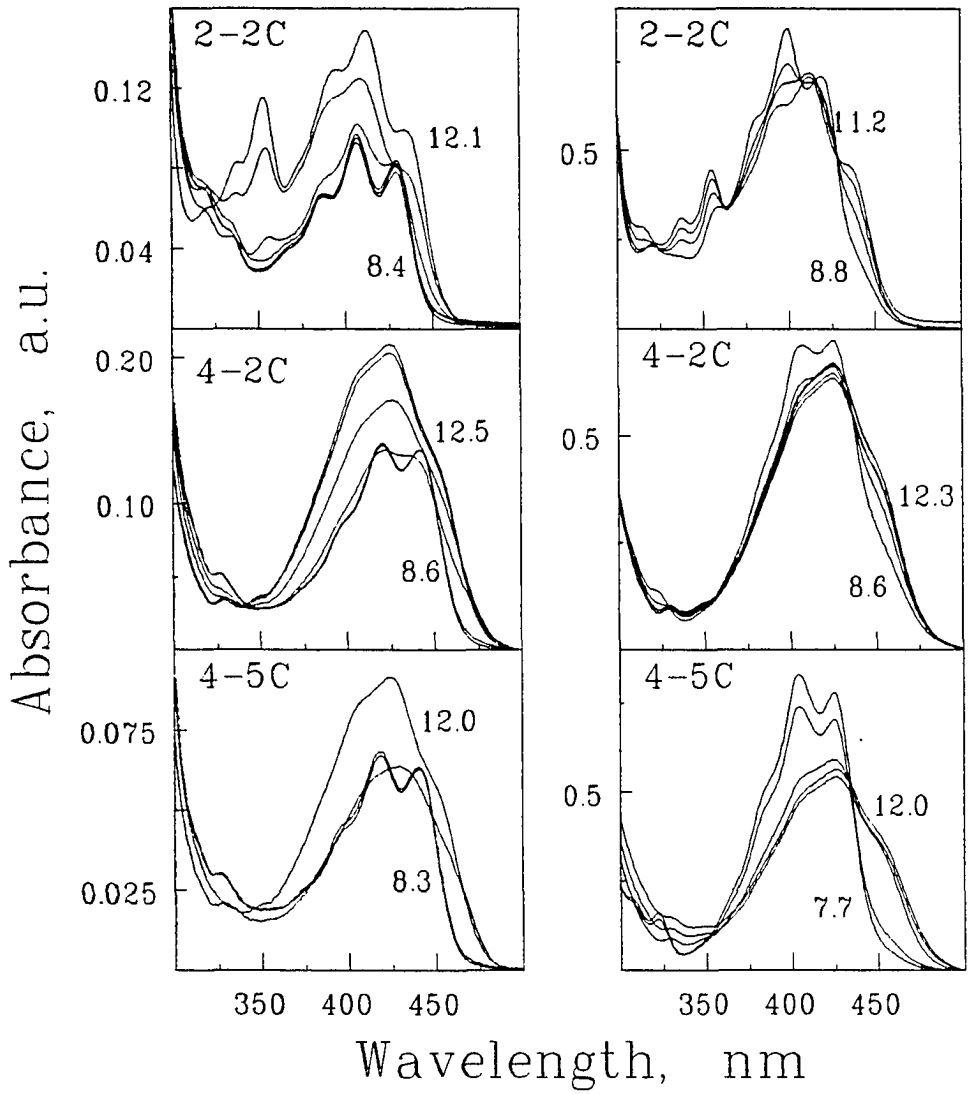

Figure 2. pH dependence of steady-state absorption spectra of the intercalators 2-2C, 4-2C, and 4-5C in the presence and absence of double-stranded DNA (left and right columns, respectively). Maximum DNA loading (at low pH) is $r = 0.06$. pH values for bound intercalators (left column) are 8.4, 9.6, 10.0, 11.0, 11.6, 12.1 for 2-2C; 8.6, 9.5, 10.9, 11.5, 12.0, and 12.5 for 4-2C; and 8.3, 10.0, 11.5, and 12.0 for 4-5C. pH values for free intercalators (right column) are 8.8, 9.5, 10.1, and 11.2 for 2-2C; 8.6, 9.4, 10.4, 11.2, 12.0, and 12.3 for 4-2C; and 7.7, 8.9, 9.9, 11.7, and 12.0 for 4-5C.

The effects of pH on the steady-state fluorescence spectra of bound and free 2-2C, 4-2C, and 4-5C are shown in Fig. 3. In the limit of high pH, the fluorescence spectra of the apparent onset of metamophoses in the "bound" intercalator fluorescence spectra occurs at considerably lower pH than in the corresponding absorption spectra. This effect arises primarily from differences in fluorescence yields, rather than from lower pK_a^* values for excited state (as opposed to ground state) proton transfers in the bound intercalators.

Time-resolved fluorescence profiles of the free and DNA-bound carboxamides 2-2C and 4-2C were studied under 400 nm excitation and broadband detection ($\lambda > 450$ nm). The results are summarized in Figures 4 and 5, which give the pH dependence of the lifetimes and preexponential factors, respectively, from triexponential fits to the isotropic fluorescence decays. These kinetic parameters have already been reported for the free carboxamides in water [12]; the free intercalator parameters are included here for comparison with the corresponding parameters for the DNA-bound intercalators.

For both 2-2C and 4-2C, the fluorescence decay becomes nearly single-exponential in the presence of DNA at pH ~ 11. At this pH, the empirical long-component lifetime is essentially the same for the free and "bound" intercalators (~12 ns for 4-2C, ~ 17 ns for 2-2C). For such pH, the bulk of the intercalators appear to be dissociated from the polynucleotide. For pH > 11, the pH-dependence of the long-component lifetime is similar for the free and dissociated intercalators.

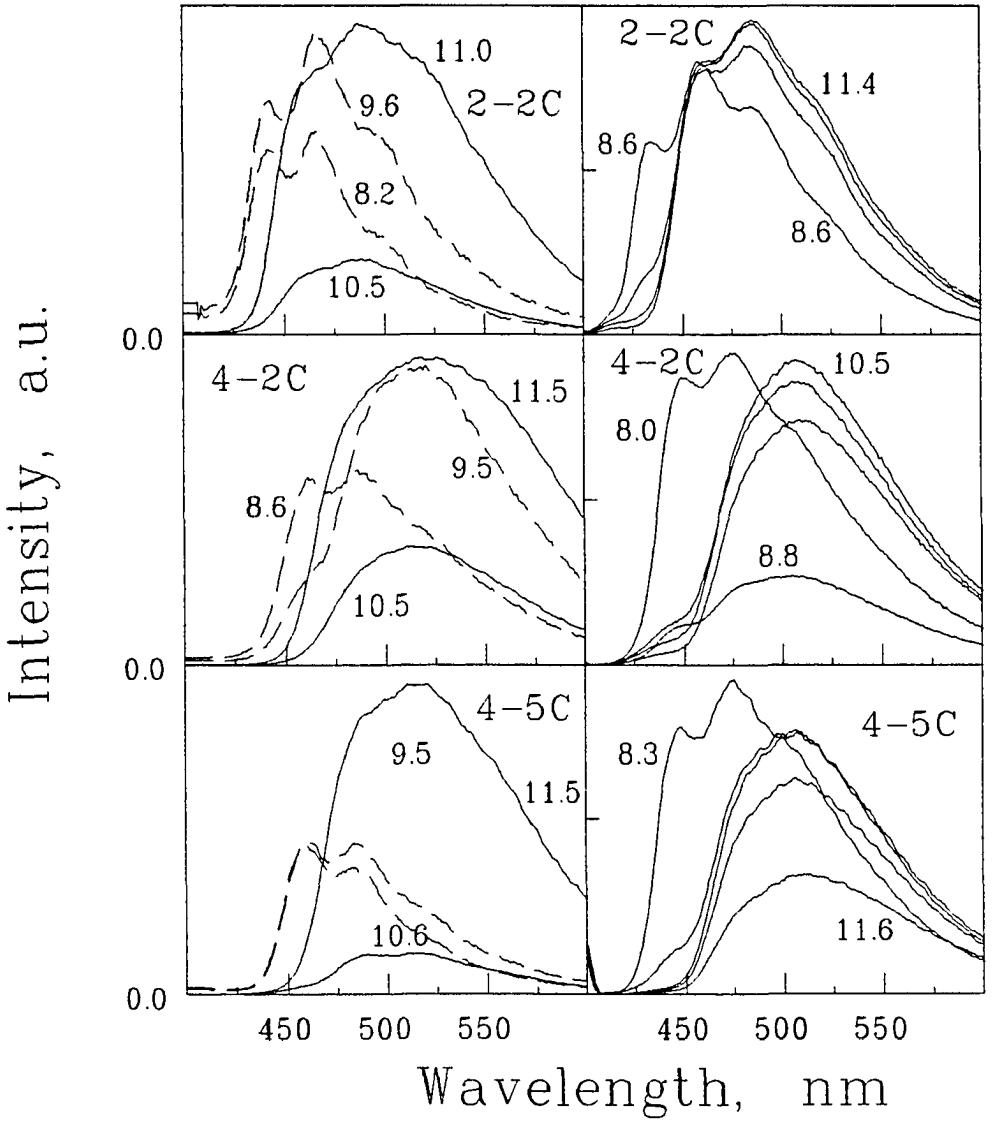

Figure 3. pH dependence of steady-state fluorescence spectra of 2-2C, 4-2C, and 4-5C in the presence and absence of double-stranded DNA (left and right columns, respectively). Maximum DNA loading is $r = 0.06$. Dashed curves for bound intercalators (left column) indicate fluorescence spectra multiplied by x20. pH values for free intercalators (right column) are 8.6, 9.8, 10.7, and 11.4 for 2-2C; 8.0, 8.8, 9.6, 10.5, and 11.5 for 4-2C; and 8.3, 9.6, 10.9, 11.1, and 11.6 for 4-5C.

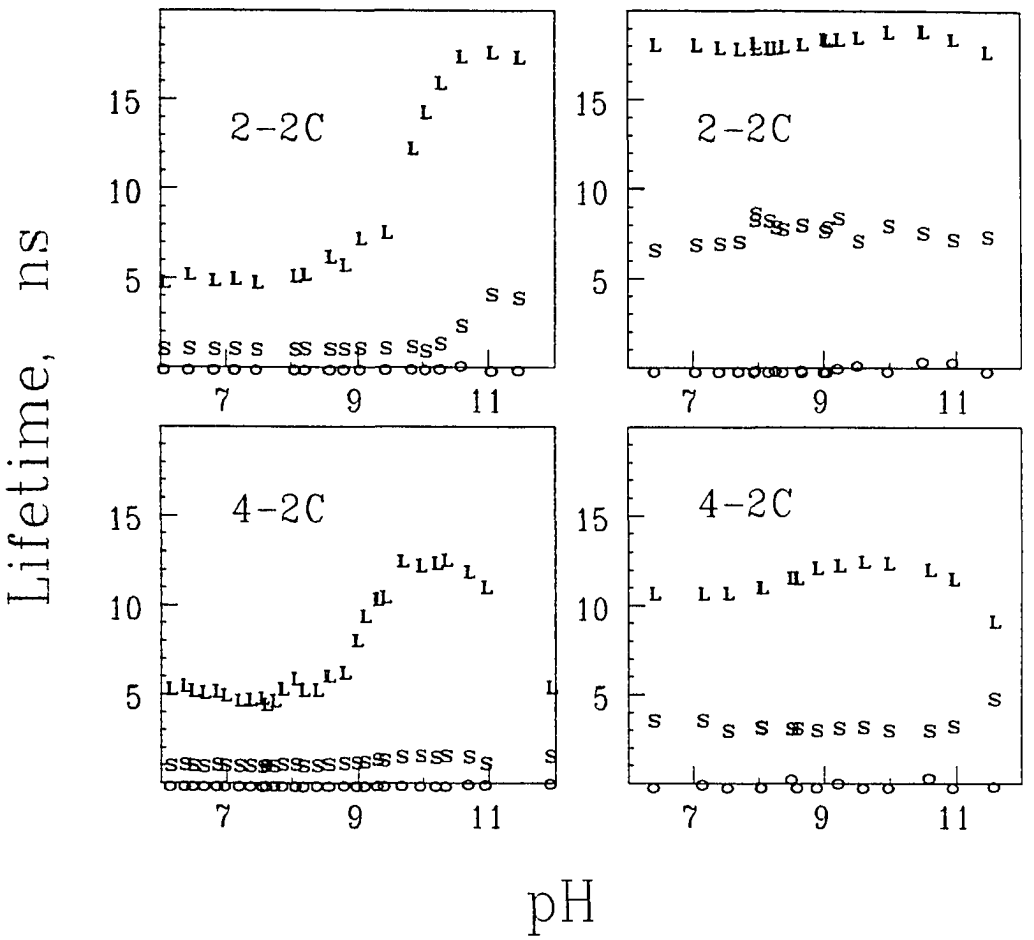

Figure 4. pH dependence of fluorescence component lifetimes for 2-2C and 4-2C in the presence and absence of double-stranded DNA (left and right columns, respectively), derived from triexponential fits to isotropic decays. Maximum DNA loading is $r = 0.06$. Excitation wavelength was 400 nm. Data points for the long, intermediate, and subnanosecond components are labeled L, S, and o, respectively.

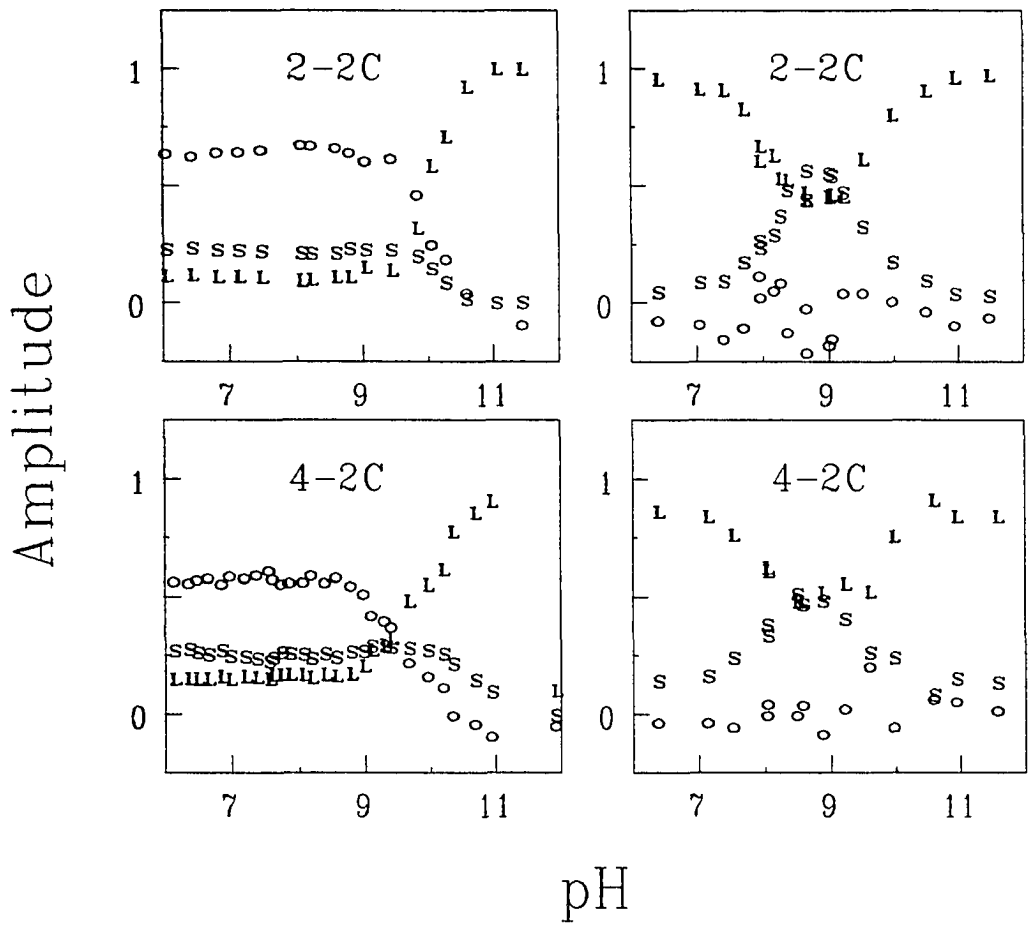

Figure 5. pH dependence of fluorescence preexponential factors for 2-2C and 4-2C in the presence and absence of double-stranded DNA (left and right columns, respectively), derived from triexponential fits to isotropic decays. Maximum DNA loading is $r = 0.06$. Excitation wavelength is 400 nm. Data point legend is the same as in Fig. 4.

For pH < 8 (where essentially all of the intercalators are bound in the presence of DNA), the long-component lifetime becomes appreciably shorter (~5 ns in both 2-2C and 4-2C) than for the free intercalators. However, for the bound intercalators at these pH, the fluorescence decay becomes dominated by a subnanosecond lifetime component (preexponential factor > 0.5), as shown in Fig. 5. No such major subnanosecond component is found in the free intercalators at any pH; the minor picosecond components in that case likely arise at least in part from dynamic solvation. Both of the bound 2-2C and 4-2C species also exhibit an intermediate component (amplitude ~ 0.25) with lifetime ~ 1 ns. These lifetimes and amplitudes correlate with the low fluorescence yields observed in the bound intercalators (Figs. 2 and 3) relative to those in the free intercalators.

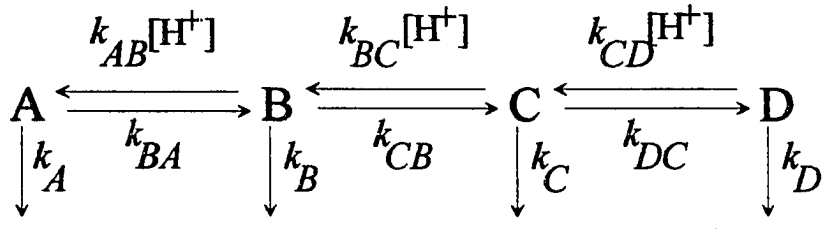

Figure 6. Kinetic scheme for interconversion of four excited-state species A, B, C, and D through sequential deprotonation in aminoacridine carboxamides.

Discussion

The pH-dependent fluorescence kinetics of the free intercalators 2-2C, 4-2C and 4-5C have been successfully modeled [12] using a sequential deprotonation scheme involving four excited state aminoacridine species, as shown in Fig. 6. In this scheme, species A, B, C, and D are the diprotonated, monoprotonated, unprotonated, and anionic aminoacridine carboxamides, respectively. This kinetic model predicts four-exponential fluorescence decay kinetics for each of the four species [12]. The lifetimes and pre-exponential factors depend on the deprotonation rate constants k_{BA}, k_{CB}, k_{DC}, on the unimolecular decay rates k_A, k_B, k_C, k_D, and on the ground- and excited-state pK_a values for the three deprotonation steps.

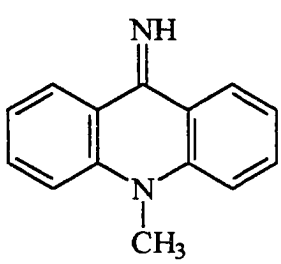

2

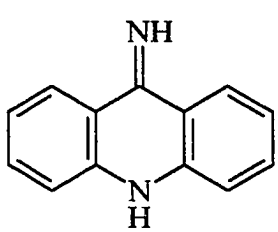

3

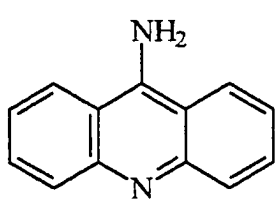

4

The free ground state intercalators are diprotonated at neutral pH. One of the protonation sites is the distal N atom in the carboxamide side chain. By analogy to other aliphatic amines near room temperature, the pK_a value for this site is likely to be 10-11 [14].

Singly protonated 9-aminoacridine itself is likely to exist as a true aminoacridine species, rather than as the tautomeric iminoacridan [15,16]. The structure of the unprotonated ground state 9-aminoacridine is unknown. Since the visible absorption band system of unprotonated 9-aminoacridine resembles that of 9-imino-10-methylacridan (**2**) much more closely than it resembles that of 1- or 2-aminoacridine [17], unprotonated ground state 9-aminoacridine may be an iminoacridan (**3**) instead of an aminoacridine (**4**). If the imino structure **3** correctly describes unprotonated ground state 9-aminoacridine, the first deprotonation occurs at the amino group, and the second deprotonation occurs at the heterocyclic pyridine N atom. If amino structure **4** is correct, the first deprotonation occurs instead at the pyridine N atom. For intercalators 2-2C and 4-2C, the first deprotonations exhibit pK_a values of 8.6 and 8.3, respectively. These are appreciably lower than pK_a = 9.9-10.0 for the first deprotonation of 9-aminoacridine [18]. In what follows, we will use pK_{a1}, pK_{a2}, pK_{a3} and pK_{a1}^*, pK_{a2}^*, pK_{a3}^* to denote the successive pK_a values (in increasing order) for the three deprotonation steps in the ground and fluorescing states, respectively.

The thermodynamic Förster cycle [19-21] is a useful predictor of pK_a shifts between the ground and fluorescing states in molecules in which intermolecular proton transfers are not accompanied by significant entropy changes. Since the absorption and fluorescence spectra of the free intercalators exhibit large red shifts for their first deprotonations (cf. Figs. 2-3), their pK_{a1}^* values are likely to be several units lower than their pK_{a1} values [12]. This

Table I. Rate Constants and Excited-State Equilibrium Constants from Simulations of Fluorescence Lifetimes and Amplitudes Using Sequential Deprotonation Model [a]

	Free 2-2C	DNA/ 2-2C	Free 4-2C	DNA/ 4-2C
pK_{a1}	9.25	10.25	8.8	9.5
pK_{a2}	9.50	10.3	9.25	10.85
pK_{a3}	13.0	13.0	12.0	12.0
pK_{a1}^*	2.0	2.0	2.0	2.0
pK_{a2}^*	8.3	9.25	8.3	8.8
pK_{a3}^*	13.0	13.0	13.0	13.0
$k_A + k_{BA}$ [b]	0.14	1.0	0.32	1.15
k_B	0.055	0.20	0.095	0.20
k_C	0.052	0.052	0.080	0.075
k_D	0.20	0.20	0.75	0.75
k_{CB}	0.08	1.15	0.20	0.45
k_{DC}	0.50	0.50	0.50	0.50

[a] All rate constants are in ns^{-1}; parameters for free intercalators are taken from reference 12.

[b] The parameters k_A and k_{BA} are covariant, and simulations only yield values for $k_A + k_{BA}$.

prediction is borne out by the optimized parameters (Table I) yielded by fits of the sequential deprotonation model (Fig. 6) to the pH-dependent fluorescence parameters (Figs. 4-5) of the free intercalators 2-2C, 4-2C, and 4-5C. In these fits, the fluorescence kinetics were well described by models in which pK_{a1} ranges from 8.3 to 9.5 (depending on the aminoacridine species), and pK_{a1}* is fixed at 2.0 [12]. We now consider the fluorescence kinetics of the bound intercalators 2-2C and 4-2C. For pH < 9.5, these differ fundamentally from those observed in the free intercalators through the presence of a large-amplitude subnanosecond decay component. In both 2-2C and 4-2C, this component's lifetime (which is too short to gauge in Fig. 4) is typically 70-100 ps. Attempts were made to model the fluorescence lifetimes and pre-exponential factors for the bound intercalators in Figs. 4-5, using the same kinetic scheme employed for the free intercalators. (In this view, the effects of DNA binding simply assert themselves through modulation of the six pK_a values and the seven rate constants k_{BA}, k_A, etc.) No combination of the thirteen parameters satisfactorily mimicked the observed pH dependence of the fluorescence parameters in the presence of DNA over the entire pH range. Since fluorescence quenching of intercalators in DNA is often markedly site-dependent (see below), the implicit assumption of sample homogeneity was relaxed by arbitrarily assigning the nanosecond and subnanosecond lifetime components to aminoacridine species in distinct binding environments. The subnanosecond component was therefore excluded from the analysis, and the two nanosecond component amplitudes from the triexponential fits were renormalized to unit sum. (This procedure is partly justified

because the fastest lifetime components arising from proton-transfer schemes such as the one in Fig. 6 have small amplitudes under broadband fluorescence detection conditions at most pH [12, 22]). With this exclusion, the nanosecond component lifetimes and amplitudes were readily simulated for the bound intercalators at all pH, as shown in Figs. 7 and 8. Typical parameters yielding satisfactory fits are listed alongside the corresponding parameters for the free intercalators [12] in Table I. Since the intercalators become unbound for pH $\geq$ 9.5-10, these fits were subject to the constraint that the values of k_D and k_{DC} in the presence of DNA are equal to those for the free intercalators [12]. It was unclear whether the unimolecular decay rates k_C should also be similar in the presence and absence of DNA (since pK_{a2} and pK_{a2}^* lie in the transition region of pH where the intercalators become unbound), but optimal fits were obtained when this was the case. The fits were relatively insensitive to the pK_{a1}^*, provided pK_{a1}^* was several units below pK_{a1} [12]; this parameter was arbitrarily fixed at 2.0 in all cases.

According to Table I, DNA binding causes substantial upward shifts in the empirical values of the deprotonation equilibrium constants pK_{a1}, pK_{a2}, and pK_{a2}^*. For example, pK_{a1} for the first ground state deprotonation of 4-2C is displaced from 8.8 to 9.5. Binding to calf thymus DNA thus appears to block ground state deprotonation until the pH is nearly high enough to dissociate the intercalator from the polynucleotide. Our simulations suggest that the equilibrium constants pK_{a2}, pK_{a2}^* for the second deprotonation are increased by 0.5-1.6 units upon binding to DNA. Since these values lie in the dissociation region, it is

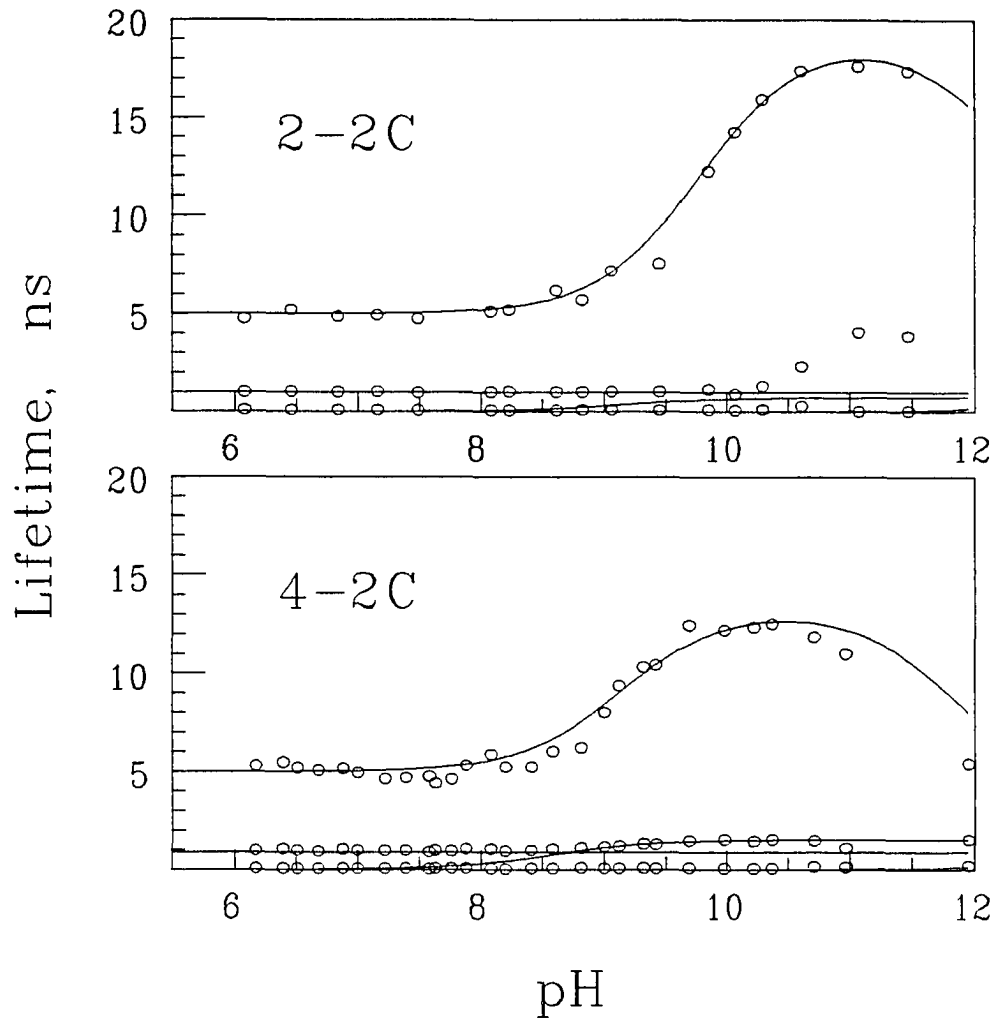

Figure 7. Nanosecond component lifetimes yielded by triexponential analyses of 2-2C and 4-2C fluorescence decays in the presence of DNA (data points) and lifetimes simulated using the kinetic model in Fig. 6 (continuous curves). Model parameters for simulations are listed in Table I.

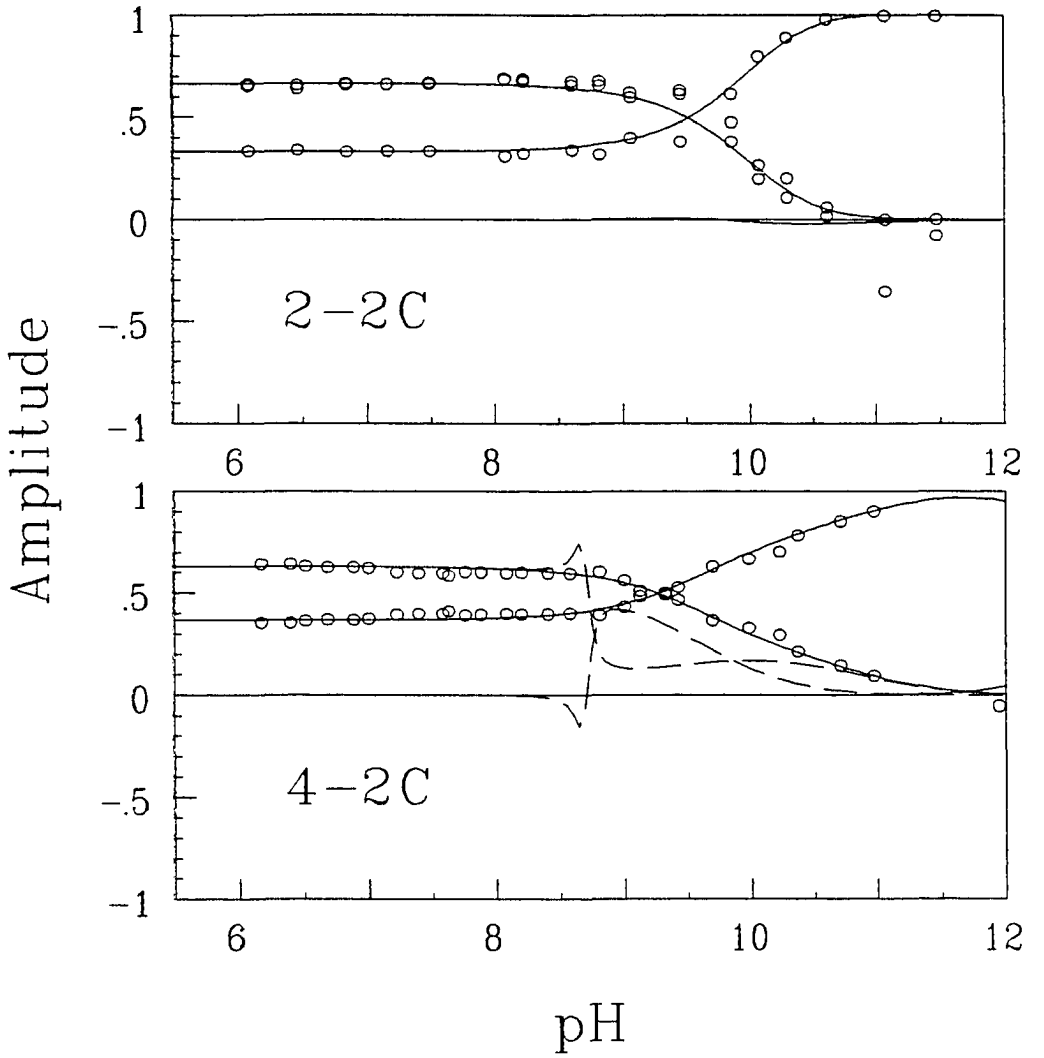

Figure 8. Amplitudes of nanosecond components from triexponential analyses of 2-2C and 4-2C fluorescence decays in the presence of DNA (data points) and amplitudes simulated using the kinetic model in Fig. 6 (continuous curves). Model parameters for simulations are listed in Table I.

unclear whether these are true equilibrium constants for the second deprotonation steps in the DNA-bound intercalators, or whether dissociation precedes these deprotonations. It is possible that DNA binding also produces shifts in the equilibrium constants pK_{a1}*, but our simulations indicate that displacements in pK_{a1}* commensurate with those in pK_{a1}, pK_{a2}, and pK_{a2}* (Table I) would have little effect on the observed fluorescence kinetics. It is clear, however, that pK_{a1}* cannot be as high as ~9.5; DNA binding does *not* block the first excited state deprotonation in these intercalators.

A second major effect of DNA binding appears in the unimolecular decay rate k_B of the singly protonated species, which controls the empirical long component lifetime observed for 2 < pH < 9.5 in our kinetic model. These long components are considerably shorter for DNA-bound 2-2C and 4-2C than for the free intercalators at any pH (Fig. 4). Hence, k_B is larger for the DNA-bound species by factors of 2 to 4 (k_B = 0.20 ns^{-1} for DNA-bound 4-2C, versus 0.095 ns^{-1} in solution). Possible mechanisms for these accelerated unimolecular decays are shortening of the radiative lifetimes (through alteration of the electronic structure upon DNA binding) and enhancement of the nonradiative decay through interaction with the DNA host.

In separate experiments, fluorescence decays were obtained for aminoacridine 4-2C bound to the synthetic polynucleotides poly(dG)-poly(dC) and poly(dA)-poly(dT) with loading $r \sim 0.05$ at pH ~ 7. In the case of 4-2C in poly(dG)-poly(dC), the fluorescence decay is strongly dominated (97%) by components with lifetime ≤ 50 ps. Small-amplitude

components (< 3%) appear with lifetimes 13.3 ns and 2.4 ns. The latter lifetimes resemble those of free 4-2C in solution at pH = 7 (Fig. 4), and may thus arise from residual, unbound 4-2C. Antecedents exist for strong intercalator fluoresence quenching by guanine bases [23-25]; the fluorescence yield of proflavine and quinacrine decreases with the G-C content of DNA, and similar quenching occurs for these intercalators in single-stranded poly(dG), but not poly(dC). In contrast, triexponential analysis of the fluorescence decay of 4-2C in poly(dA)-poly(dT) yields major nanosecond components, with lifetimes 8.8 ns (18%) and 3.3 ns (62%). A third component appears with lifetime 710 ps (19%). These lifetimes bear a family resemblance to (but are not the same as) the ones observed in calf thymus DNA at neutral pH (Fig. 4). Finally, the first major vibronic feature in the absorption spectrum of 4-2C in poly(dG)-poly(dC) and in poly(dA)-poly(dT) occurs at 443 and 437 nm, respectively; the corresponding band in double-stranded calf thymus DNA appears at the intermediate wavelength 441 nm. The majority of the intercalators thus appear to bind preferentially to G-C-rich regions of the polynucleotide, as reported earlier [11]. Hence, it is reasonable to attribute the (major) subnanosecond component of the fluorescence decays of 2-2C and 4-2C observed at pH < 9.5 to intercalators bound to G-C sites. The bulk of the fluorescence, observed for pH < 9.5 (corresponding to the longer component lifetimes), then stems principally from the minority of intercalators that are bound to A-T rich regions. By analogy to 4-2C in the presence of poly(dG)-poly(dC), a small fraction of the long-component fluorescence decays may arise from residual free intercalators.

The occurrence of intermolecular proton transfers at the first bound intercalator deprotonation site (which is likely to be the 9-amino group, because the unprotonated chromophore spectroscopically resembles an iminoacridan [17]) appears to rule out binding modes in which the amino group is buried in the DNA groove and shielded from the solvent. This would exclude one of the models proposed by Capomacchia et al. [18] for intercalation of the parent compond 9-aminoacridine. The fact that the equilibrium constants pK_{a1}, pK_{a2}, and pK_{a2}^* are significantly higher for the bound intercalators than for the solution intercalators correlates qualitatively with the known charge-transfer interactions between intercalators and DNA base pairs [25]. The fluorescence of many intercalators is quenched by charge transfer from the base (usually guanine, but in some cases adenine) to the excited intercalator. Such charge transfer interactions increase the electron density on the chromophore, and are thus expected to displace the pK_a values in the direction observed.

Acknowledgement

We thank Dr. Hai-Chou Chang for his assistance with this project in its early stages.

References

1. Atwell, G. J.; Cain, B. F.; Baguley, B. C.; Finlay, G. J.; Denny, W. A. *J. Med. Chem.* **1984**, *27*, 1481.

2. Cain, B. F.; Atwell, G. J. *Eur. J. Cancer* **1974**, *10*, 539.

3. Griffen, J. P.; Newman, R. A.; McCormack, J. J.; Krakoff, L. H. *Cancer Treat.Rep.* **1982**, *66*, 1323.

4. Piccart, M. *Eur. J. Cancer* **1981**, *17*, 775.

5. Lerman, L. S. *J. Mol. Biol.* **1961**, *3*, 18.

6. Zee-Cheng, R. K.-Y.; Podrebarac, E. G.; Menon, C. S.; Cheng, C. C. *J. Med. Chem.* **1979**, *22*, 501.

7. Zee-Cheng, R. K.-Y.; Cheng, C. C. *J. Med. Chem.* **1978**, *21*, 291.

8. Muller, W.; Crothers, D. M. *J. Mol. Biol.* **1968**, *35*, 251.

9. Feigon, J.; Denny, W. A.; Leupin, W.; Kearns, D. R. *J. Med. Chem.* **1984**, *27*, 450.

10. Denny, W. A.; Atwell, G. J.; Baguley, B. C.; Wakelin, L. P. G. *J. Med. Chem.* **1985**, *28*, 1568.

11. Wakelin, L. P. G.; Atwell, G. J.; Rewcastle, G. W.; Denny. W. A. *J. Med. Chem.* **1987**, *30*, 855.

12. Smith, C. A.; Chang, H-.C.; Struve, W. S.; Atwell, G. J.; Denny, W. A. *J. Phys. Chem.* **1995**, *99*, 8927.

13. Petrich, J. W.; Chang, M. C.; McDonald, D. B.; Fleming, G. R. *J. Am. Chem. Soc.* **1983**, *105*, 3824.

14. Perrin, D. D.; Dempsey, B.; Serjeant, E. P. *pK_a Prediction for Organic Acids and Bases*; Chapman and Hall: London, 1981; p 22.

15. Stezowski, J. J.; Kollat, P.; Bogucka-Ledóchowska, M.; Glusker, J. P. *J. Am. Chem. Soc.* **1985**, *107*, 2067.

16. Boyd, M.; Denny. W. A. *J. Med. Chem.* **1990**, *33*, 2656.

17. Albert, W.; Ritchie, J. *J. Chem. Soc.* **1943**, *1943*, 458.

18. Capomacchia, A. C.; Casper, J.; Schulman, S. G. *J. Pharm Sci.* **1974**, *63*, 1272.

19. Weller, A. *Prog. React. Kinet.* **1961**, *1*, 189.

20. Vander Donckt, E. *Prog. React. Kin.* **1970**, *5*, 273.

21. Jaffe, H. H.; Jones, H. L. *J. Org. Chem.* **1965**, *30*, 964.

22. Laws, W. R.; Brand, L. *J. Phys. Chem.* **1979**, *83*, 795.

23. Michelson, a. A.; Moony, C.; Kovoor, A. *Biochimie* **1972**, *54*, 1129.

24. Weisblum, B.; De Haseth, P. L. *Proc. Natl. Acad. Sci. USA* **1972**, *69*, 629.

25. Löber, G. *J. Luminescence* **1981**, *22*, 221.

GENERAL CONCLUSIONS

The excited state kinetics of the 9-aminoacridine carboxamides, discussed in the introduction as compounds **3**, were investigated. The first paper studied the kinetics of these compounds through steady-state fluorescence and absorption spectroscopies and the picosecond time resolved technique of photon counting. Spectroscopic titrations both in the steady-state and time resolved realms were performed and various kinetic models were used to theoretically simulate the experimental titration curves. Of the models attempted, the four species sequential proton transfers model was found to agree best with the experimental datum found for these carboxamides.

The determination of the excited state amplitudes and lifetimes have been thoroughly discussed for two and four species kinetic models. The two species model resulted in an identical set of two theoretical lifetimes for each excited species and a total of four theoretical amplitudes. A two state system was found to have a biexponential emission decay indifferent to the detection wavelength. The four state system resulted in an identical set of four theoretical lifetimes for each of its species and an overall total of sixteen theoretical amplitudes. The Laplace transform was used in both the two and four state analyses to convert the respective sets of differential decay equations into sets of algebraic equations.

The effects of DNA binding on the ground and excited state proton transfers of several *N*-((dimethylamino)-alkyl)-9-aminoacridine carboxamide intercalators were studied by steady-

state electronic spectroscopy and by time-correlated single photon counting. The fluorescence kinetics in calf thymus double stranded DNA of the 9-aminoacridine carboxamide intercalators are dominated by those intercalators bound to (dA)-(dT) sites, because fluorescence is extensively quenched for intercalators in poly(dG)-poly(dC). Binding to calf thymus DNA was found to increase the first deprotonation equilibrium constant in the ground state pK_{a1} of these intercalators by 0.7-1.0 units and increase pK_{a2}, pK_{a2}* for the second deprotonation in the ground and excited states. It was found that DNA binding does not block excited state proton transfers at the first deprotonation site because the pH-dependent fluorescence kinetics indicate that pK_{a1}* for the first excited state deprotonation is several units below pK_{a1}. Hence, specific interactions between the first deprotonation site (which is likely to be the 9-amino group) and the phosphate backbone do not appear to be involved in binding to (dA)-(dT) sites. The steady-state and time-resolved electronic spectroscopy of these intercalators in the presence of DNA were found to convert to those of the free intercalator at pH ~ 9.5-10, indicating that dissociation from the polynucleotide occurs at these pH.

Suggestions for further work include investigating the kinetics of the aminoacridine intercalators in various synthetic polynucleotide chains. Only the time resolved fluorescence of 4-2C bound to poly(dG)·poly(dC) and poly(dA)·poly(dT) have been investigated. The effects of different binding sites may be investigated through the use of synthetic polynucleotide strands like poly(dGdA)·poly(dCdT). Poly(dGdA)·poly(dCdT) would be interesting to investigate because bound aminoacridine intercalators would always be between

a fluorescence quenching (dG)-(dC) base pair and a (dA)-(dT) base pair. Many different synthetic polynucleotide strands could be used to investigate the kinetics of each type of binding site. Kinetic investigations in single strand synthetic polynucleotide strands (e.g. poly (dA)) could also prove to be informative by simplifying even further the number of possible binding sites.

ACKNOWLEDGMENTS

I wish to extend special thanks to Dr. Walter Struve for his guidance, encouragement, and support throughout my graduate training.

I also wish to extend a special thanks to Dr. Sergei Savihhin and Dr. Su Lin for their many helpful suggestions and assistance.

Thank you to Dr. Hai Chou Chang for his friendship and collaboration in the first paper of this work and to others of my research group for their support and friendship: Daniel Buck and JeNell Sibbald.

The writing of this dissertation would have been much more difficult without the patience, and understanding (and warm food) of my beautiful wife Ana.

APPENDIX

In order to determine the theoretical excited state lifetimes and amplitudes for different kinetic models computer programs were written in Borland C++. Additional programs were written in Maple V.2 software to solve the required determinants for finding the lifetimes and amplitudes of a particular model (e.g. determinants (52) and (82) in section I for the sequential proton transfers model). Other Maple V.2 programs were written to check the output (at a single pH value) of the larger and more complex Borland C++ programs. User programs were written in SPECTRA language to organize the final output, perform data manipulation, and compare the calculated results to experimental results. The computer programs contained in this appendix are only a small portion of the total number of computer programs written for this work since many different kinetic models were attempted to fit the experimental data of the first manuscript. The four species sequential proton transfers model of Figure 9b was shown to be in best agreement with the excited state kinetic data of the first manuscript. Therefore this appendix contains solely the computer programs used in obtaining the excited state lifetimes and amplitudes of the four species sequential proton transfers model.

The following program written in Borland C++ outputs four theoretical excited state lifetime curves verses pH for the optimum model. The program reads values for the rate constants and ionization constants from a data file called 'param.dat' whose origin will be

discussed later. The pH range for the theoretical lifetime calculation is specified within the program. The coefficients of the fourth order polynomial derived from the determinant (52) of section I were placed directly into the lifetime calculating program by a Maple V.2 program which is discussed later. The calculations within the lifetime calculating program incorporate Graeffe's Root squaring procedure to determine the roots of the fourth order polynomial. The precision for calculating these roots is specified within the program. The rate constants that are pH dependent (bimolecular) are specified within the program. The final calculation is placed into SPECTRA format for plotting, manipulation, and comparison with experimental values.

```
/* BELOW IS LINE8.CPP:  This program outputs four theoretical lifetime curves
verses pH for the four species sequential proton transfers model.  pH dependence
of the individual rate constants is done within the program.
*/
#include <stdio.h>
#include <stdlib.h>
#include <math.h>
#include "C:\SERGEI\SPECTRA.bg3\user.h"
#include <alloc.h>


//#define p(x){SP(PRINTF,"[%d]",x);}
#define p(x)  {};

extern int _stklen = 10000;

double m[5][100],nn[5][100];

int bioskey(int i)

{
```

```
    i=i;
    return (int)SP(GETVALUE,"\nPress ENTER!");
}

    int matherr (struct exception *a)
{
    SP(PRINTF,"\nMATH ERROR no %d, {%s}",a->type,a->name);
    bioskey(0);
    exit(1);
    return 0;
}


    float checkdouble(double x)
{
    if(x<-1e15) return -1.e15;
     else if(x>1e10) return 1.e15;
     else if(fabs(x)<1e-10) return 0;
    return x;
}

    /* This version calculates lifetimes (roots)  -1/r[i] for full calculation
    of 4 species equilibrium  A<>B<>C<>D  pH dependence is done in program  */

main (int argc,char *argv[])
{

    double kba,kab,ka,kb,kc,H,ba,cb,kd,kdc,kcd,dc;
    double kbc, kcb, kkba, kkcb, kkdc, kka, kkb, kkc, kkd;
    double Ka, ph;
    //FILE *pp;                 // char name[100];
    double a[10], gab, gbc, gcd;
    double b[10];
    double c[10];
    //double r[10], x[10], y[10], z[10], t[10];
    double A0,B0,C0,D0;
    double top,  rt, pplus, pminus;
    int n, np1, iter, itmax,  i, j, jj;

    float *(*spec);
    double *start,*step;
    int *len;
```

```
    char *comment;
    FILE *par;
    if(argc!=2) {printf("This program must be used from SPECTRA");return 0;}
    sscanf(argv[1],"%lu",&spectra);       /* load SPECTRA library function pointer */
    SP(FARMALLOC,farmalloc); /* Alter SPECTRA farmalloc function by new one
*/
    SP(FARFREE,farfree);          /* The same about farfree. These commands */
                                  /* are very, very important !!! */
     /* ABOVE WAS VERY IMPORTANT STANDARD SPECTRA USER
FUNCTION  HEADER ! */
    SP(SPECTRA,&spec,&start,&step,&len,&comment);

    p(1)

    par=fopen("PARAM.DAT","r+t");
    if(par==NULL) {SP(PRINTF,"Initial parameters not specified!");bioskey(0);return
       0;}
    SP(PRINTF,"Chuck's HopeSoft Inc., 1881\n");

    p(2);

    fscanf(par,"%lg",&kka);
    fscanf(par,"%lg",&kkb);
    fscanf(par,"%lg",&kkc);
    fscanf(par,"%lg",&kkd);
    fscanf(par,"%lg",&kkba);
    fscanf(par,"%lg",&kkcb);
    fscanf(par,"%lg",&kkdc);

        /*entering equilibrium constant values*/

    fscanf(par,"%lg",&ba);
    fscanf(par,"%lg",&cb);
    fscanf(par,"%lg",&dc);

       // parameters for finding ground state amplitudes for amplitude calculations

    fscanf(par,"%lg",&gab);
    fscanf(par,"%lg",&gbc);
    fscanf(par,"%lg",&gcd);

    p(3);
```

```
/*
printf("\nOutput to (con=console,prn=printer or file name) = ");scanf("%s",name);
pp=fopen(name,"w+t");
if(pp==NULL) {printf("Sorry, cannot output to %s",name);bioskey(0);return 0;}
*/
b[1] = 1.0;
c[1] = 1.0;

p(4);

n = 4;
itmax = 15;
top = 1.0e130;
//eps = 0.1;
//iprint = 0;

np1 = n+1;


for(ph=5,jj=0;ph<13.15;ph+=.05)          /* SPECIFY pH RANGE HERE*/

{
    H=pow(10,-ph);

    Ka=pow(10,-ba);
    kab =kkba/Ka;
    Ka=pow(10,-cb);
    kbc =kkcb/Ka;
    Ka=pow(10,-dc);
    kcd=kkdc/Ka;

    /* BELOW:  SET  RATE CONSTANTS THAT ARE PH DEPENDENT*/

    ka=kka;  kb=kkb;
    kc=kkc;  kd=kkd;

    kba=kkba;  kcb=kkcb;  kdc=kkdc;
    kab=kab*H;   kbc=kbc*H;   kcd=kcd*H;

    p(5);
    /*
    printf("\nka = %f, kb = %f, kc = %f, kd = %f", ka,kb,kc,kd);
```

```
printf("\nkba = %f, kab = %f, kdc = %f, kcd = %f", kba,kab,kdc,kcd);
printf("\nsa = %f, sb = %f, sc = %f, sd = %f", sa,sb,sc,sd);
 */

/*below:  coefficients of the fourth order polynomial calculated by Maple
were input directly into the program.  a[1]s^4+a[2]s^3+a[3]s^2+a[4]s+a[5]  */

a[1] = 1.0;
a[2] = kab+ka+kdc+kbc+kcb+kcd+kba+kb+kd+kc;
//SP(PRINTF,"{%lg,%lg,%lg,%lg}",a[2],sa,sb,sc);
a[3] = kba*kb + kb*kc + kb*kdc + kb*kbc + kab*kc + kab*kdc + kab*kbc +
       kcb*kc + kcb*kdc + ka*kb + ka*kab + ka*kcb + ka*kc + ka*kdc +
       ka*kbc + kba*kcb + kba*kc + kba*kbc + kab*kd + kb*kcd + kcb*kcd +
       kcb*kd + kb*kd + kab*kcd + ka*kd + ka*kcd + kba*kcd + kba*kd +
       kc*kd + kc*kcd + kdc*kd + kbc*kd + kbc*kcd + kba*kdc;

a[4] = kb*kbc*kd + kb*kbc*kcd + kab*kc*kd + kab*kc*kcd + kab*kdc*kd +
       kab*kbc*kd + kab*    kbc*kcd + kcb*kdc*kd + kba*kdc*kd + kcb*kc*kd
       + kba*kc*kcd + kb*kc*kcd + kb*kc*kd + kba*kb*kbc + kba*kcb*kcd +
       kb*kdc*kd + kba*kb*kd + kba*kbc*kcd + kcb*kc*kcd + kba*kcb*kd +
       kba*kc*kd + ka*kbc*kd + ka*kb*kcd + ka*kab*kd + ka*kcb*kcd +
       ka*kbc*kcd + ka*kcb*kd + ka*kdc*kd + ka*kc*kcd + ka*kb*kd +
       ka*kab*kcd + ka*kc*kd + kba*kbc*kd + kba*kb*kcd + kba*kb*kc +
       kba*kb*kdc + kba*kcb*kc + kba*kcb*kdc + ka*kb*kdc + ka*kb*kc +
       ka*kb*kbc + ka*kab*kc + ka*kab*kdc + ka*kab*kbc + ka*kcb*kc +
       ka*kcb*kdc;

a[5]=ka*kb*kc*kcd + ka*kb*kc*kd + ka*kb*kdc*kd + kba*kcb*kc*kd +
       kba*kb*kc*kcd + kba*kb*kc*kd + kba*kb*kdc*kd + ka*kab*kbc*kcd +
       ka*kcb*kc*kcd + kba*kcb*kc*kcd + kba*kb*kbc*kd + kba*kb*kbc*kcd +
       kba*kcb*kdc*kd + ka*kb*kbc*kd + ka*kb*kbc*kcd + ka*kab*kc*kd +
       ka*kab*kc*kcd + ka*kab*kdc*kd + ka*kcb*kdc*kd + ka*kab*kbc*kd +
       ka*kcb*kc*kd;

p(6);
/* a[1] = 1.0;
a[2] = -16.0;
a[3] = 78.0;
a[4] = -412.0;
a[5] = 624.0;

printf("\na1 = %f, a2 = %f, a3 = %f, a4 = %f, a5 = %f",
```

```
        a[1], a[2], a[3], a[4], a[5]);
*/

/*  BELOW IS GRAEFFE'S ROOT DETERMINING METHOD*/

c[1] = a[1]; c[2] = a[2]; c[3] = a[3]; c[4] = a[4]; c[5] = a[5];
p(7);
for (iter=1; iter <= itmax; iter++)
        {

        /*BELOW:  the algorithm to calculate the coefficients of the the
        proceeding polynomial in the sequence from the coefficients of the
        preceding polynomial*/

            //p(7001);
            /*SP(PRINTF,"[%lg,%lg,%lg]",c[1],c[2],c[3]);*/
            b[2] = - c[2]*c[2] + 2.0*c[1]*c[3];
            //p(701);
            b[3] = c[3]*c[3] - 2.0*c[2]*c[4]+ 2.0*c[1]*c[5];;
            //p(702);
            b[4] = - c[4]*c[4]+ 2.0*c[3]*c[5];;
            //p(71);
            b[5] = c[5]*c[5];

    /*
    if (iprint != 0) {printf("\niter = %d, np1 = %d", iter, np1);

                        printf("\nb1 = %f, b2 = %f, b3 = %f, b4 = %f, b5 = %f",
                        b[1], b[2], b[3], b[4], b[5]);}
    */
            for (i=2; i < np1+1; i++)
                {/* printf("\nbi = %e", b[i]);  */
                if (fabs(b[i]) > top || fabs(b[i]) < 1.0/top )
                {goto label;}       }

                c[1] = b[1]; c[2] = b[2]; c[3] = b[3]; c[4] = b[4];c[5] = b[5];
        }
p(8);
iter = itmax;

label:
p(81);
```

```
    for (i=2; i < np1+1; i++)
          {
              if(b[i-1]!=0) rt = fabs(b[i]/b[i-1]);
                else {SP(PRINTF,"b[i-1]=0 ! Divide by zero error!");
                                        bioskey(0);return 0;}

    /*BELOW:  each root is checked to determine validity and sign*/

              for (j=1; j < iter+1; j++)
                  {rt = sqrt(rt);}

              pplus =  a[1]*rt*rt*rt*rt + a[2]*rt*rt*rt + a[3]*rt*rt + a[4]*rt + a[5];
              pminus = a[1]*rt*rt*rt*rt - a[2]*rt*rt*rt + a[3]*rt*rt - a[4]*rt + a[5];

              if (fabs(pplus) > fabs (pminus)) {goto label1;}
                  //pval = pplus;
                  spec[i-2][jj] = checkdouble(rt);
                  spec[i-2][jj]=checkdouble(-1./rt);    /* -1/root so plot +tau vs pH */
                  goto label2;

              label1:
                  //pval = pminus;
                  spec[i-2][jj] = checkdouble(-rt);
                  spec[i-2][jj] = checkdouble(1./rt);  /*  same reason as above */
              label2:/*
                  if (fabs(pval) >= eps)
                          {printf("\nnot a root %f, polynomial is %f", rt, pval);}

                  else {printf("\nis a root %f, polynomial is %f", rt, pval);}
                   */
          }

    jj++;

}

p(9);
for(i=0;i<4;i++)
          {
                  len[i]=jj-1;
                  start[i]=5;          // set initial pH here
                  step[i]=0.05;         // set step here
```

```
        }
for(i=0;i<4;i++) SP(CHANGED,i);
p(10);
SP(SETSINGLE);
        {
                int j;
                double maxx=15;
                for(j=0;j<jj;j++)
                for(i=0;i<4;i++) if(maxx<spec[i][j]) maxx=spec[i][j];
                maxx=maxx*1.03;
            /*  SP(CLEAR);  */
                SP(SETPLOT,(float)start[0],(float)start[0]+(jj-1)*step[0],
                (float)0., (float)maxx);              // all SP fn's

   /*plot output in spectra format*/

                SP(INTERPRETE,"MINX=MINX;");
                SP(INTERPRETE,"C=COLOR;COLOR=0;SPEC0=1;TEXT 8,
                AT0(8), 1, SPEC0;PLOT SPEC0;COLOR=C;");
                SP(INTERPRETE,"C=COLOR;COLOR=1;SPEC0=2;TEXT 8.2,
                AT0(8.2), 1,SPEC0;PLOT SPEC0;COLOR=C;");
                SP(INTERPRETE,"C=COLOR;COLOR=2;SPEC0=3;TEXT 8.4,
                AT0(8.4), 1, SPEC0;PLOT SPEC0;COLOR=C;");
                SP(INTERPRETE,"C=COLOR;COLOR=3;SPEC0=4;TEXT
                8.6,AT0(8.6),1,SPEC0;PLOT SPEC0;COLOR=C;");
                SP(SETCOLOR,0);
        }

    return 0;
}
```

The following program written in Borland C++ outputs four theoretical excited state amplitude curves verses pH for the four species sequential proton transfers model. Since each lifetime has four amplitudes associated with it, these amplitudes are added together because experimentally they are indistinguishable. The final output of this program is therefore a total of four and not sixteen amplitudes plotted verses pH. The below amplitude calculating program reads fixed values for the rate constants, ground and excited state ionization

constants, and combined absorption/detection efficiencies from the data file 'param.dat.' In order to obtain values for the initial excited state populations, the program uses the ground state ionization constants to calculate at every pH value the relative ground state populations of the system. The combined absorption/detection efficiency for each species is most likely different (excitation was always at 400 nm) allowing these differences to be accounted for by multiplying the respective absorption/detection efficiency by its ground state population. The optimum values of the absorption/detection efficiencies are discovered by comparison of the theoretical amplitudes and the experimental amplitudes. The coefficients of the third order polynomials for each of the four excited state species (e.g. the coefficients of the third order polynomial for a(s) are found from the determinant (82) of section I) were each placed directly into the amplitude calculating program by a Maple V.2 program. Incorporated in the amplitude calculating program is Graeffe's Root squaring method for determining the roots of the third order polynomial equations in s. The precision for calculating the roots is specified within the program. The pH range of the calculation is specified within the program. The final calculation is placed into SPECTRA format for plotting, manipulation, and comparison with experimental values.

/* BELOW IS AMP8ALL.CPP: The program calculates amplitudes for the four species sequential proton transfers kinetic model. The program internally adds the amplitudes associated with the same lifetime. The final output is thus four amplitude curves verses pH and not sixteen curves verses pH. pH dependence of the individual rate constants is done within the program. The program also

```
incorporates the ground state ionization constants and absorption/detection
efficiencies in the determination of the initial excited state populations
*/
#include <stdio.h>
#include <stdlib.h>
#include <math.h>
#include "C:\SERGEI\SPECTRA.bg3\user.h"
#include <alloc.h>


//#define p(x){SP(PRINTF,"[%d]",x);}
#define p(x)  {};

extern int _stklen = 10000;

double m[5][100],nn[5][100];

int bioskey(int i)

    {
    i=i;
    return (int)SP(GETVALUE,"\nPress ENTER!");
    }

int matherr (struct exception *a)
    {
    SP(PRINTF,"\nMATH ERROR no %d, {%s}",a->type,a->name);
    bioskey(0);
    exit(1);
    return 0;
    }


float checkdouble(double x)
    {
    if(x<-1e15) return -1.e15;
      else if(x>1e10) return 1.e15;
      else if(fabs(x)<1e-10) return 0;
    return x;
    }
/* BELOW:  calculation of the lifetimes (roots  -1/r[i] ) of 4 species equilibrium
A<>B<>C<>D.  These roots are required to perform the amplitude calculations  */
```

```
main (int argc,char *argv[])
   {

   double kba,kab,ka,kb,kc,H,ba,cb,kd,kdc,kcd,dc;
   double kbc, kcb, kkba, kkcb, kkdc, kka, kkb, kkc, kkd;
   double ph, ka1, ka2, ka3, bn, Ka, gab, gbc, gcd;
   double aa, bb, cc, dd;
   double amp1, amp2, amp3, amp4, total;
   //FILE *pp;                  // char name[100];
   double a[10];
   double b[10];
   double c[10];
   double r[10], x[10], y[10], z[10], q[10];
   //double y[10], z[10], t[10];
   double A, B, C, D, D1, D2, D3, D4;
   double A0,B0,C0,D0;
   double top,  rt, pplus, pminus;
   int n, np1, iter, itmax,  i, j, jj;

   float *(*spec);
   double *start,*step;
   int *len;
   char *comment;
   FILE *par;
   if(argc!=2) {printf("This program must be used from SPECTRA");return 0;}
   sscanf(argv[1],"%lu",&spectra);        /* load SPECTRA library function pointer
      */
   SP(FARMALLOC,farmalloc);  /* Alter SPECTRA farmalloc function by new
      one */
   SP(FARFREE,farfree);          /* The same about farfree. These commands */
                                 /* are very, very important !!! */
    /* ABOVE WAS VERY IMPORTANT STANDARD SPECTRA USER
      FUNCTION HEADER ! */
   SP(SPECTRA,&spec,&start,&step,&len,&comment);

   p(1)

   par=fopen("PARAM.DAT","r+t");
   if(par==NULL) {SP(PRINTF,"Initial parameters not specified!"); bioskey(0);
                  return 0; }
   SP(PRINTF,"Chuck's HopeSoft Inc., 1881\n");
```

```
p(2);

fscanf(par,"%lg",&kka);
fscanf(par,"%lg",&kkb);
fscanf(par,"%lg",&kkc);
fscanf(par,"%lg",&kkd);
fscanf(par,"%lg",&kkba);
fscanf(par,"%lg",&kkcb);
fscanf(par,"%lg",&kkdc);

      /*equil. constants*/

fscanf(par,"%lg",&ba);
fscanf(par,"%lg",&cb);
fscanf(par,"%lg",&dc);

     // parameters for finding amplitudes

fscanf(par,"%lg",&gab);
fscanf(par,"%lg",&gbc);
fscanf(par,"%lg",&gcd);

     // coeff. for indicating efficiency of our being able to see the
     //   fluorescence

fscanf(par,"%lg",&aa);
fscanf(par,"%lg",&bb);
fscanf(par,"%lg",&cc);
fscanf(par,"%lg",&dd);


p(3);
    /*
    printf("\n Output to (con = console, prn = printer or file name) = "); scanf
    ("%s",name);
    pp=fopen(name,"w+t");
    if(pp==NULL) {printf("Sorry, cannot output to %s",name); bioskey(0); return
    0;}
    */
b[1] = 1.0;
c[1] = 1.0;
```

```
p(4);

n = 4;
itmax = 15;
top = 1.0e130;
//eps = 0.1;
//iprint = 0;

np1 = n+1;



for(ph=5,jj=0;ph<12.10;ph+=.05)
    {
    H=pow(10,-ph);


    Ka=pow(10,-ba);
    kab =kkba/Ka;
    Ka=pow(10,-cb);
    kbc =kkcb/Ka;
    Ka=pow(10,-dc);
    kcd=kkdc/Ka;

    /* below:  setting rate constants that are pH dependent*/

    ka=kka;  kb=kkb;
    kc=kkc;  kd=kkd;

    kba=kkba;  kcb=kkcb;  kdc=kkdc;
    kab=kab*H;   kbc=kbc*H;   kcd=kcd*H;

    p(5);
    /*
    printf("\nka = %f, kb = %f, kc = %f, kd = %f", ka,kb,kc,kd);
    printf("\nkba = %f, kab = %f, kdc = %f, kcd = %f", kba,kab,kdc,kcd);
    printf("\nsa = %f, sb = %f, sc = %f, sd = %f", sa,sb,sc,sd);
     */

    a[1] = 1.0;
```

```
a[2] = kab+ka+kdc+kbc+kcb+kcd+kba+kb+kd+kc;

//SP(PRINTF,"{%lg,%lg,%lg,%lg}",a[2],sa,sb,sc);

a[3] = kba*kb + kb*kc + kb*kdc + kb*kbc + kab*kc + kab*kdc + kab*kbc +
       kcb*kc + kcb*kdc + ka*kb + ka*kab + ka*kcb + ka*kc + ka*kdc +
       ka*kbc + kba*kcb + kba*kc + kba*kbc + kab*kd + kb*kcd + kcb*kcd
       + kcb*kd + kb*kd + kab*kcd + ka*kd + ka*kcd + kba*kcd + kba*kd
       + kc*kd + kc*kcd + kdc*kd + kbc*kd+ kbc*kcd + kba*kdc;

a[4] = kb*kbc*kd + kb*kbc*kcd + kab*kc*kd + kab*kc*kcd + kab*kdc*kd +
       kab*kbc*kd + kab*kbc*kcd + kcb*kdc*kd + kba*kdc*kd + kcb*kc*kd
       + kba*kc*kcd + kb*kc*kcd + kb*kc*kd + kba*kb*kbc + kba*kcb*kcd
       + kb*kdc*kd + kba*kb*kd + kba*kbc*kcd + kcb*kc*kcd +
       kba*kcb*kd + kba*kc*kd+ ka*kbc*kd + ka*kb*kcd + ka*kab*kd +
       ka*kcb*kcd + ka*kbc*kcd + ka*kcb*kd + ka*kdc*kd + ka*kc*kcd +
       ka*kb*kd + ka*kab*kcd + ka*kc*kd + kba*kbc*kd + kba*kb*kcd +
       kba*kb*kc + kba*kb*kdc + kba*kcb*kc + kba*kcb*kdc + ka*kb*kdc
       + ka*kb*kc + ka*kb*kbc + ka*kab*kc + ka*kab*kdc + ka*kab*kbc +
       ka*kcb*kc + ka*kcb*kdc;

a[5]=ka*kb*kc*kcd + ka*kb*kc*kd + ka*kb*kdc*kd + kba*kcb*kc*kd +
       kba*kb*kc*kcd + kba*kb*kc*kd + kba*kb*kdc*kd + ka*kab*kbc*kcd
       + ka*kcb*kc*kcd + kba*kcb*kc*kcd + kba*kb*kbc*kd +
       kba*kb*kbc*kcd + kba*kcb*kdc*kd + ka*kb*kbc*kd + ka*kb*kbc*kcd
       + ka*kab*kc*kd + ka*kab*kc*kcd + ka*kab*kdc*kd + ka*kcb*kdc*kd
       + ka*kab*kbc*kd + ka*kcb*kc*kd;

p(6);

    /*
    a[1] = 1.0;
    a[2] = -16.0;
    a[3] = 78.0;
    a[4] = -412.0;
    a[5] = 624.0;

    printf("\na1 = %f, a2 = %f, a3 = %f, a4 = %f, a5 = %f",
        a[1], a[2], a[3], a[4], a[5]);
    */

// BELOW IS GRAEFFE'S ROOT SQUARING TECHNIQUE
```

```
c[1] = a[1]; c[2] = a[2]; c[3] = a[3]; c[4] = a[4]; c[5] = a[5];
p(7);
for (iter=1; iter <= itmax; iter++)
        {
        //p(7001);
        /*SP(PRINTF,"[%lg,%lg,%lg]",c[1],c[2],c[3]);*/
        b[2] = - c[2]*c[2] + 2.0*c[1]*c[3];
        //p(701);
        b[3] = c[3]*c[3] - 2.0*c[2]*c[4]+ 2.0*c[1]*c[5];;
        //p(702);
        b[4] = - c[4]*c[4]+ 2.0*c[3]*c[5];;
        //p(71);
        b[5] = c[5]*c[5];

              /*
              if (iprint != 0) {printf("\niter = %d, np1 = %d", iter, np1);

              printf("\nb1 = %f, b2 = %f, b3 = %f, b4 = %f, b5 = %f",
              b[1], b[2], b[3], b[4], b[5]);}
              */

        for (i=2; i < np1+1; i++)
              {
              /* printf("\nbi = %e", b[i]);  */
              if (fabs(b[i]) > top || fabs(b[i]) < 1.0/top )
              {goto label;}
              }

              c[1] = b[1]; c[2] = b[2]; c[3] = b[3]; c[4] = b[4];c[5] = b[5];
        }
p(8);
iter = itmax;

label:
p(81);
for (i=2; i < np1+1; i++)

        {
        if(b[i-1]!=0) rt = fabs(b[i]/b[i-1]);
          else {SP(PRINTF,"b[i-1]=0 ! Divide by zero error!");
                                    bioskey(0);return 0;}
```

```
for (j=1; j < iter+1; j++)
        {rt = sqrt(rt);}

pplus =  a[1]*rt*rt*rt*rt + a[2]*rt*rt*rt + a[3]*rt*rt + a[4]*rt + a[5];
pminus = a[1]*rt*rt*rt*rt - a[2]*rt*rt*rt + a[3]*rt*rt - a[4]*rt + a[5];

if (fabs(pplus) > fabs (pminus)) {goto label1;}

        r[i-1] = rt;
        goto label2;
label1:

        r[i-1] = -rt;
label2:/*
        if (fabs(pval) >= eps)
                {printf("\nnot a root %f, polynomial is %f", rt, pval);}

        else {printf("\nis a root %f, polynomial is %f", rt, pval);}
         */
}
```

/*AMPLITUDE CALCULATION IS BELOW, THE PROGRAM CALCULATES THE FOUR AMPLITUDES FOR EACH LIFETIME AND ADDS THESE FOUR CALCULATED AMPLITUDES TOGETHER AT EACH pH VALUE. */

```
for (i=1; i<5; i++) {r[i] = fabs(r[i]);}
```

/* use pH dependent ground state A0,B0,C0, and D0, with ground state pka values gab, gbc, and gdc */

```
ka1=pow(10,-gab);
ka2=pow(10,-gbc);
ka3=pow(10,-gcd);

bn=ka1*H*H+ka1*ka2*H+ka1*ka2*ka3+H*H*H;

A0=H*H*H/bn;
B0=ka1*H*H/bn;
C0=ka2*ka1*H/bn;
D0=ka3*ka2*ka1/bn;
```

```
/* below are the coefficients for the third order polynomial:  (As^3+Bs^2+Cs+D) for
the amplitude calculation of species A in the model:  A<>B<>C<>D;  */

        A = A0;

        B = B0*kab + A0*kb + A0*kcb + A0*kc + A0*kd + A0*kab + A0*kdc +
                A0*kbc + A0*kcd;

        C = A0*kb*kc + A0*kb*kd + A0*kb*kbc + A0*kb*kdc + B0*kab*kd +
                B0*kab*kbc + B0*kab*kcd + C0*kab*kbc + A0*kb*kcd + A0*kab*kc
                + A0*kab*kdc + A0*kab*kbc + A0*kab*kd + A0*kcb*kc +
                A0*kcb*kdc + A0*kcb*kcd + A0*kc*kcd + A0*kc*kd + A0*kbc*kd +
                A0*kdc*kd + A0*kab*kcd + A0*kcb*kd + A0*kbc*kcd + B0*kab*kc +
                B0*kab*kdc;

        D = A0*kb*kdc*kd + A0*kab*kc*kcd + A0*kab*kc*kd + C0*kab*kbc*kcd +
                B0*kab*kdc*kd + D0*kab*kbc*kcd + A0*kb*kc*kcd +
                B0*kab*kbc*kcd + A0*kcb*kdc*kd + A0*kcb*kc*kd + B0*kab*kbc*kd
                + C0*kab*kbc*kd + A0*kab*kdc*kd + A0*kb*kc*kd + A0*kab*kbc*kd
                + A0*kab*kbc*kcd + A0*kb*kbc*kcd + B0*kab*kc*kcd +
                A0*kb*kbc*kd + A0*kcb*kc*kcd + B0*kab*kc*kd;

        /* Cauchy's Residue theorem */

        D1 = (r[2]-r[1])*(r[3]-r[1])*(r[4]-r[1]);
        D2 = (r[1]-r[2])*(r[3]-r[2])*(r[4]-r[2]);
        D3 = (r[1]-r[3])*(r[2]-r[3])*(r[4]-r[3]);
        D4 = (r[1]-r[4])*(r[2]-r[4])*(r[3]-r[4]);

        x[1] = (B*r[1]*r[1] - A*r[1]*r[1]*r[1] - C*r[1] + D)/D1;
        x[2] = (B*r[2]*r[2] - A*r[2]*r[2]*r[2] - C*r[2] + D)/D2;
        x[3] = (B*r[3]*r[3] - A*r[3]*r[3]*r[3] - C*r[3] + D)/D3;
        x[4] = (B*r[4]*r[4] - A*r[4]*r[4]*r[4] - C*r[4] + D)/D4;

                                /*COEFFICIENTS FOR SPECIES B*/

        A = B0;

        B = B0*kd + B0*kdc + B0*kbc + kba*B0 + B0*kc + ka*B0 + kba*A0 +
                B0*kcd + C0*kbc;

        C = ka*B0*kbc + kba*B0*kd + kba*B0*kcd + kba*B0*kdc + kba*B0*kc +
```

```
        B0*kc*kd + B0*kc*kcd + B0*kdc*kd + D0*kbc*kcd + C0*kbc*kd +
        C0*kbc*kcd + B0*kbc*kd + B0*kbc*kcd + kba*A0*kd + kba*B0*kbc
        + kba*A0*kc + kba*A0*kdc + kba*C0*kbc + kba*A0*kbc + ka*B0*kc
        + ka*B0*kd + ka*B0*kcd + ka*C0*kbc + kba*A0*kcd + ka*B0*kdc;

D = ka*C0*kbc*kd + ka*B0*kdc*kd + kba*B0*kdc*kd + ka*B0*kbc*kd +
        ka*B0*kbc*kcd + kba*B0*kbc*kcd + ka*B0*kc*kcd + kba*A0*kc*kcd
        + kba*C0*kbc*kd + ka*B0*kc*kd + ka*C0*kbc*kcd + kba*A0*kbc*kd
        + ka*D0*kbc*kcd + kba*B0*kc*kd + kba*B0*kc*kcd +
        kba*A0*kdc*kd + kba*D0*kbc*kcd + kba*A0*kbc*kcd +
        kba*C0*kbc*kcd + kba*B0*kbc*kd + kba*A0*kc*kd;

D1 = (r[2]-r[1])*(r[3]-r[1])*(r[4]-r[1]);
D2 = (r[1]-r[2])*(r[3]-r[2])*(r[4]-r[2]);
D3 = (r[1]-r[3])*(r[2]-r[3])*(r[4]-r[3]);
D4 = (r[1]-r[4])*(r[2]-r[4])*(r[3]-r[4]);

y[1] = (B*r[1]*r[1] - A*r[1]*r[1]*r[1] - C*r[1] + D)/D1;
y[2] = (B*r[2]*r[2] - A*r[2]*r[2]*r[2] - C*r[2] + D)/D2;
y[3] = (B*r[3]*r[3] - A*r[3]*r[3]*r[3] - C*r[3] + D)/D3;
y[4] = (B*r[4]*r[4] - A*r[4]*r[4]*r[4] - C*r[4] + D)/D4;

                        /*COEFFICIENTS FOR SPECIES C*/

A = C0;

B = kab*C0 + kb*C0 + kcb*C0 + C0*kd + C0*kcd + kcd*D0 + kcb*B0 +
        ka*C0 + kba*C0;

C = kab*C0*kd + kab*C0*kcd + kab*kcd*D0 + kcb*C0*kd + kcb*C0*kcd +
        kcb*kcd*D0 + kcb*B0*kd + kcb*B0*kcd + kba*kcb*A0 + kb*kcd*D0
        + kb*C0*kd + kb*C0*kcd + ka*kb*C0 + ka*kab*C0 + ka*kcb*C0 +
        ka*C0*kd + ka*C0*kcd + ka*kcd*D0 + ka*kcb*B0 + kba*kb*C0 +
        kba*kcb*C0 + kba*C0*kd + kba*C0*kcd + kba*kcd*D0 +
        kba*kcb*B0;

D = kba*kcb*C0*kcd + kba*kcb*kcd*D0 + ka*kb*C0*kd + kba*kcb*A0*kd +
        kba*kcb*A0*kcd + kba*kcb*B0*kd + kba*kcb*B0*kcd +
        ka*kab*C0*kcd + kba*kb*C0*kd + kba*kb*C0*kcd + ka*kab*kcd*D0
        + ka*kcb*C0*kd + ka*kcb*C0*kcd + kba*kcb*C0*kd +
        ka*kcb*kcd*D0 + ka*kab*C0*kd + ka*kb*C0*kcd + ka*kb*kcd*D0 +
        ka*kcb*B0*kd + kba*kb*kcd*D0 + ka*kcb*B0*kcd;
```

```
D1 = (r[2]-r[1])*(r[3]-r[1])*(r[4]-r[1]);
D2 = (r[1]-r[2])*(r[3]-r[2])*(r[4]-r[2]);
D3 = (r[1]-r[3])*(r[2]-r[3])*(r[4]-r[3]);
D4 = (r[1]-r[4])*(r[2]-r[4])*(r[3]-r[4]);

z[1] = (B*r[1]*r[1] - A*r[1]*r[1]*r[1] - C*r[1] + D)/D1;
z[2] = (B*r[2]*r[2] - A*r[2]*r[2]*r[2] - C*r[2] + D)/D2;
z[3] = (B*r[3]*r[3] - A*r[3]*r[3]*r[3] - C*r[3] + D)/D3;
z[4] = (B*r[4]*r[4] - A*r[4]*r[4]*r[4] - C*r[4] + D)/D4;

                    /*COEFFICIENTS FOR SPECIES D*/

A = D0;

B = D0*kbc + kab*D0 + kcb*D0 + kb*D0 + kba*D0 + C0*kdc + D0*kc +
      D0*kdc + ka*D0;

C = ka*D0*kc + kcb*C0*kdc + ka*kab*D0 + ka*kcb*D0 + ka*D0*kdc +
      kb*D0*kbc + kab*C0*kdc + kb*D0*kc + kb*D0*kdc + kb*C0*kdc +
      kab*D0*kc + kab*D0*kbc + kcb*D0*kc + kcb*D0*kdc + kcb*B0*kdc
      + ka*C0*kdc + ka*D0*kbc + kba*kcb*D0 + kba*D0*kc +
      kba*D0*kdc + kba*D0*kbc + kba*C0*kdc + kba*kb*D0 +
      kab*D0*kdc + ka*kb*D0;

D = kba*kcb*D0*kdc + kba*kcb*A0*kdc + kba*kcb*C0*kdc + ka*kb*D0*kc
      + ka*kb*D0*kdc + ka*kb*D0*kbc + kba*kb*D0*kbc + ka*kb*C0*kdc
      + ka*kab*D0*kc + ka*kab*D0*kdc + ka*kab*D0*kbc +
      ka*kcb*C0*kdc + ka*kcb*B0*kdc + kba*kb*D0*kc + ka*kcb*D0*kdc
      + kba*kb*D0*kdc + ka*kab*C0*kdc + ka*kcb*D0*kc +
      kba*kcb*B0*kdc + kba*kcb*D0*kc + kba*kb*C0*kdc;

D1 = (r[2]-r[1])*(r[3]-r[1])*(r[4]-r[1]);
D2 = (r[1]-r[2])*(r[3]-r[2])*(r[4]-r[2]);
D3 = (r[1]-r[3])*(r[2]-r[3])*(r[4]-r[3]);
D4 = (r[1]-r[4])*(r[2]-r[4])*(r[3]-r[4]);

q[1] = (B*r[1]*r[1] - A*r[1]*r[1]*r[1] - C*r[1]  +  D)/D1;
q[2] = (B*r[2]*r[2] - A*r[2]*r[2]*r[2] - C*r[2]  +  D)/D2;
q[3] = (B*r[3]*r[3] - A*r[3]*r[3]*r[3] - C*r[3]  +  D)/D3;
q[4] = (B*r[4]*r[4] - A*r[4]*r[4]*r[4] - C*r[4]  +  D)/D4;
```

```
/*The four amplitudes for each lifetime are now added but are first multiplied by their
respective absorption/detection efficiencies  aa, bb, cc, and dd.  The lifetimes are
designated with numbers one through four and the amplitude for each lifetime is
represented by:  x, y, z, and q, respectively*/

                amp1= aa*x[1] + bb*y[1] + cc*z[1] + dd*q[1];
                amp2= aa*x[2] + bb*y[2] + cc*z[2] + dd*q[2];
                amp3= aa*x[3] + bb*y[3] + cc*z[3] + dd*q[3];
                amp4= aa*x[4] + bb*y[4] + cc*z[4] + dd*q[4];

                                /*  THE AMPLITUDES ARE NORMALIZED*/

                   total=amp1 + amp2 + amp3 + amp4;

                spec[0][jj]=amp1/total;
                spec[1][jj]=amp2/total;
                spec[2][jj]=amp3/total;
                spec[3][jj]=amp4/total;

                     /*
                          spec[0][jj]=aa*x[1] + bb*y[1] + cc*z[1] + dd*q[1];
                          spec[1][jj]=aa*x[2] + bb*y[2] + cc*z[2] + dd*q[2];
                          spec[2][jj]=aa*x[3] + bb*y[3] + cc*z[3] + dd*q[3];
                          spec[3][jj]=aa*x[4] + bb*y[4] + cc*z[4] + dd*q[4];
                     */

    jj++;

    }

p(9);
for(i=0;i<4;i++)
    {
    len[i]=jj-1;
    start[i]=5;          // set initial pH here
    step[i]=0.05;         // set step here
    }

/*PLOT COMMANDS ARE BELOW*/

SP(INTERPRETE,"DUMP=0;GETX 1,MINX,MAXX;MINY=-1;MAXY=1;");
```

```
SP(INTERPRETE,"C=COLOR;COLOR=0;SPEC0=1;TEXT 8, AT0(8), 1,
   SPEC0; PLOT SPEC0;COLOR=C;");
SP(INTERPRETE,"C=COLOR;COLOR=1;SPEC0=2;TEXT 8.2, AT0(8.2), 1,
   SPEC0;PLOT SPEC0;COLOR=C;");
SP(INTERPRETE,"C=COLOR;COLOR=2;SPEC0=3;TEXT 8.4, AT0(8.4), 1,
   SPEC0;PLOT SPEC0;COLOR=C;");
SP(INTERPRETE,"C=COLOR;COLOR=3;SPEC0=4;TEXT 8.6, AT0(8.6), 1,
   SPEC0;PLOT SPEC0;COLOR=C;");
SP(SETCOLOR,0);
SP(INTERPRETE,"SET SCALE 1;SET SCALEX;SET SCALEY;");


return 0;
}
```

Two programs were written using Maple V version 2.0a (DOS-5203-250123-1) software. The below Maple program calculates symbolically the coefficients of a 4x4 determinant. The program asks for each element of the determinant a_{xy} where x is the row and y is the column. The determinant is then calculated and the terms of similar powers in s are collected. The sorted coefficients in powers of s are then placed into a file called 'tmp.txt.' The purpose of creating the file is to avoid human error in placing the coefficients into the Borland C++ computer programs that calculate the lifetimes and amplitudes. An analologous Maple program was written to calculate symbolically the coeffecients of the 3x3 determinant for amplitude determinations and is not included in this appendix.

```
readlib(write);readlib(C);
with(linalg);

a11:=ka+kba+s;          a12:=-kab;
a13:=0;                 a14:=0;
a21:=-kba;              a22:=kb+kab+kcb+s;
a23:=-kbc;              a24:=0;
```

```
a31:=0;                    a32:=-kcb;
a33:=kc+kdc+kbc+s;         a34:=-kcd;
a41:=0;                    a42:=0;
a43:=-kdc;                 a44:=kd+kcd+s;

A:=matrix([[a11,a12,a13,a14],[a21,a22,a23,a24],[a31,a32,a33,a34],[a41,a42,a43,a4
4]]);

D:=det(A);
CO:=collect(D,s);

s1:=coeff(CO,s);
s2:=coeff(CO,s^2);
s3:=coeff(CO,s^3);
s4:=coeff(CO,s^4);
s0:=coeff(CO,s,0);

open(`tmp.txt`);write(`/****** These are the coefficients found by Maple ******/`);
write(`\n{double t0;\ns0=`);close();
appendto(`tmp.txt`);write(C(s0));write(`s0=`);close();
appendto(`tmp.txt`);write(C(s1));write(`s1=`);close();
appendto(`tmp.txt`);write(C(s2));write(`s2=`);close();
appendto(`tmp.txt`);write(C(s3));write(`s3=`);close();
appendto(`tmp.txt`);write(C(s4));write(`s4=`);close();
appendto(`tmp.txt`);write(`}\n/******** Coefficients s0...s4 are calculated
*****************/\n`);close();
```

The second Maple V program follows and calculates the amplitudes and the lifetimes for each of the four species at a single pH value. The purpose of this program is to test the results of the much more complicated Borland C++ programs that calculate lifetimes and amplitudes for a range of pH values. The below program requires the input of the fixed values of the rate constants and the three excited state ionization constants. The program also asks for the pH value where the calculation is to be made and the ground state populations A0, B0, C0, and D0 at the assigned pH.

```
with(linalg);
H:=1E-9;
kBA:=.1;          KaBA:=1E-2;                kAB:=kBA/KaBA;

kCB:=5;           KaCB:=3.16227766E-9;       kBC:=kCB/KaCB;
kDC:=5;           KaDC:=1e-11;               kCD:=kDC/KaDC;
kA:=.15;          kB:=.084;                  kC:=.075;
kD:=0.1;

A0:=0;      B0:=0;      C0:=0;          D0:=.6;

kAB:=kAB*H;       kBA:=kBA;       kBC:=kBC*H;       kCB:=kCB;
kCD:=kCD*H;       kDC:=kDC;

D:=array([[s+kBA+kA,-kAB,0,0],[-kBA,s+kAB+kCB+kB,
      -kBC,0],[0,-kCB,s+kBC+kC+kDC,-kCD],[0,0,-kDC,s+kD+kCD]]);

A:=array([[A0,-kAB,0,0],[B0,s+kAB+kCB+kB,
      -kBC,0],[C0,-kCB,s+kBC+kC+kDC,-kCD],[D0,0,-kDC,s+kD+kCD]]);

B:=array([[s+kBA+kA,A0,0,0],[-kBA,B0, -kBC,0],[0,C0,s+kBC+kC+kDC,-
      kCD],[0,D0,-kDC,s+kD+kCD]]);

C:=array([[s+kBA+kA,-kAB,A0,0],[-kBA,s+kAB+kCB+kB, B0,0],[0,-kCB,C0,-
      kCD],[0,0,D0,s+kD+kCD]]);

F:=array([[s+kBA+kA,-kAB,0,A0],[-kBA,s+kAB+kCB+kB,
      -kBC,B0],[0,-kCB,s+kBC+kC+kDC,C0],[0,0,-kDC,D0]]);

readlib(laplace);

invlaplace(det(A)/det(D),s,t);
invlaplace(det(B)/det(D),s,t);
invlaplace(det(C)/det(D),s,t);
invlaplace(det(F)/det(D),s,t);
```

Various SPECTRA user programs were written to input, output, and manipulate the calculated theoretical lifetime and amplitude curves from the above programs. The following user program is called 'user3.hlp' and its purpose is to create a menu of choices of different computer programs and options to output the data.

```
#SET_PAR
param.spp
        creates a data file of the parameters required to calculate the lifetimes
        and amplitudes
#CalcLife
line8.exe
        calculates the theoretical lifetimes as a function of pH
#CalcAmp
amp8all.exe
        calculates the theoretical amplitudes as a function of pH, and adds the
        amplitudes for similar lifetimes
#Print_Par
printpar.spp
        outputs the values of the parameters used in the calculation to the printer
#CLEAR
clean.spp
        clears the display screen
#SCALE
scale.spp
        sets x and y scale of the plots of amplitude and lifetime verses pH plots
#Plot_Exp
exp.spp
        overlays the experimental curve on top of the calculated curve for
        comparison
#end
end
        used to quit program
```

The following user program 'param.spp' allows the user to specify values for all of the parameters required for calculating the theoretical lifetimes and amplitudes. The program

places the user specified values for these parameters into a data file called 'param.dat.' The data file 'param.dat' is read by the Borland C++ programs that calculate the lifetimes and amplitudes.

```
print "parameters "
close 1
open "param.dat" append as 1
if filelen(1)>2;gosub 20
1: menu "par1",3,"par2",5,"par3",7,"SET",10
3: menu "ka=",a,"kb=",b,"kc=",c,"kd=",d,"kba=",e,"kcb=",f,"kdc=",g,"SET",10
goto 1
5: menu
"pKaBA=",h,"pKaCB=",i,"pKaDC=",j,"gpKaAB=",k,"gpKaBC=",l,"gpKaCD=",m,"SET",
10
goto 1
7: menu "aa=",n,"bb=",o,"cc=",p,"dd=",q,"SET",10
stop
10: close 1
   open "param.dat" output 1
   print
#1,a,"\n",b,"\n",c,"\n",d,"\n",e,"\n",f,"\n",g,"\n",h,"\n",i,"\n",j,"\n",k,"\n",l,"\n",m,"\n",n,"\n"
,o,"\n",p,"\n",q
   close 1
   stop
20: close 1
   open "param.dat" input 1
   print #1,?a,?b,?c,?d,?e,?f,?g,?h,?i,?j,?k,?l,?m,?n,?o,?p,?q
   close 1
   return
```

The following user program is called 'printpar.spp.' The purpose of this program is to output the user specified values of the rate constants, ground and excited state ionization constants, and absorption/detection efficiencies in an organized format.

```
print "printing parameters... "
close 1
```

```
open "param.dat" append as 1
if filelen(1)<2;close 1;print "Cannot find file!";stop
close 1
open "PARAM.DAT" input as 1
print #1,?a,?b,?c,?d,?e,?f,?g,?h,?i,?j,?k,?l,?m,?n,?o,?p,?q
close 1
33:open "prn" output 1
print #1,"\nparameters for sequential pKa model: A<>B<>C<>D"
print #1,"\n A  < >  B  < >  C  < > D"
print #1,"\npKaBA=",h,", pKaCB=",i,", pKaDC=",j,",gpKaAB=",k,", gpKaBC=",l,",
gpKaCD=",m
print #1,"\n ka=",a," kb=",b," kc=",c," kd=",d," kba=",e," kcb=",f," kdc=",g
print #1,"\n"
print #1,"\nweighting factors for detection:  aa=",n,", bb=",o,", cc=",p,", dd=",q
print #1,"\n"

close 1
```

The purpose of the last four programs of this appendix is to calculate and organize the ground state equilibrium population of the four species sequential proton transfer system. The below program calculates the ground state equilibrium populations. It does this by first reading the values for the three ground state ionization constants from the data file 'par.dat.' The program then calculates the groundstate populations and plots them verses pH in SPECTRA format. The pH region is chosen within the program.

```
/* This program calculates the ground state population of the 4 species equilibrium
with respect to pH  A<>B<>C<>D  */


#include <stdio.h>
#include <stdlib.h>
#include <math.h>
#include "C:\SERGEI\SPECTRA.ext\user.h"
#include <alloc.h>

#define p(x)  {SP(PRINTF,"[%d]",x);}
```

```
//#define p(x){};

extern int _stklen = 10000;

double m[5][100],nn[5][100];

int bioskey(int i)

{
i=i;
return (int)SP(GETVALUE,"\nPress ENTER!");
}

int matherr (struct exception *a)
{
SP(PRINTF,"\nMATH ERROR no %d, {%s}",a->type,a->name);
bioskey(0);
exit(1);
return 0;
}


float checkdouble(double x)
{
if(x<-1e10) return -1.e10;
  else if(x>1e10) return 1.e10;
  else if(fabs(x)<1e-10) return 0;
return x;
}

main (int argc,char *argv[])
{

double ka1,ka2,ka3,den,A,B,C,D,H,ph;
int   i,  jj;

float *(*spec);
double *start,*step;
int *len;
char *comment;
FILE *par;
if(argc!=2) {printf("This program must be used from SPECTRA");return 0;}
```

```
sscanf(argv[1],"%lu",&spectra);   /* load SPECTRA library function pointer */
SP(FARMALLOC,farmalloc);          /* Alter SPECTRA farmalloc function by new one
*/
SP(FARFREE,farfree);              /* The same about farfree. These commands */
                                  /* are very, very important !!! */
 /* ABOVE WAS VERY IMPORTANT STANDARD SPECTRA USER FUNCTION
HEADER ! */
SP(SPECTRA,&spec,&start,&step,&len,&comment);

p(1)

par=fopen("PAR.DAT","r+t");
if(par==NULL) {SP(PRINTF,"Initial parameters not specified!");bioskey(0);return 0;}
SP(PRINTF,"Chuck's HopeSoft Inc., 1881\n");

p(2);

fscanf(par,"%lg",&ka1);
fscanf(par,"%lg",&ka2);
fscanf(par,"%lg",&ka3);
fclose(par);
/*
fscanf(par,"%lg",&A0);
fscanf(par,"%lg",&B0);
fscanf(par,"%lg",&C0);
fscanf(par,"%lg",&D0);
*/
for(ph=1,jj=0;ph<13.1;ph+=.1)
{
H=pow(10,-ph);

den=ka1*H*H+ka1*ka2*H+ka1*ka3*ka2+H*H*H;

A=H*H*H/den;
B=ka1*H*H/den;
C=ka2*ka1*H/den;
D=ka3*ka2*ka1/den;
                SP(GETSPEC,0);
                spec[0][jj] = checkdouble(A);
                SP(GETSPEC,1);
                spec[1][jj] = checkdouble(B);
                SP(GETSPEC,2);
```

```
                spec[2][jj] = checkdouble(C);
                SP(GETSPEC,3);
                spec[3][jj] = checkdouble(D);

jj++;

}

p(9);
for(i=0;i<=3;i++)
        {
        len[i]=jj-1;
        start[i]=1;             // set initial pH here
        step[i]=0.1;            // set step here
        }
for(i=0;i<=3;i++) SP(CHANGED,i);
p(10);
SP(SETSINGLE);
        {

        double maxx=1.2;
        /*
        int j;
        for(j=0;j<jj;j++)
                for(i=0;i<4;i++) if(maxx<spec[i][j]) maxx=spec[i][j];
        maxx=maxx*1.03;
        */
    /*  SP(CLEAR);  */
        SP(GETSPEC,0);
        SP(SETPLOT,(float)start[0],(float)start[0]+(jj-1)*step[0],(float)0.,(float)maxx); //
all SP fn's
    /*
        for(i=0;i<4;i++)
                    // require float, so 1. or 0. etc.
                {
                SP(SETCOLOR,i);
                SP(PLOT,spec[i],start[i],step[i],len[i],0);
                }
    */
        SP(INTERPRETE,"MINX=MINX;");
        SP(INTERPRETE,"C=COLOR;COLOR=0;SPEC0=1;TEXT
8,AT0(8),1,SPEC0;PLOT SPEC0;COLOR=C;");
```

```
        SP(INTERPRETE,"C=COLOR;COLOR=1;SPEC0=2;TEXT
8.2,AT0(8.2),1,SPEC0;PLOT SPEC0;COLOR=C;");
        SP(INTERPRETE,"C=COLOR;COLOR=2;SPEC0=3;TEXT
8.4,AT0(8.4),1,SPEC0;PLOT SPEC0;COLOR=C;");
        SP(INTERPRETE,"C=COLOR;COLOR=3;SPEC0=4;TEXT
10.0,AT0(10.0),1,SPEC0;PLOT SPEC0;COLOR=C;");
        SP(SETCOLOR,0);
     SP(INTERPRETE,"SET SCALE 2;SET SCALEX;SET SCALEY;");
        }

return 0;
}
```

Three separate user programs are required for the above groundstate calculating program.

The first is the menu program called 'user3.hlp.' The user programs are written in SPECTRA

format and not Borland C++ format.

```
#SET_PAR
pargrnd.spp
  No help!
#Calc_grnd
grndst.exe
  Look at the help for Set_PAR
#Print_Par
pargrdpr.spp
 Just press enter and you'll see
what is it!
#CLEAR
clean.spp
#SCALE
scale.spp
sets scale
#end
end
```

One of the program options in the above user menu is 'pargrnd.spp.' 'pargrnd.spp' is a user program that asks for the required parameters for the calculation of the ground state populations. The program is described below.

```
print "parameters "
close 1
open "param.dat" append as 1
if filelen(1)>2;gosub 20
1: menu "par1",3,"SET",10
3: menu "ka1=",a,"ka2=",b,"ka3=",c,"SET",10
goto 1
5:                                                                    menu
"pKaBA=",h,"pKaCB=",i,"pKaDC=",j,"A0=",k,"B0=",l,"C0=",m,"D0=",n,"SET",10
goto 1
stop
10: close 1
   open "param.dat" output 1
   print #1,a,"\n",b,"\n",c,"\n"
   close 1
   stop
20: close 1
   open "param.dat" input 1
   print #1,?a,?b,?c
   close 1
   return
```

The last important user program mentioned in the user menu for calculating ground state equilibrium populations is 'pargrdpr.spp.' This user program allows the printer to output the user specified parameters in an organized format.

```
print "printing parameters... "
close 1
```

```
open "param.dat" append as 1
if filelen(1)<2;close 1;print "Cannot find file!";stop
close 1
open "PARAM.DAT" input as 1
print #1,?a,?b,?c,?d,?e,?f,?g,?h,?i,?j,?k,?l,?m,?n
close 1
33:open "prn" output 1
print #1,"\nparameters for sequential pKa model: A<>B<>C<>D ground state
population"
rem print #1,"\npKaBA=",h,", pKaCB=",i,", pKaDC=",j,", A0=",k,", B0=",o,", C0=",m,",
D0=",n
print #1,"\n"
print #1,"\n ka1=",a," ka2=",b," ka3=",c
print #1,"\n  A   < >    B   < >    C   < > D"
print #1,"\n"

close 1
```